DYNAMIC CHARACTERIZATION OF INERTANT META-STRUCTURES

By

KARTHIK MADHAMSHETTY

Bachelor of Engineering in Mechanical Engineering

Osmania University

Hyderabad, India

2015

Submitted to the Faculty of the
Graduate College of
Oklahoma State University
in partial fulfillment of
the requirements for
the Degree of
MASTER OF SCIENCE
December, 2018

DYNAMIC CHARACTERIZATION OF INERTANT META-STRUCTURES

Thesis Approved:

Dr. James M. Manimala

Thesis Adviser

Dr. James K. Good

Dr. Aurelie Azoug

ACKNOWLEDGEMENTS

I cannot express my gratitude in words for the moral support and unconditional love from my parents, Laxmi Narayana and Dhana Laxmi. I cannot imagine where I would stand without them. I thank them for their sacrifice and for being my pillars of support.

I sincerely thank my adviser, Dr. James M. Manimala for giving me the opportunity and guidance to complete my graduate studies. He has been a true inspiration to me and I am indebted to his patience and unbounded knowledge. He constantly supported me and steered me in the right direction whenever needed. Without his meticulous guidance and constant support, this thesis would not have been possible.

I would like to express my gratitude to Dr. James K. Good for his insights on research and teaching me the basics of finite element methods which helped me throughout my research. I would also like to thank Dr. Aurelie Azoug for her support.

I would like to thank Jaya Sahithi Vemparala who identified the potential in me and for supporting, guiding and motivating me all the time.

I would like to thank Prateek P. Kulkarni for being there for me whenever needed, he has been an amazing teacher and I always enjoyed our technical discussions.

I would like to thank Venkat Ramya Chilukuri, Milkyas Afework, Alexander Svetgoff, Timothy Emerson, Alessio Lozzi, and Catherine Sheehan for their support.

Name: KARTHIK MADHAMSHETTY

Date of Degree: DECEMBER, 2018

Title: DYNAMIC CHARACTERIZATION OF INERTANT META-STRUCTURES

Major: MECHANICAL AND AEROSPACE ENGINEERING

Abstract: In establishing the traditional analogies between mechanical and electrical networks, lack of preservation of topology while transitioning from a mechanical to its equivalent electrical network was rectified by so-called mobility or force–current analogy. One drawback was that the mass, which is the equivalent of the grounded capacitor, cannot represent a two-terminal device when described in an inertial frame. This was remedied by a two-terminal mechanical device termed the 'inerter' postulated at the turn of this century. The inerter is a mechanical element in which applied force is proportional to the relative acceleration across its terminals. The proportionality constant is termed 'inertance'. Practically, the inerter is realized by storing energy using a flywheel and can deliver a dynamic mass presence a few orders of magnitude greater than the device mass leading to considerable interest in inerters in recent years. In this study, inspired by acoustic metamaterials (AM), the dynamic characteristics of 'meta-structures' employing inerters are explored. Firstly, improved analytical models incorporating component inertias and sizing and parametric studies for two prominent embodiments of the inerter viz. the rack-and-pinion and the ball-screw inerter are considered. The dependence of specific inertance (ratio of inertance to static mass) on key parameters are brought out through simulations. A prototype rack-and-pinion inerter with specific inertance of 90 was designed, fabricated and tested under low-rate excitations. Measured specific inertance was found to display an exponential decline with increase in excitation frequency. Using a phase-matching procedure, estimation of internal stiffness and damping in the prototype reveals influences of the excitation frequency and ultra-low frequency meandering effects. Further, motivated by challenges in miniaturizing rotary components for microscale inerters, a potential kinematically-simpler structure based on the von Mises truss is investigated. Its nonlinear equation of motion is derived using Hamilton's principle. Potential inertant mechanisms for this structure under harmonic inputs are probed using simulations. Finally, while studies on inherent nonlinearities in inerters are more widely available, those concerning the use of intentionally nonlinear inerters are scarce. In this context, the mechanical wave manipulation characteristics of Nonlinear Inertant Acoustic Metamaterials (NLIAM) are studied. Based on notional concepts for inertant devices, frequency and acceleration-dependent nonlinear inertant models are advanced. Dispersion characteristics of NLIAM with frequency-dependent inverse square law (ISL) and power law (PL) inertance are examined. While a tuned ISL model ensures existence of band gap over almost the entire bandwidth of interest, its limiting inertances are challenging to realize in practice. A potentially more practical PL approximation is proposed and shown to have a widening of the band gap by more than 100% towards frequencies below the lower bound of the band gap for the AM with frequency invariant inertance. Further, drawing inspiration from the Duffing-type stiffness, first order dispersion corrections are obtained for an NLIAM with acceleration-dependent inertance using a perturbation approach. Dispersion curves shifts are found to enable this NLIAM to act as a passive adaptive filter for mechanical waves based solely on excitation amplitude. Practical manifestations of NLIAM could help realize extraordinary wave manipulation capabilities especially suitable for low frequency structural dynamic applications.

TABLE OF CONTENTS

Chapter Page

LIST OF TABLES

LIST OF FIGURES

Figure Page

Figure Page

Figure Page

Figure Page

LIST OF SYMBOLS AND ABBREVATIONS

J…….....Inertance

ϒ…….....Specific inertance

DCSE……Displacement Control Sinusoidal Excitation

ACSE……...Acceleration Control Sinusoidal Excitation

u_r…….Displacement of the Rack

Φ…….....Phase angle

M_{st}……Static mass

k…….....Stiffness

c……...Damping constant or coefficient

L…….....Lagrange

T…….....Kinetic energy

V…….....Potential energy

SAM…….Swing Arm Mass

SAL……..Swing Arm Length

AM……...Acoustic Metamaterial

LRAM…….....Locally Resonant Acoustic Metamaterial

LIAM……...Linear Inertant Acoustic Metamaterial

NLIAM…….....Nonlinear Inertant Acoustic Metamaterial

ISL…….....Inverse Square Law

PL……Power Law

θ_{12}…….....Mass ratio

δ_{12}……Stiffness ratio

$\bar{\omega}$……..Normalized frequency

$\bar{\Gamma}$……...Nonlinearity parameter

Γ…….....Normalized nonlinearity parameter

A*…….Normalized amplitude

r……Rate factor

ε……Perturbation parameter

γ_0……..Static inertance Parameter

γ_n……..Nonlinear inertance Parameter

γ_∞…….High frequency limit of the Inertance

L…….....Lattice length

μ…..……..Complex wave number

α…….....Real part of the wave number

β……...Imaginary part of the Wave number

u^*……..Displacement transmissibility

CHAPTER I

INTRODUCTION

1.1 Motivation

Humans have been inventing many things to satisfy their needs and to ease their work. Science has changed human life in a way no one expected. Starting with the invention of the bullock cart to the invention of the car, humans have strived to reduce their effort and improve their comfort. The rapid growth in human population and consequent huge demand on resources has led to considerable automation, which take less time and less human effort to produce many objects.

One key component of such a system is the machine which reduces effort. Every machine under operation is subjected to different types of loads such as thermal load, mechanical load, seismic load, wind load etc. and it has to be designed to withstand these mechanical loads else it may result in adverse effects on the operation of the machines. Vibration is one such example, where the system is constantly moving to and fro with some displacement about the mean position. They have to be carefully designed to withstand these loads, such as a vibration suppression system in which the vibration absorber absorbs the vibrations and damps out the energy. The frequency of vibration and natural frequency of the system should not match otherwise it may lead to resonance and the structure vibrates with more amplitudes and may lead to failure. To avoid this, a vibration isolator can be used, where the system's natural frequency is altered by the isolator and keeps it well below the natural frequency of the system so that resonance is avoided and the system doesn't get damaged.

Instead of vibrations being absorbed by the resonators, they can be used to harvest energy while reducing the vibrations. Several methods have evolved to harvest the unnecessary vibrations. One interesting way to utilize the undesired vibrations is by using an energy harvester, where the vibrations are absorbed by a means of transduction in harvesters and the generated energy is used to charge a battery. Discovered by Michael Faraday in 1831, one means to harvest energy is by electromagnetic induction which uses coils and magnets to harvest energy.

The traditional vibration absorbers used are composed of springs and dampers, which when under load absorb energy. The spring gets compressed and the damper dissipates energy by offering resistance to the load. Depending on the type of load, they need to be modified and designed, for example in an earthquake sustaining bridge design, large springs and dampers are used, which deform and absorb the energy keeping the structure less prone to damage from vibrations. Manufacturing of these large springs and dampers is difficult to produce, uses more material and involves high cost. A suitably designed inerter could serve as a complementary mechanical element in such systems in order reduce overheads.

The inerter which was introduce almost two decades ago has a unique property, inertance which is can provide dynamic mass amplification. It acts as if it has high dynamic mass under loading with relatively small static device mass. In practice, specific inertance (ratio of inertance to static device mass) of up to 300 can be achieved [2]. Using this approach, in addition to springs and dampers for vehicle suspensions systems, vibration isolation systems, and mechanical actuators, an inerter can be used, which significantly improves the performance and also reduces the size and mass of the mechanical system.

1.2 Literature Review

In the traditional analogy as shown in the Figure 1.1, between mechanical and electrical networks a spring is equivalent to an inductor, a damper is equivalent to a resistor, and mass is equivalent to a capacitor, force is equivalent to current, and a fixed end is equivalent to an electrical ground in an inertial frame of reference [1]. In the traditional analogy, the spring is equivalent to a

resistor and the damper is equivalent to the inductor. But there is no perfect equivalence for the non-grounded capacitor. Previously, the mass element was equivalent to a non-capacitor, but, the capacitor can have two active terminals where as one end of the mass element should be grounded and a mass element cannot store energy where as a capacitor can.

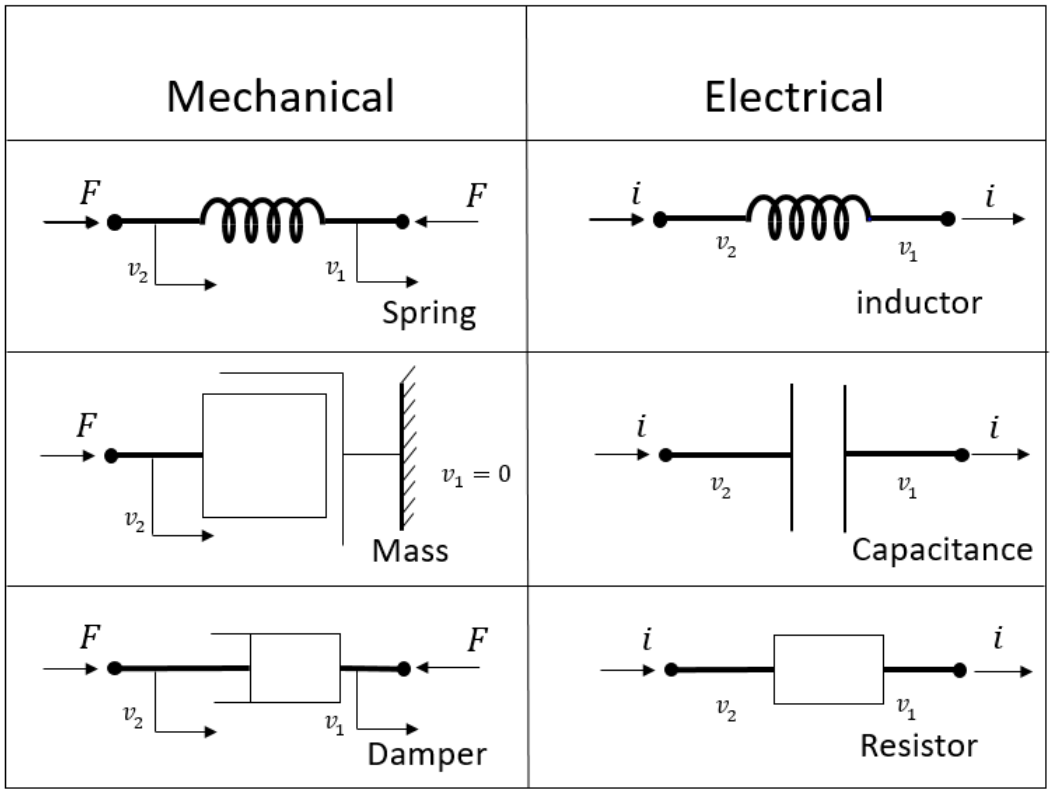

Figure 1.1: Traditional force current analogy [2].

The two terminal capacitor in electrical networks had an incomplete equivalence, there has to be a mechanical device in which the force applied between the two ends is directly proportional to the relative acceleration of the two ends, the Figure 1.2 interprets the question in an easy way.

$$F = k(x_1 - x_2)$$
$$F = c(\dot{x_1} - \dot{x_2})$$
$$F = ?\,(\ddot{x_1} - \ddot{x_2})$$

Figure 1.2: Force response equations showing the incompleteness of the element which relates to the relative acceleration

To complete this analogy, a new element 'inerter' is proposed by Smith [2] in 2002. The inerter is a two terminal mechanical device in which the force applied between the two ends is directly proportional to the relative acceleration of the two ends. The inerter is the missing element in the force current analogy. It is equivalent to a capacitor which stores energy. A mass element has only one active terminal while another terminal is always grounded, but the capacitor can have two active terminals without one being grounded. Electrical networks with two active terminal capacitors do not have a direct mechanical analogy. The inerter is an element which has two terminals and a fly wheel which stores energy.

$$F = J\,(a_1 - a_2) \tag{1.1}$$

In which F is applied force, J is the inertance and a_1 and a_2 are the accelerations of the two terminals. With the invention of an inerter the force-current analogy can be completed as shown in the Figure 1.3 and the perfect equivalence for the capacitor is the inerter.

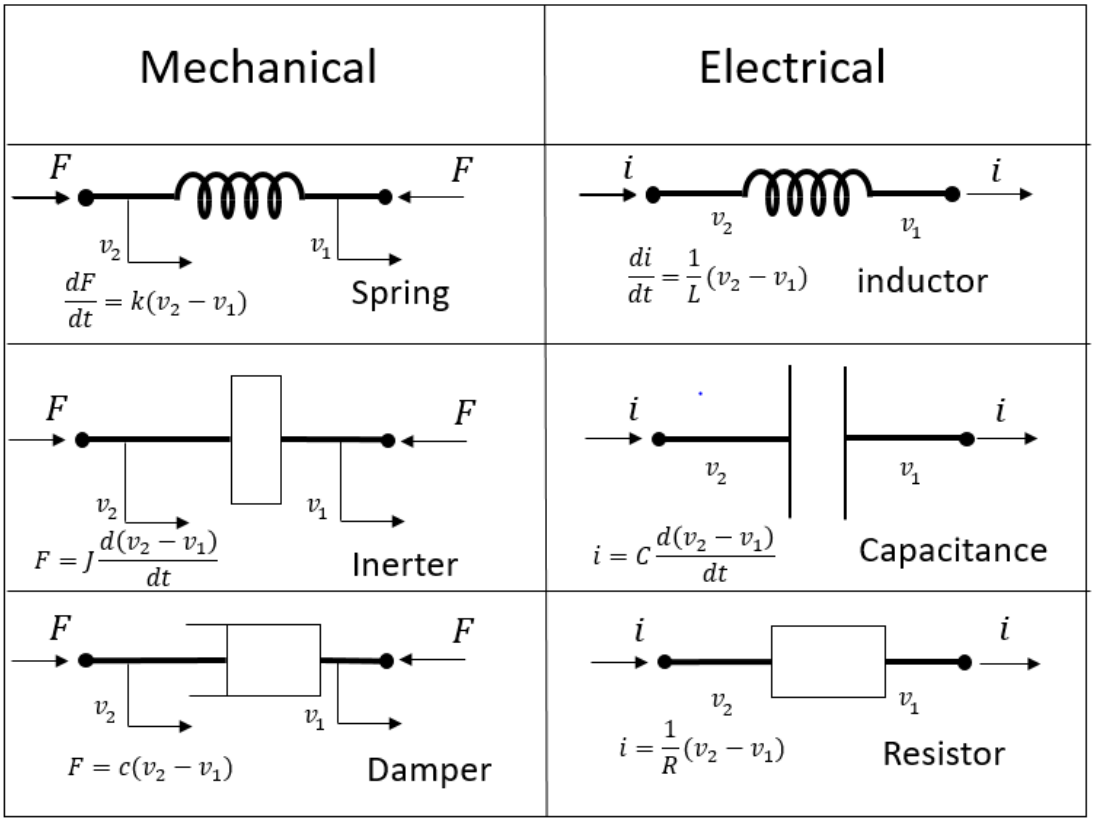

Figure 1.3: Updated force-current analogy [2].

The unique behavior of the inerter, which is the dynamic mass amplification is mostly used in vibration absorption systems and its use has significantly improved the performance over traditional shock absorbers. The physical realizations of the inerter is more important to study so as to understand its nature and its dynamic mass amplification effect. The inerters in practice, can achieve specific inertance of up to 300 which is the ratio of dynamic mass to static mass of the device.

The inerter can be physically realized in many ways. The prominent realizations are rack-and-pinion inerter [3] as shown in the Figure 1.4 is the schematic of rack-and-pinion inerter, in which the force transmission takes place from rack to pinion, pinion to gear, gear to pinion and pinion to flywheel, inertance occurs due to the gear ratios of the gear and pinion.

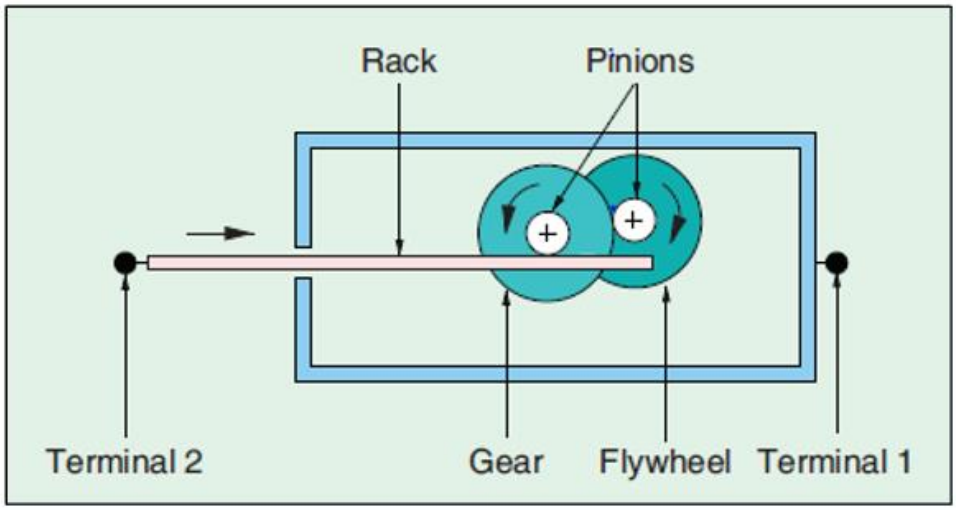

Figure 1.4: Schematic of a rack-and-pinion inerter [10]

Figure 1.5 is the schematic of ball-screw inerter [4, 6], where it has a screw which translates, and the ball-nut rotates which has an attached flywheel. Force transmission takes place from screw to ball-nut, ball-nut to flywheel.

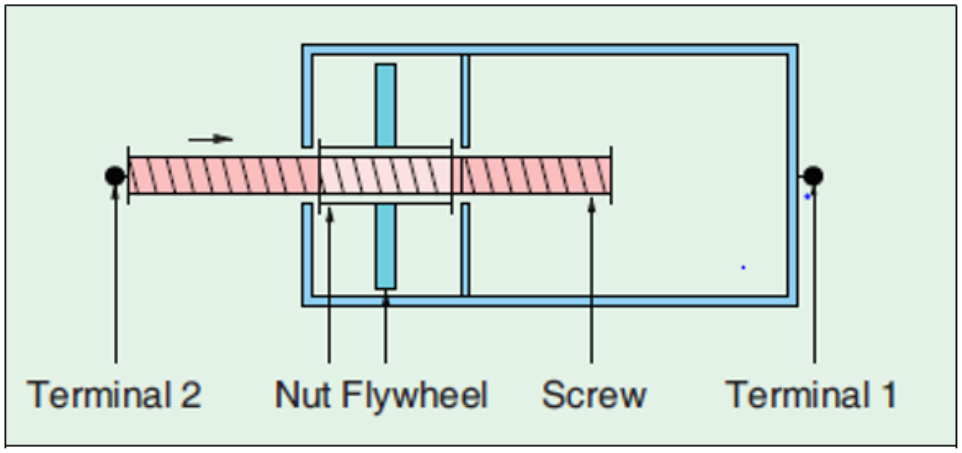

Figure 1.5: Schematic of a ball-screw inerter [4, 6]

Ball-screw inerter is the first ever manufactured inerter at Cambridge University, it is symmetric in nature and simple in construction as shown in the Figure 1.6, it has a ball-screw mechanism and a flywheel.

Figure 1.6: Ball-screw inerter manufactured at Cambridge University [10]

Inerter can be realized in many ways out of which rack-and-pinion and ball-screw inerter are prominent. One more way of realizing an inerter is hydraulic inerter or fluid inerter [7, 8], whose construction is simple but installing the fluid-inerter is way more complex as it has to be used in very confined space and with proper control of pressure. Depending on the type of application and complexity involved different inertant realizations were evolved gradually.

Prime application of inerter was as a vibration absorption system, so its applications are mostly focused on vehicle suspension system. Vehicle suspension is the first ever application of inerter in which the performance was improved significantly [2, 3]. The inerter was employed in eight different suspension layouts [3] including the full car model analytical optimization was done and experiment results of one such layout is reported. Significant performance improvement was observed in the layouts employing inerter.

Wang et al [4] used the inerter in train suspension, where ball-screw inerter was used to study its effect on the different layouts. Five different types of suspension layouts are explained

and analytical results of those layouts were reported and one experiment result of one layout is reported, where the performance was very much observed. The third application was in steering systems of a high performance vehicle [5] where a damper was replaced with an inerter to stabilize the system and study its dynamic behavior, and the computer simulations demonstrate the stabilization of the system and improved performance parameters such as ride comfort, tire grip and suspension displacement.

Papageorgiou and Smith [6] extended the study by testing both ball-screw and rack-and-pinion inerter with a closed loop hydraulic test rig and low frequency response of both the inerters were reported. Both of the inerters were studied to explain their performance relatively. Any physical system has nonlinear properties, these are very tough to predict by experiment or analytical methods Liu et al [9] and Xin et al [12] studied nonlinearities in landing gear model incorporating inerter where the prime focus was to improve the landing gear model for shimmy vibrations and study its nonlinear effects. A Simulink model was used to predict the model [9] and interestingly models with inerter and without inerter were analyzed to compare the performance, model employing inerter showed more improvement in the performance parameters. Wang and Su [11] studied the inerter nonlinearities on vehicle suspension systems, three suspension layouts were analyzed and three nonlinearities of inerter which are friction, elastic effect and backlash were studied.

Further the merits of inerter in semi active suspension system were studied in [13 - 17], where inerter was used in combination with spring and damper strut suspensions, simulations were carried out and they were analyzed on performance parameters like tire grip, road holding capacity, suspension deflection and body acceleration. They make up most of the parameters used to study the performance of a suspension system, drastic improvement was observed in layouts employing inerter.

Kuznetsov et al [18] made an interesting study by employing inerter in a quarter car model for vibration analysis and focuses on comfort level of the passengers. First a theoretical quarter car

model considering kelvin elements is considered and acceleration equations are derived. For numerical examples actual road data of three rural streets is taken and it is used for the analysis. The use of real time data is the merit of this study. Tran and Hasegawa [19] investigated the effect of inertance on the passive suspension by varying the inertance over the model, this research focuses on disturbances of frequency range 0-30 Hz which effects the passenger comfort and comparisons were made with base model and optimized the inertance for the model with more ride comfort. A detail study is made on the suspension layouts by studying it under three different types of engagements in [20] which are compressive engagement, disengagement and extensive engagement, Simulink and experimental data match very well and the model is close to reality. Li [21] investigated the adaptive inerter with varying inertance on a semi-active suspension model, analysis is carried out with different inertances to study the effect of addition of inerter to the system.

A novel structure for Inerter-based Dynamic Vibrational Absorbers (IDVA) is proposed by replacing the damper in the Traditional Dynamic Vibration Absorbers (TDVA) [22] with inerter-based mechanical networks and the performances of the proposed IDVA's are investigated. Hu and Chen [23] introduced a new term IDVA (inerter-based dynamic vibration absorber), in which inerter is used as a vibration absorber, numerical optimization with inerter predicts 20% improvement in the performance in a wider frequency band over traditional devices. The unnecessary oscillations of a pendulum are damped out by employing an inerter, where it is used as a tuned mass absorber [24]. A horizontal forced duffing oscillator is considered as the model. It is shown that by changing the damping and inertance one can eliminate dangerous dynamic instabilities from the systems. A similar study has been made but in single degree of freedom and in multiple degree of freedom systems [25]. Vibration isolations is one of the key areas in which inerter can be used Chen [26] used inerter to study the effect of it on the natural frequency of the single, two and multi degree of freedom systems, where inerter significantly reduced the natural frequency of the system. One more interesting area in which inerter can be used is in building

suspension, [27, 28] have investigated in this area, where the buildings are to be protected against earthquake loads.

The performance improvement in the vehicle suspension using the inerter increases significantly this led the researches to explore more in the field of inerter where adaptive performance can be achieved. An adaptive inerter in which the inertance can be controlled in real time is used in the suspension system [29] and good improvement in the ride comfort is noticed. A quarter car model with an adaptive inerter in parallel with a spring and damper is installed to study effect of adding an adaptive inerter [30] and it is concluded that performance improvement in ride quality, suspension deflection and tire deflection are improved. A theoretical model of a novel type of tuned mass damper with a continuously variable transmission and gear-control system which enables change of inertance is studied to examine its damping properties [31]. The experimental study of the similar inerter was carried out and helps offers damping efficiency within a good range of forcing frequencies [32]. A fluid inerter was used investigated as a passive vibration control [33] where the change in inertance is achieved by using pipe with adjustable radius. A simplified yet authentic model was developed for an inerter-based tuned mass damper including nonlinear effects such as viscous damping and dry friction as well as the play in gears [34]. The nonlinear effects of the geometrical arrangement of the inerter are investigated in terms of vibration isolation and it is compared to the traditional arrangement [35] and shows possible benefits in the high frequency regime. The nonlinearities in the fluid inerter such as friction and nonlinear damping force caused by the viscosity of fluid is investigated [36]. The nonlinearities of the ball-screw inerter on the vibration isolation performance of the vehicle suspension system are investigated [37] and concluded that the vibration isolation performance with the nonlinear ball-screw inerter is slightly increased. The nonlinear effects for low-frequency civil engineering applications are studied using an off the shelf inerter [38]. Most of the research on inerters focuses on structural scale applications such as suspension systems, steering mechanisms, vibration absorption and the effect of natural

frequency of the system with inerter etc., but as the technology is moving towards the micro and nano scale there is a need to realize the inertance and find its applications at a miniature level.

Every material which exists has some kind of nonlinearity, nothing in the nature is linear. Some exhibit nonlinear material properties while some have nonlinear stiffness. Nonlinearity might be in the material or by the geometry. Solving a nonlinear problem is very difficult hence we assume that the system has linearity in some region and solve our analytical models.

On the other hand some structures exhibit negative stiffness which is of particular significance here. Stiffness is the resistance offered by the material or the structure against the applied force. In general stiffness is positive for structures undergoing some kind of displacement under load. But some structures exhibit negative stiffness in some region which means that they exhibit very large displacements even though no force or less force is applied which demonstrates that force and displacement are in opposite direction. Whereas all the systems with positive stiffness oppose the force and tend to increase the resistance with application of excess force in the same direction.

A simple example of achieving negative stiffness regime is using a von Mises truss is shown in the Figure 1.7.

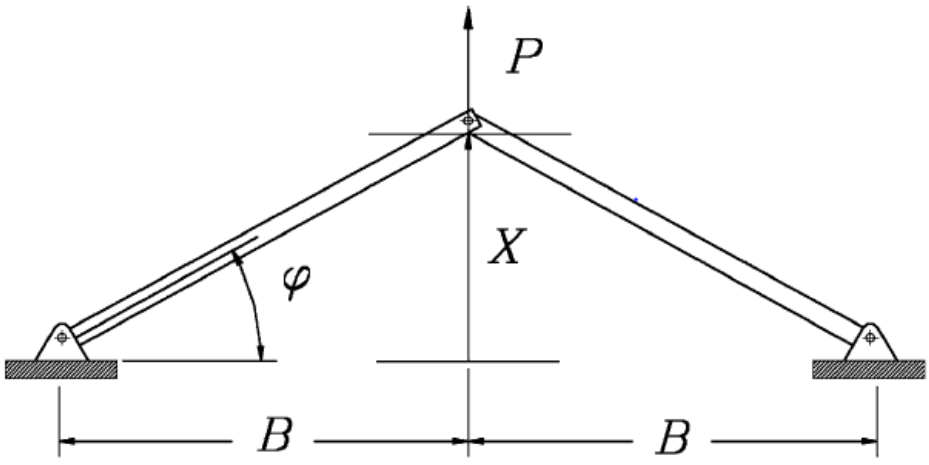

Figure 1.7: von Mises truss having two pin joints [40].

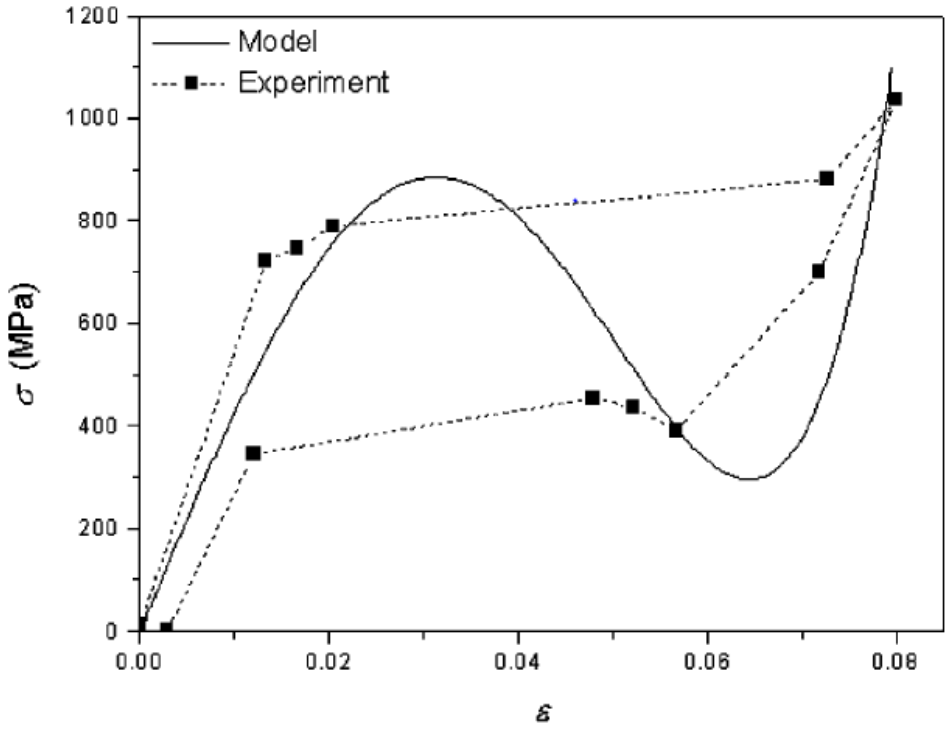

Figure 1.8: Stress-strain curve of the von Mises truss [40].

The truss is acted upon by a force 'P' as shown in the Figure 1.7. Till a certain point stress is directly proportional to strain then the structure exhibits negative stiffness region where the truss just snaps through to second stable position. The truss has two stiffness regimes, the positive stiffness and the negative stiffness regime.

Fulcher et al [40] investigated the applications of buckled and unbuckled beams with negative stiffness in passive vibration and shock isolation systems. Kashdan et al [41] demonstrated the negative stiffness in a buckled beam and had experimental investigation as well, he considered two models one buckled beam and another unbuckled beam, both of them exhibited negative stiffness region but the buckled beam demonstrated more negative stiffness region making it more dominant for other investigations. The characteristics of vibration isolation systems were improved using negative stiffness elements [42].

Barbarino et al [43] investigated the behavior of bi-stable arch by deriving the force equation using Lagrange method and simulated in MATLAB with two different inputs one is

harmonic displacement input and harmonic force input. Further, they extended the research by investigating the behavior under impulsive excitation in [44]. Pontecorvo et al [45] further extended the research by ANSYS simulations of delrin arches and experimental setup of delrin arches and showing that they exhibit negative stiffness. Palathingal and Ananthasuresh [46] have investigated the effect of bi-stability in beams with different boundary conditions, in total six types of beams were investigated and concluded that pinned-pinned configuration had superior bi-stable characteristics.

The need for inventing new materials with unusual properties which are not readily available in the nature is never ending. The technology is progressing rapidly and human needs materials with unusual properties which are not found in naturally occurring materials. Metamaterials are one such materials which are not naturally occurring but man made materials which have unusual properties. These materials derive their unique and unusual properties from the engineered microstructures. The concepts of metamaterials arose long back in the 1880's but the studies on them are relatively recent. They are widely accepted in the fields such as Electromagnetic materials and Acoustic materials.

The thought of metamaterial was first implemented for manipulating EM waves [47, 48, 49] which paved a path for creation of left-handed materials with negative electric permittivity and negative magnetic permeability. The earliest works that paved the path for research in metamaterials was Veselago's paper [50] which postulated the possibility of materials with negative magnetic permeability and electric permittivity. A huge surge of interest in this field began after Pendry [51] proposed the possibility of theoretical left-handed metamaterials.

Over the past few decades significant progress has been made on the metamaterials. Acoustic metamaterials are a class of metamaterials which derive their unique dynamic properties from the locally engineered micro structures that exhibit unusual elastic wave propagation characteristics. The word Meta (meaning beyond in Greek) indicates the ability to offer material properties beyond existing in nature. Depending on their scale of implementation, microstructures

in the context of AM is used as a terminology to refer to engineered local structures and can even be macroscopic. They can be deployed as complex endo structures within functionally exo structures [52] or even as microscopic particulates in a host material [53]. The theoretical possibility of having negative mass density and negative bulk modulus [54, 55] in AM were explored. The presence of such negative properties for materials which are absent in any naturally occurring materials created more interest in these materials. The most prominent case explored in AM is the Locally Resonant Acoustic Metamaterial (LRAM) in which they have a resonator in the local attachments. The frequency-dependent attenuation for sound in a periodic structure was reported by Martinez et al [56] where the test article was a sculpture by Eusebio Sempere exhibited at Juan March Foundation in Madrid. Vincent [57] explored the gap effect for acoustic waves using nonlinear resonators was one of the earliest demonstrations. Using a one dimensional array of elastic membranes, negative effective density below a cutoff frequency was realized by Lee et al [58]. To explain the negative effective mass phenomenon Huang et al [59] presented different analytical models. Huang and Sun [60] presented the existence of more than one stop band for elastic wave propagation for mass in mass system. Many other studies on LRAM were explored using different local resonators. Helmholtz resonator were used as local structures in metamaterials [61], sonic crystals in [62], nonlinear oscillators in [63] and frequency invariant inerters in [64].

Several numerical investigations were carried out to verify the bandgap properties of AM with local nonlinear duffing-type springs [64], linear springs and also with static inerter [65]. Narisetti et al [66] employed nonlinear stiffness in local structures and used a perturbation approach to study the elastic wave propagation characteristics. These studies motivated the investigation of Duffing-type inertance which is discussed in Chapter 4.

1.3 Objectives

Inerter exhibits a distinctive feature of dynamic mass amplification. As discussed in the forgoing section, inerters have inspired several research studies that shed more light on their mechanisms and applications. Overall, the aim of this work is to examine the dynamic characteristics of

structures that employ inerters within the framework of the metamaterials design approach. The applicability of the resultant inertant meta-structures for enriched performance in low frequency structural dynamic scenarios is of interest. In this context, the objectives of this thesis are

- Improve the analytical model of the inerter by including component sizing and inertias so that a simple yet unsimplistic approach for their analysis can be developed.
- Experimentally characterize inertance and the nonlinear influences involved in practical inertant devices.
- Investigate a potential kinematically simpler structure which could provide an inerter-like behavior and be more amenable to microscale implementation.
- To investigate the influence of adding intentionally nonlinear inerter's within the local engineered configurations for AM and to characterize their wave manipulation capabilities.

1.4 Chapter Overviews

The aim of this thesis is to improve the analytical model of the inerter and study the inertance effect experimentally, investigate a potential kinematically simpler structure of inerter which can have an inerter like behavior in miniature scale and study the effect of employing nonlinear inerter's in AM. Chapter 1 deals with the motivation of this study, which deals with the need for conducting this research. It explains in detail about the inerter, its dynamic mass amplification and how it is achieved. It also explains about the past research that is done on this field and brings out the importance of this study and fills the gap of frequency dependence of inerter. It lists out the objectives of this thesis as well.

In Chapter 2 the improved analytical models for two prominent mechanical realizations of the inerter which are ball-screw and rack-and-pinion inerter are demonstrated with necessary line diagrams and 3D models. Force equations for both of these inerter have been derived, with each step in detail. Parametric study for both the inerters have been reported, which explains the dependence of key parameters of the inerter with the specific inertance (J/M_{st}). It is followed by the

fabrication of the test article and experiment setup for the rack-and-pinion inerter. It is tested at two different cases, displacement controlled sinusoidal excitation and acceleration controlled sinusoidal excitation, both the test results have been reported and using a phase matching procedure the internal stiffness and damping of the structure are estimated and they are compared with the discrete element model simulations.

The potential kinematically simpler structure which could give an inerter like behavior is explored in Chapter 3. The Analytical model for the structure is based on a von Mises truss and the equation of motion is derived using Hamilton's principle based on Lagrange's method. Using the equation of motion, a numerical parametric study is performed and the structure is studied under two excitation conditions which are harmonic displacement input and harmonic force input. Finally results are discussed and conclusions are made.

The intentional nonlinearities of inerter and their effect on the AM wave propagation characteristics are investigated in Chapter 4. The notional concepts for realizing nonlinear inertance in practical are discussed using a ball-screw inerter as basis. Two types of inerter nonlinearities are studied which are frequency-dependent and acceleration-dependent. A perturbation approach was used to derive the first order corrections to frequency and displacement for the acceleration-dependent case for weakly nonlinear cases. Then the dispersion curves are simulated and conclusions are made. Finally the conclusions are reported in the chapter 5 and recommendations for future are made.

CHAPTER II

CHARACTERIZATION OF A STRUCTURAL INERTER

2.1 Introduction

The basic mechanical two terminal devices which have an equivalent in electrical networks are the spring, damper and (previously) mass. The existing analogy was inadequate as mass was grounded element. The mass, which is the mechanical equivalent of the grounded electrical capacitor, cannot represent a two-terminal device, since by definition one of its terminals is 'fixed' when its motion is described with respect to an inertial frame of reference. But instead of mass, a new device inerter has been introduced which replaces the mass element which is the inerter. It is a two terminal mechanical device in which force applied between two ends is directly proportional to the difference of accelerations of the two ends. The constant of proportion is termed as inertance, which is akin to a dynamic mass amplification factor. The dynamic mass can exceed the static mass of the device by a few orders of magnitude.

$$F = J\,(a_1 - a_2) \tag{2.1}$$

Where F is the applied force, a_1 and a_2 are the accelerations of the two terminals and J is the inertance which has the units of mass.

The potential applications of an inerter are many chief among them are as a vibration absorption and vibration isolation device. In vibration absorption system, where the vibrations are to be absorbed by a huge mass or high resistance, instead it can be replaced by an inerter with less static mass but has high dynamic mass.

The inertance property of inerter can help absorb more energy and damp out the oscillations more efficiently than a conventional damper. In vibration isolation system where the system has to protected from resonance, inerter can detune the natural frequency of the system due to its high dynamic mass, therefore by increasing the dynamic mass it reduces the natural frequency of the system and can keep it well below the excitation frequency of interest.

2.2 Analytical Model

Analytical models for specific inertance that include component inertias and sizing but retaining rigid body assumptions are developed for both the ball-screw and rack-and-pinion embodiments of the inerter. Firstly, detailed designs that account for functional components for both versions were created. Equations of motion were derived for these designs, and parametric studies were undertaken to extract the dependencies for specific inertance.

2.2.1 Analytical Expressions for Specific Inertance

The inerter can be mechanically realized in many ways, out of which the most prominent ones are the ball-screw inerter and rack-and-pinion inerter. Both achieve the inertance through the rotation of flywheel which is achieved through a series of rack, gear and pinions, while the former one uses a ball-screw mechanism.

Ball-screw inerter is the mechanically simpler realization of the inerter. It transmits motion to its flywheel using a ball-screw mechanism. It converts the translation motion of screw to rotational motion of the ball nut and the flywheel is attached to the ball nut. Hence when the nut rotates the flywheel will also rotate.

Figure 2.1 shows the 3D CAD model of a ball-screw inerter design, which is based on Commercial Off-the-shelf components (COTS). Its principal components are two thrust bearings, a fly wheel, the ball-screw unit and its nut, and an external casing to house the rotary components. From a mechanical standpoint, the ball-screw version is the simpler of the two versions considered here. One end of the screw acts as the first terminal of the inerter, while the casing acts as the other.

Force transmission occurs from the screw through the nut, flywheel, and bearings to the casing. Both axial and rotary dynamic balancing are easier to accomplish using the ball-screw design.

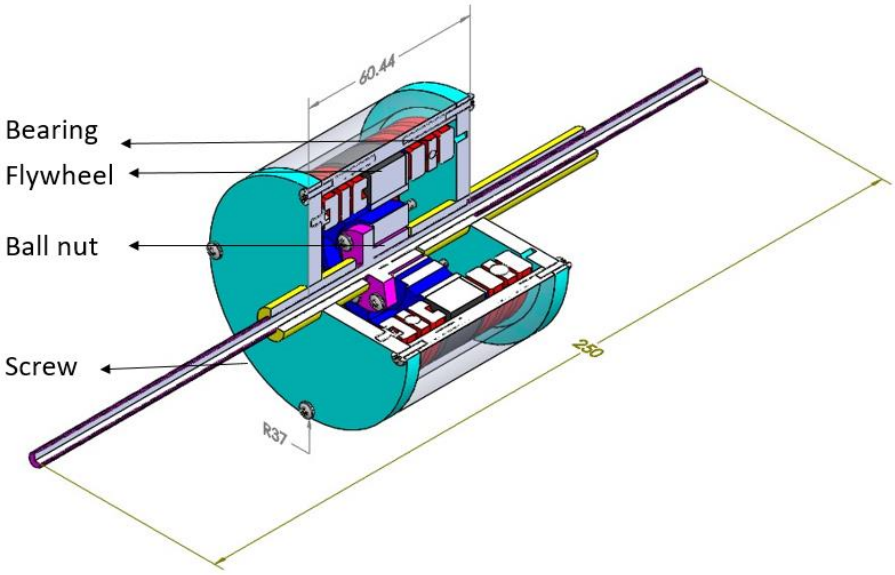

Figure 2.1: Ball and screw inerter CAD model. Units: mm

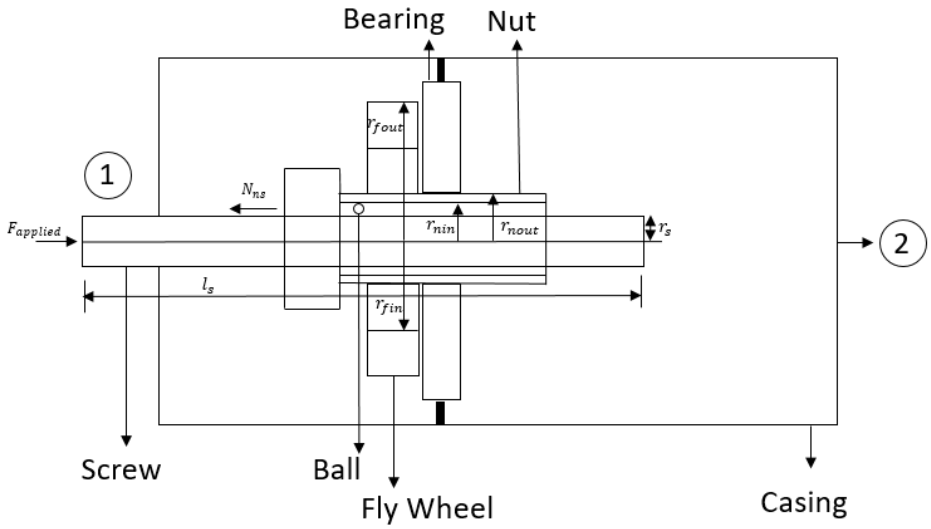

Figure 2.2: Line diagram of ball and screw inerter showing forces and geometric parameters

A line diagram with forces and geometric parameters for the ball-screw design is shown in Figure 2.2 For the purposes of this analysis, a force is assumed to be applied to terminal 1 (i.e., the screw) and terminal 2 (casing) is assumed to be encastred as shown in Figure 2.2. The screw is

assumed to have rotation about its axis and translation in the axial direction alone. The effect of friction and other sources of damping as well as gravity are neglected.

Consider a ball-screw inerter with the second end fixed as shown in Figure 2.2, the equation of motion for screw in axial direction is:

$$F_{applied} - N_{ns} = m_s a_s \tag{2.2}$$

Where, $F_{applied}$ is the Force applied on the screw, N_{ns} is the normal reaction of nut on screw, m_s is the mass of the screw and a_s is the acceleration of screw.

Now, assuming that nut it rigidly connected to the flywheel, the rotational equation of motion for nut and flywheel due to the axial motion of the screw is as follows:

$$\frac{N_{sn}L}{2\pi} = (I_n + I_f)\alpha_n \tag{2.3}$$

Where, N_{sn} is the normal reaction of screw on nut, L is the lead of the screw, I_n is the moment of inertia of nut, I_f is the moment of inertia of flywheel and α_n is the angular acceleration of nut.

Now, expressing the linear accelerations of screw in terms of angular acceleration of nut, one can directly note that $\alpha_n = \frac{2\pi}{L} a_s$

Where, a_s is the acceleration of screw, L is the lead of the screw and α_n is the angular acceleration of nut.

Simplifying Equations 2.2 and 2.3 and using the acceleration relationship we finally get the force equation as

$$F_{applied} = \left[\left(\frac{m_n r_n^2}{2} + m_f k^2\right)\left(\frac{2\pi}{L}\right)^2 + m_s\right] a_s \tag{2.4}$$

Where, m_n is the mass of nut is, m_f is the mass of flywheel and k is the radius of gyration of flywheel. Rewriting the above equation by comparing it with the Equation 2.1 in terms of inertance J and the static mass of the inerter, M_{st} one can obtain the expression for the specific inertance for this device as:

$$\Upsilon_{BS} = \left(\frac{J}{M_{st}}\right)_{BS} = \frac{\left(\frac{m_n r_n^2}{2} + m_f k^2\right)\left(\frac{2\pi}{L}\right)^2}{M_{st}} + \frac{m_s}{M_{st}} \tag{2.5}$$

This equation expresses the specific inertance for a ball-screw inerter in terms of component inertias and sizing parameters.

The rack-and-pinion inerter was one of the first manufactured inerters. In this inerter force transmission takes places through series of gears and pinions. The CAD model for the rack-and-pinion inerter is shown in the Figure 2.3, in order to reveal the internal mechanism, the top and front panels are removed in the figure. It is complex in construction compared to the ball-screw inerter as it has a rack, two pinions, one gear, two shafts, bearings and a fly-wheel as its major components. Force transmission takes place from the rack, which is the first terminal, through its pinion, then to the gear and its pinion and finally to fly-wheel.

The red colored component is the gear, the green ones are the pinions (which are the same in the paper), the blue one is the rack, the yellow colored component is the flywheel which is an aluminum ring of 4 inch outer and 3 inch inner diameter and 1 inch thickness, and it is attached to the shaft with the help of a 3D printed structure. The aluminum ring and the 3D printed structure are bolted together, and the structure has the facility to bolt to the shaft.

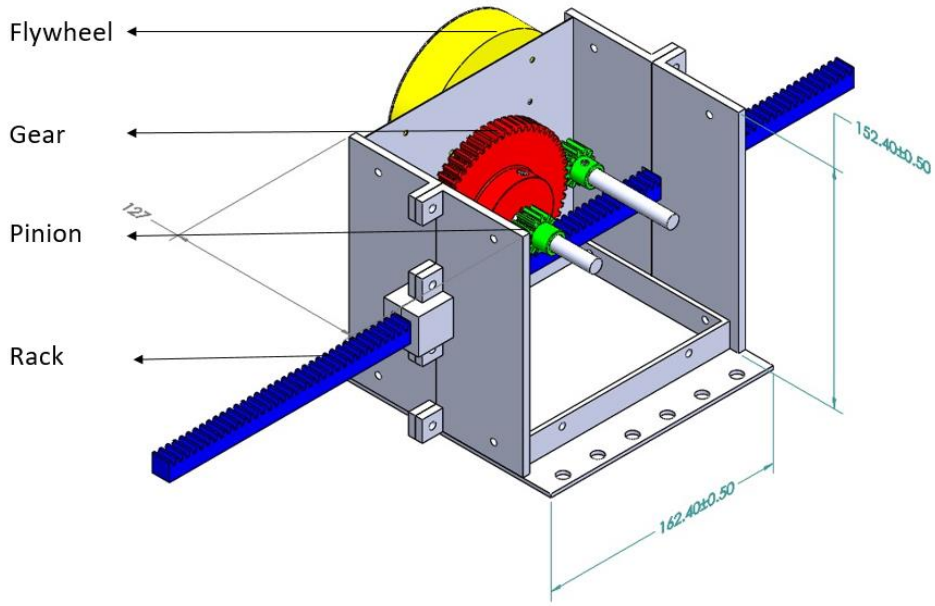

Figure 2.3: Rack-and-pinion inerter CAD model. Units: mm

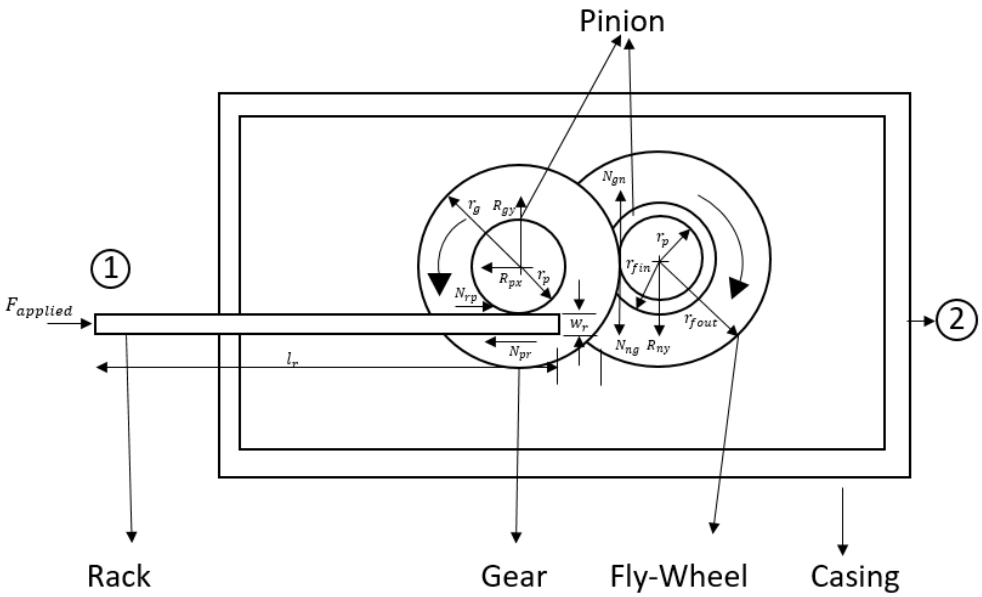

Figure 2.4: Line diagram of rack-and-pinion inerter showing forces and geometric parameters

Consider a rack and pinion inerter with the second end fixed as shown in Figure 2.4, then the equation of motion of rack is as follows.

$$F_{applied} - N_{pr} = m_r a_r \tag{2.6}$$

Where, $F_{applied}$ is the Force applied on the rack, N_{pr} is the normal reaction force due to rack's pinion on rack, m_r is the mass of the rack and a_r is the acceleration of rack.

Now, writing the equations of motion for pinion and gear in the x direction, y direction and moment equation in z direction we have.

$$-R_{px} + N_{rp} = 0 \tag{2.7}$$

$$-R_{gy} + N_{ng} = 0 \tag{2.8}$$

$$-N_{rp} r_p + N_{ng} r_g = \left(I_p + I_g\right)\alpha_p \tag{2.9}$$

Where, R_{px} is the reaction force on the pinion in x direction due to the casing, N_{rp} is the normal reaction force due to the rack on rack's pinion, R_{gy} is the reaction force on the gear in y direction due to the casing, r_p is the radius of pinion, r_g is the radius of gear, I_p is the moment of inertia of pinion and I_g is the moment of inertia of gear and α_p is the angular acceleration of the rack's pinion.

Now, writing the equations of motion for pinion and flywheel in y direction and moment equation in z direction we have.

$$-R_{ny} + N_{gn} = 0 \tag{2.10}$$

$$N_{ng} r_n = \left(I_n + I_f\right)\alpha_n \tag{2.11}$$

Where, R_{ny} is the reaction force on the gear's pinion in y direction due to the casing, N_{gn} is the normal reaction force of gear on gear's pinion, r_n is the radius of the gear's pinion, I_n is the moment of inertia of the gear's pinion and I_f is the moment of inertia of the flywheel.

Now, the accelerations for all the components can be related through the expressions, $a_r = a_p, a_r = \frac{r_p}{\alpha_p}, a_n = a_g,$ and $\alpha_n = r_g a_p / r_n r_p$

Where, r_g is the radius of the gear, a_p is the acceleration of rack's pinion, r_n is the radius of gear's pinion and r_p is the radius of rack's pinion.

Now using the Equations 2.6, 2.9, 2.11, and acceleration relationships we derive the force equation for rack and pinion inerter as

$$F_{applied} = \left[\frac{\left(\frac{m_n r_n^2}{2} + m_f k^2 \right) r_g^2}{r_p^2 r_n^2} + \frac{\left(m_p r_p^2 + m_g r_g^2 \right)}{2 r_p^2} + m_r \right] a_r \tag{2.12}$$

Where, $F_{applied}$= applied force, m_n = mass of pinion, r_n = radius of second pinion, m_f = mass of flywheel, k = radius of gyration of flywheel, r_g = radius of gear, r_n= radius of second pinion, r_p= radius of first pinion m_p = mass of first pinion, m_r= mass of rack, and a_r= acceleration of rack.

Rewriting Equation 2.12 in terms of inertance (*J*) and dividing the equation by static mass of the inerter, we have

$$\Upsilon_{RP} = \left(\frac{J}{M_{st}} \right)_{RP} = \frac{\left(\frac{m_n r_n^2}{2} + m_f k^2 \right) r_g^2}{r_p^2 r_n^2 \, M_{st}} + \frac{\left(m_p r_p^2 + m_g r_g^2 \right)}{2 r_p^2 M_{st}} + \frac{m_r}{M_{st}} \tag{2.13}$$

Where, *J* = inertance and M_{st}= static mass of the inerter

This relationship (Equation 2.13) expresses the specific inertance of a rack and pinion inerter in terms of its component inertias and sizing.

2.3 Numerical Parametric Study

The parametric dependencies for the specific inertance of both ball-screw and rack-and-pinion inerters are explored using numerical simulations. They help in establishing the feasible design space and aid the selection of component. Observing the expressions for specific inertance, it can be easily seen that specific inertance depends on different parameters with varying degrees of influence. For designing an inerter of known inertance it is important that we know the optimum

values of the parameters for specific application and design constraints. For this, parametric curves are advantageous. If any parameter needs to be constrained, then it is easy to find the remaining parameters, and it is easy to check if the design is feasible or not with a given set of parameters.

The parametric curve is a curve drawn between two variables while other parameters are kept constant. The parameter is varied between the limits for possible design values in order to understand the nature of its dependency. The expressions for specific inertance are adopted for the geometries of the component designs as follows.

For the ball-screw inerter from Equation 2.5 substituting $M_{st} = m_s + m_n + m_f + m_b + m_c$ where, subscripts s, n, f, b, and c denote the screw, nut, flywheel, bearing, and the casing, respectively. The mass of the fasteners and other miscellaneous components are lumped with the casing. Now, simplifying into corresponding density and thickness we have the following equation. It is deduced so that it is easy to know the dependency of the different variables on the inertance J.

$$\Upsilon_{BS} = \left(\frac{J}{M_{st}}\right)_{BS} = \frac{\left[\rho_n t_n (r_{nout}^4 - r_{nin}^4) + \rho_f t_f \left(r_{fout}^4 - r_{fin}^4\right)\right] 2\pi^3/(L^2) + \rho_s l_s r_s^2 \pi}{\left[\pi\rho_n t_n (r_{nout}^2 - r_{nin}^2) + \pi\rho_f t_f \left(r_{fout}^2 - r_{fin}^2\right) + \pi\rho_s l_s r_s^2 + \ m_c + m_b\right]} \tag{2.14}$$

In the above expression t_n and t_f represent the axial thickness for the nut and the flywheel respectively, while l_s represents the axial length for the screw. The key parameters explored here are the inner and outer radius of flywheel and the nut within the bounds of the available sizing. The reference parameter is chosen as the lead of the screw. Remaining parameters are kept constant. Table 2.1 lists the base parametric setting used for the ball-screw inerter design.

Table 2.1: Key components of the ball-screw inerter and their parametric values.

Component	Parameter	Value
Nut	Density	7890 kg/m^3
	Thickness	17 mm
	Outer radius	5.5 mm
	Inner radius	2 mm
Flywheel	Density	7890 kg/m^3
	Thickness	13 mm
	Outer radius	30 mm
	Inner radius	20 mm
Ball-Screw	Density	7890 kg/m^3
	Length	250 mm
	Radius	2 mm
	Lead	5 mm
Casing	Mass	0.2 kg
Bearing	Mass	0.174 kg

A ball-screw is a device which converts linear motion to rotational motion and frictional forces are dominant and contribute to significant losses. Due to the frictional force and the sizing of the screw they can sometimes be 'self-locking'. The self-locking condition is given by $\mu\pi d < L$, where μ is the coefficient of friction, d is the mean diameter of the screw, and L is the lead. When the lead is sufficiently small for a particular diameter of the screw the locking force will be high and it is becomes difficult to move the screw, and hence lead should be sufficiently high. Assuming the coefficient of friction μ between mating surfaces as 0.3, and the diameter of screw as fixed at 4 mm, a lead of 5 mm ($> \mu\pi d = 3.8\,mm$) is used to prevent self-locking.

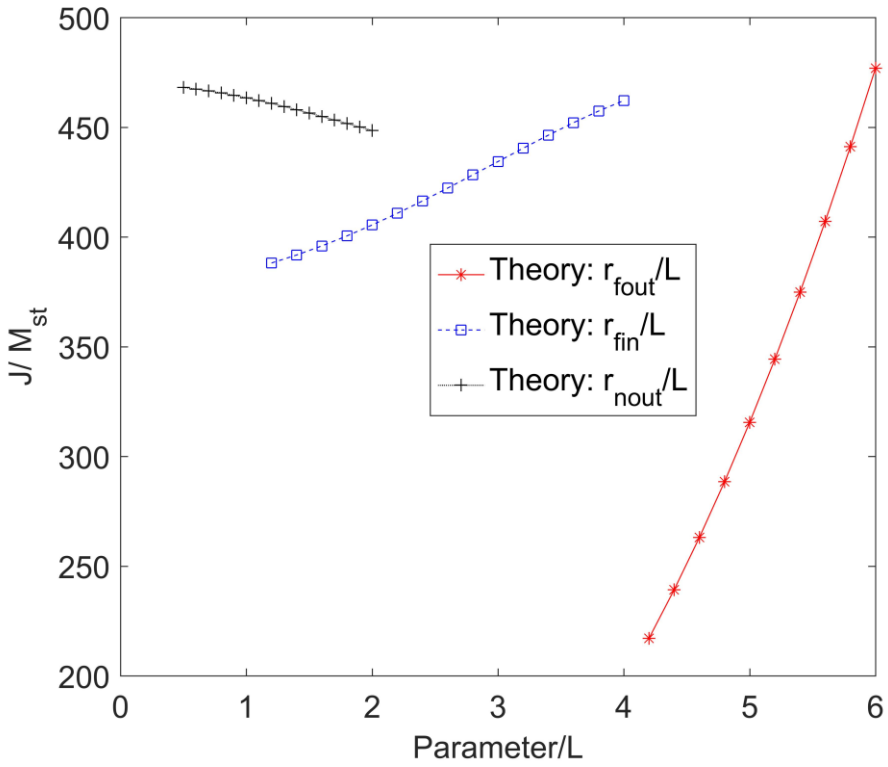

Figure 2.5: Parametric curves of ball-screw inerter. L: lead of screw

Figure 2.5 depicts the variation of specific inertance of the ball-screw inerter with the key parameters. For each parametric variation other parameters involved are invariant. It is seen that the specific inertance can be changed drastically if outer radius of flywheel is increased, this is explainable because the outer radius of flywheel influences the size and mass of the flywheel. The specific inertance increases with increase in the inner radius of the flywheel but less compared to the outer radius of flywheel this is because, increasing the inner radius of flywheel decreases the mass but also increases its radius of gyration. Further, an increase in the size of the nut somewhat decreases the specific inertance. Overall, among the key parameters, it is desirable to minimize the radius of the nut, and maximize the inner and outer radii of the flywheel for the given choice of the other fixed parameters. Under the design constraints of the components chosen, specific inertance up to about 450 is seen to be achievable through an optimal choice of key parameters.

Similarly for rack-and-pinion inerter, from Equation 2.13 substituting the static mass of the rack-and-pinion inerter as $M_{St} = m_r + 2m_p + m_g + m_f + m_c$ where, the subscripts r, p, g, f and c stand for the rack, pinion, gear, flywheel and casing. As the rack's and the gear's pinions are identical, a separate symbol is not introduced, but twice the mass of the rack's pinion is used to account for the two pinions. The mass of the static shafts, bearings, fasteners, and other miscellaneous components are lumped with the casing. Introducing component densities, and expressions for volumes, radius of gyration, and mass moment of inertia, the specific inertance in terms of independent fundamental parameters can be expressed as:

$$\Upsilon_{RP} = \left(\frac{J}{M_{st}}\right)_{RP} = \frac{\{[\rho_p t_p r_p^4 + \rho_f t_f (r_{fout}^4 - r_{fin}^4)] r_g^2 \pi\}/2r_p^4 + (\rho_p t_p r_p^4 + \rho_g t_g r_g^4)\pi/2r_p^2 + \rho_r l_r w_r t_r}{[2\pi\rho_p t_p r_p^2 + \pi\rho_f t_f (r_{fout}^2 - r_{fin}^2) + \pi\rho_g t_g r_g^2 + \rho_r l_r w_r t_r + m_c]} \tag{2.15}$$

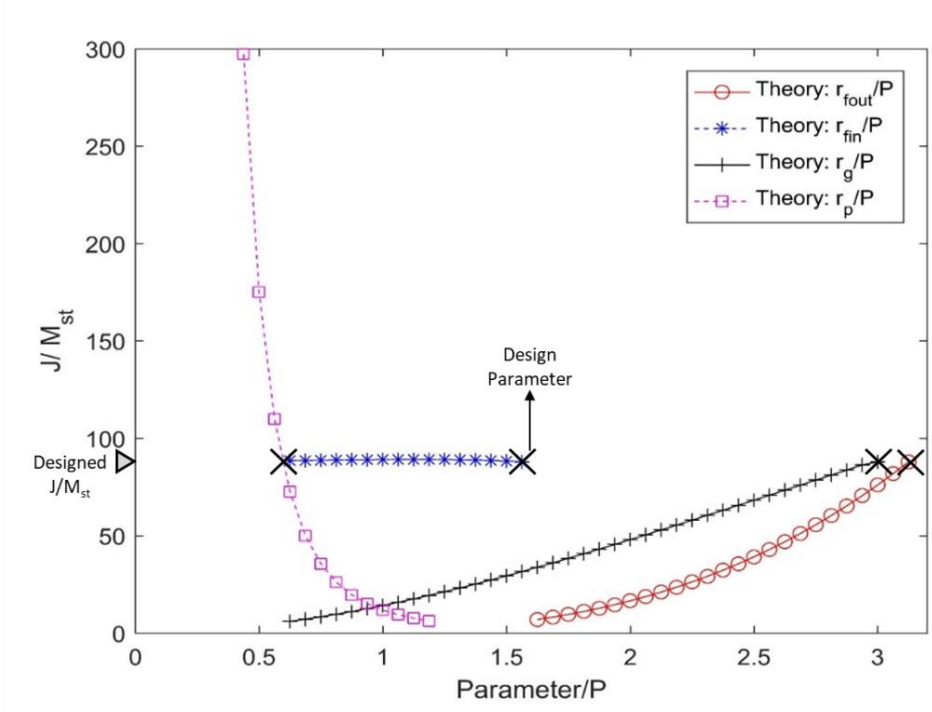

Figure 2.6: Parametric curves of rack-and-pinion inerter. P: pitch of gear/pinion

Table 2.2: Key components of the rack-and-pinion inerter and their parametric values.

Component	Parameter	Value
Gear	Density	7890 kg/m^3
	Thickness	13 mm
	Outer radius	47.6 mm
	Inner radius	6.4 mm
	Pitch	16 mm
Flywheel	Density	7890 kg/m^3
	Thickness	25.4 mm
	Outer radius	50.8 mm
	Inner radius	25.4 mm
Pinion	Density	7890 kg/m^3
	Thickness	13 mm
	Outer radius	9.5 mm
	Inner radius	6.4 mm
	Pitch	16 mm
Rack	Density	7890 kg/m^3
	Length	500 mm
	Width	12.7 mm
	Pitch	16 mm
Casing	Mass	0.3 kg

In Equation 2.15, the symbol t pertains to the out-of-plane thickness for the subscripted components, while l_r and w_r are the length and width of the rack. Also, since the rack and gear pinions are identical, they are sized without distinction through the use of the same radius and thickness parameters. The base parametric setting for the rack-and-pinion inerter design is listed in Table 2.2.

Figure 2.6 depicts the variation of specific inertance (J/M_{st}) for the rack-and-pinion inerter with key sizing parameters nondimensionalized by the pitch of the rack. The selected designed

points for each parameter are marked using black ‘X’ mark. The design value of specific inertance is marked on the vertical axis. It can be seen that the specific inertance has highly sensitive to the radius of pinion. This is because the participation of the pinion radii terms in the denominator. The specific inertance remains almost constant with the inner radius of flywheel this is because it increases the radius of gyration of flywheel, but at the same time decreases the mass of the flywheel. Both radii of gear and outer radius of flywheel show an increasing dependence on the specific inertance as they have a dominant influence on the rotary inertia. Overall it is desirable to have smaller pinion radii, larger gear and outer radius of flywheel for the design to have higher specific inertance.

2.4 Test Article Design and Fabrication

A prototype rack-and-pinion inerter that was fabricated is shown in the Figure 2.7, it has an inertance of 180 kg and static mass of 2 kg, providing a specific inertance of 90. It has two pinions, one gear, one rack, two shafts, four bearings and a flywheel which are commercial off the shelf (COTS) components.

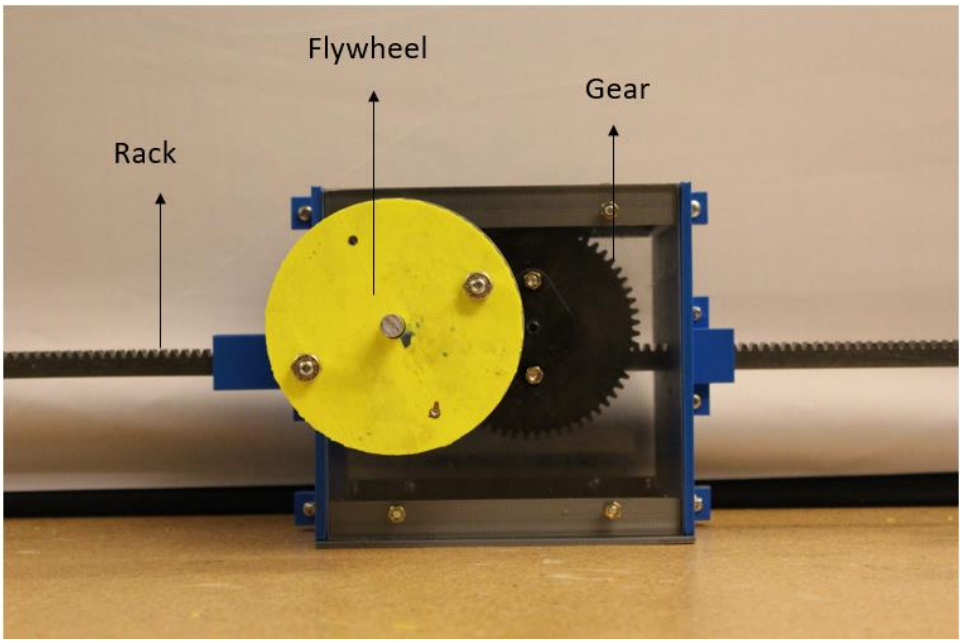

Figure 2.7: Rack-and-pinion inerter

Table 2.3: Summary of components for the rack-and-pinion inerter

S. No	Component	Material	Density (kg/m^3)	Key parameter	Fabrication
1	Rack	Steel	7890	l_r (length)	COTS
2	Pinion(s)	Steel	7890	r_p (radius)	COTS
3	Gear	Steel	7890	r_g (radius)	COTS
4	Flywheel	Aluminum	2800	r_f (radius)	COTS
5	Casing	PLA	1250	m_c (mass)	3D printed
6	Hub	PLA	1250	-	3D printed

The yellow colored 3D printed part as shown in the figure is a structure to support flywheel which is an aluminum ring. Two acrylic sheets are used to reveal the internal mechanism and the casing is made up of 3D printed structures using a desktop three-dimensional (3D) printer, the base of the inerter is printed with holes which are used to mount the inerter to the vibration isolation table firmly.

Table 2.3 summarizes the components used for manufacturing the rack-and-pinion inerter with key parameters and their details.

2.5 Experimental Setup and Procedures

The test setup is built on a vibration isolation table with an electro-dynamic shaker (ET-140 from Labworks Inc.) and the inerter connected to its actuator with the help of 3D printed fixtures. Inerter and electro-dynamic shaker are firmly mounted to the table so that they will not have any relative movement during the experiment.

The electro-dynamic shaker receives its input from a waveform generator, which is connected to an amplifier, which amplifies the signal. In between the shaker and rack (terminal-1), there is an inline type load cell as shown in the Figure 2.8 which has a maximum load capacity of 1000 lb. with 0.1 lb. sensitivity which reads the load that is being applied by the shaker on the rack. The load cell has external thread cuttings which is used to mount the load cell inside the adaptor fixture as shown in the Figure 2.9 which has internal thread cuttings. The adaptor fixture is designed with bolt holes to attach it to the shaker head firmly.

Figure 2.8: LCM 200 load cell.

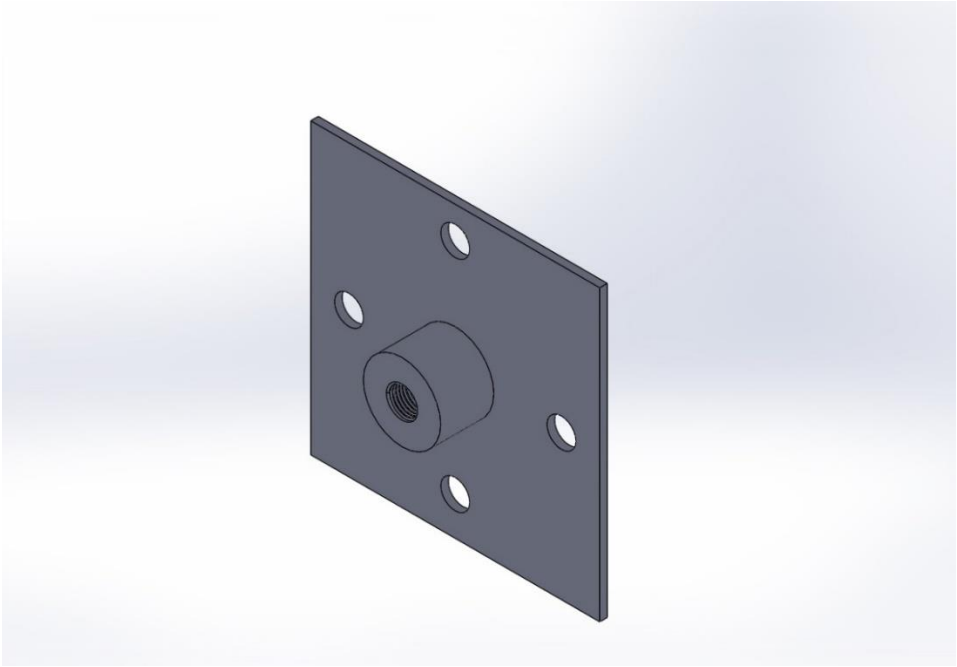

Figure 2.9: 3D model of the fixture between shaker head and the inerter

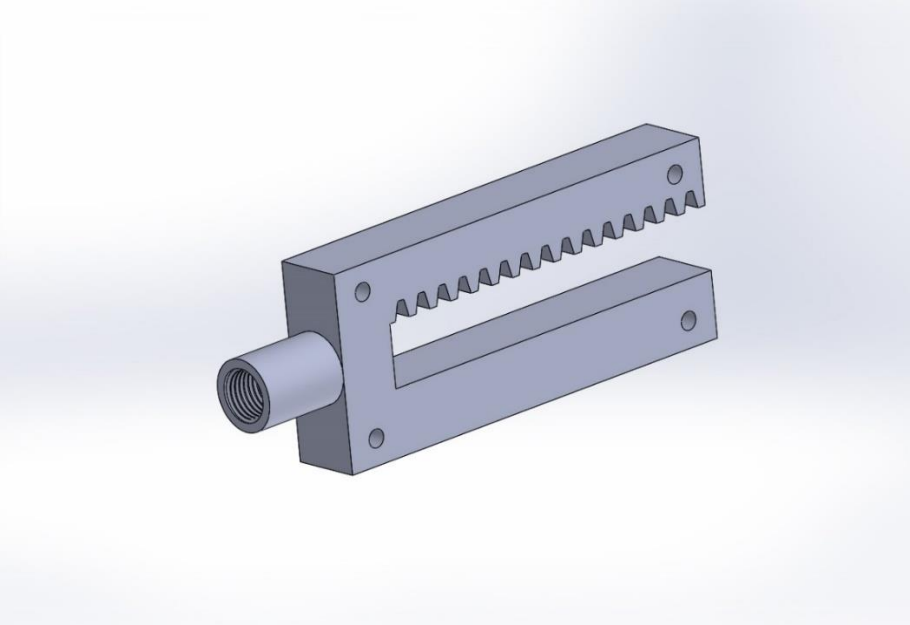

Figure 2.10: 3D model for the fixture between load cell and rack

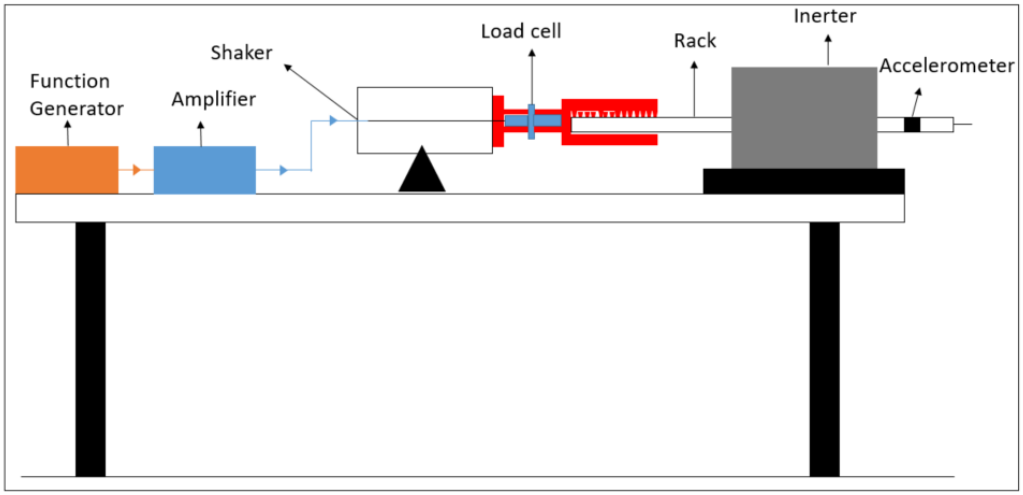

Figure 2.11: Schematic of structural scale inerter experiment setup

Similarly, an attachment between the load cell and the inerter has been designed using Solid-works which can be used connect the load cell and the inerter's rack. The inerter receives its input from a rack, and the load cell has external thread cuttings, hence an attachment was designed which can connect these both. The designed fixture has female thread cuttings which can be attached to the load cell. For attaching the fixture to the rack, a similar tooth profile is 3D modelled

so that the teeth will mate with the inerter's rack. This will ensure a firm fix between the attachment and the rack. Figure 2.10 is the CAD model of the fixture between the load cell and the rack. To prevent the sideways motion of the rack, two side plates are fabricated which have four holes and can be used to bolt the two plates to the fixture. Accelerations are measured by a single axis B&K (4507) accelerometer which has a sensitivity of 10 mV/ms^{-2}, and it is mounted to the rack.

Figure 2.11 is the schematic of the inerter's experiment test setup, first the type of wave and the amplitude of the wave are set in the function generator which is the Key sight waveform generator here, and these are pre-amplified by Labworks pa-141 power amplifier before they are fed into the shaker. The amplifier receives its input from the function generator where a constant level of amplification is used for each type of test case. A Labworks ET-140 shaker is used for the experiment which is a moving armature type 110 lbf capacity electro dynamic shaker. The Labworks pa-141 amplifier is equipped with a gain control which can amplify up to 40 dB voltage gain.

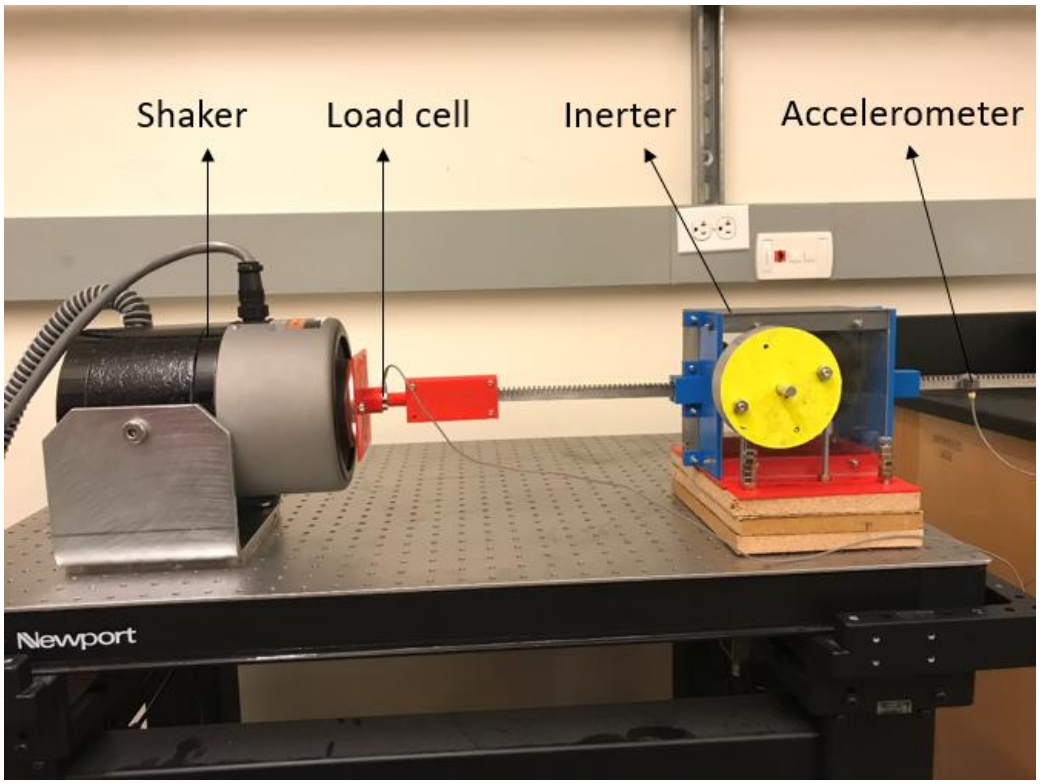

Figure 2.12: Rack-and-pinion inerter test setup with electro-dynamic shaker

Figure 2.12 is the picture of the experiment setup which has all the components, a shaker which is connected to the load cell with the help of 3D printed fixtures, the inerter which is the test article and the accelerometer which reads the acceleration of the rack.

Inerter is tested at two test cases based on excitation type one displacement control sinusoidal excitation (DCSE) and another acceleration control sinusoidal excitation (ACSE). First, an accelerometer is connected to the shaker head and LabVIEW code is built which displays the acceleration and displacement of the accelerometer which is connected to the shaker. First for DCSE case, the amplifier level is kept constant and the voltage in the waveform generator is increased till the desired displacement of 7-8 mm is achieved and voltage is noted down for the corresponding frequency, this procedure is repeated for different frequencies and the corresponding voltage and frequency is noted. Similarly for the ACSE case using the same LabVIEW code, accelerations are observed and same procedure is repeated until acceleration of 3.5 m/s^2 is achieved and the corresponding frequency and voltage is noted down, this is repeated for other frequencies and the corresponding voltages are noted.

For the experiment, first the voltage and frequency are inputted in the waveform generator and the signal is inputted to amplifier which amplifies the signal and inputs the amplified signal to the shaker, next the LabVIEW code is ran and then the amplification level is tuned to the fixed value. LabVIEW code is ran prior to amplifier so that the initial transition data is not missed. The experiment will be stopped once the steady state in the load cell is achieved, and the load cell and accelerometer data is saved. Three sets of experiments are ran for consistency. This is repeated for acceleration case and the load cell and acceleration histories are saved. The results are displayed in the following section.

2.6 Results and Discussions

In this section firstly, the results from two test cases - Displacement-Controlled Sinusoidal Excitation (DCSE) and Acceleration-Controlled Sinusoidal Excitation (ACSE) are presented and discussed. Then the histories of load and acceleration readings are used to calculate the specific

inertance (J/M_{st}). Finally, the specific inertance values are used to plot the variation with the excitation frequency.

2.6.1 Displacement Controlled Sinusoidal Excitations

In this section, the inerter is tested at displacement controlled sinusoidal excitations at different frequencies under 5 Hz. Load and acceleration histories for frequencies 0.5 Hz, 1 Hz, 2 Hz, 3 Hz, 4 Hz and 5 Hz are shown in the Figures 2.13 - 2.18. In all the cases the load and acceleration histories are time synchronous, and the history for the first 8 s from start-up is shown. For each frequency, the post start-up transient data is used to extract the average peak load and average peak acceleration in order to compute the specific inertance, J/M_{st} as per Equation 2.16 below:

$$\frac{J}{M_{st}} = \frac{< |F_{peak}| >}{< |a_{peak}| > M_{st}} \tag{2.16}$$

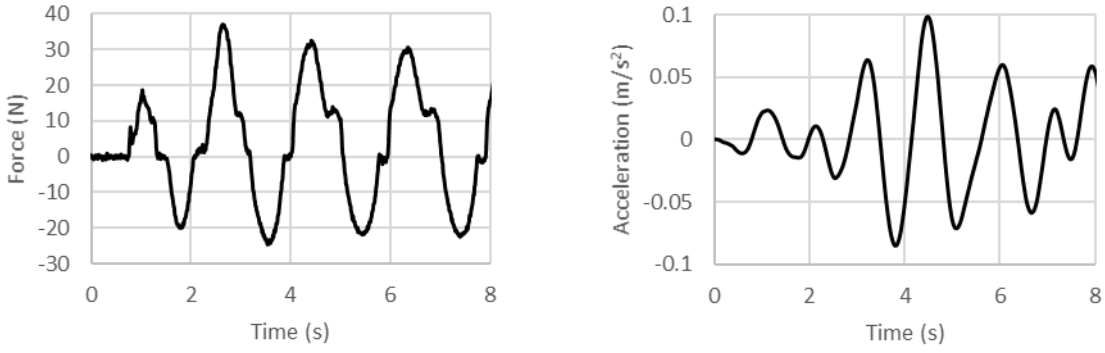

(a) *(b)*

Figure 2.13: Experimental (a) force and (b) acceleration histories at 0.5 Hz under displacement control.

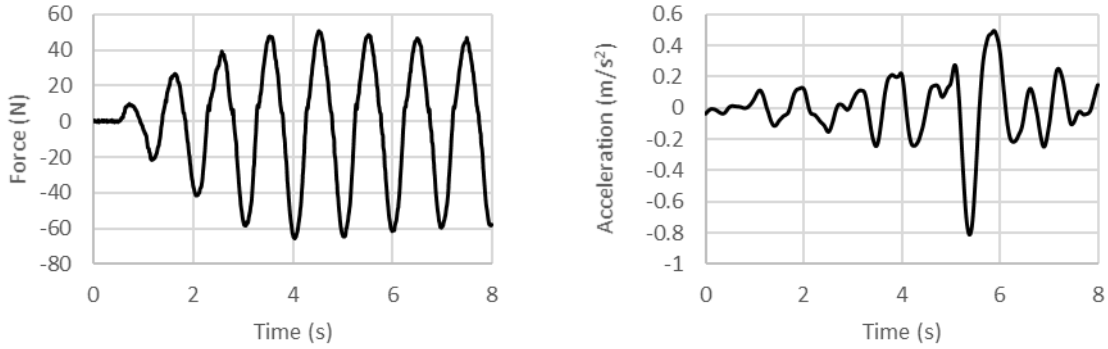

(a) *(b)*

Figure 2.14: Experimental (a) force and (b) acceleration histories at 1 Hz under displacement control.

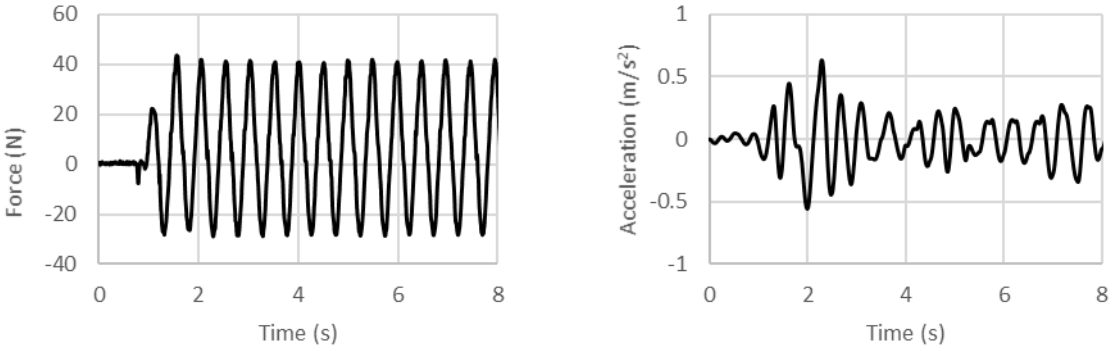

(a) *(b)*

Figure 2.15: Experimental (a) force and (b) acceleration histories at 2 Hz under displacement control.

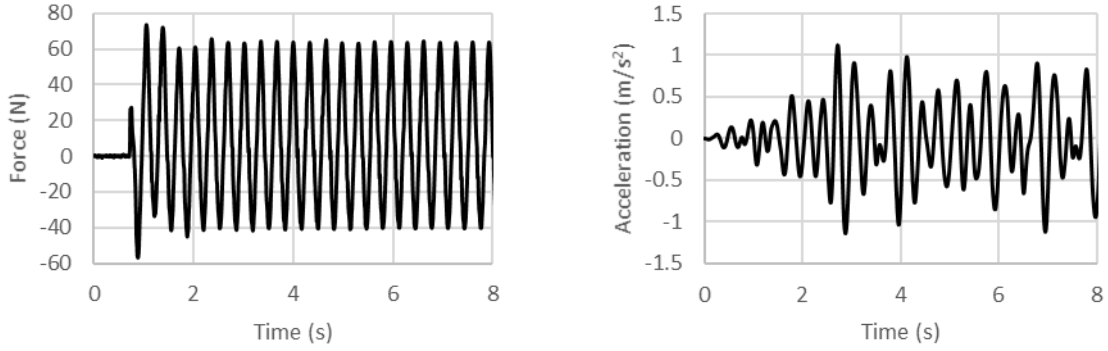

(a) *(b)*

Figure 2.16: Experimental (a) force and (b) acceleration histories at 3 Hz under displacement control.

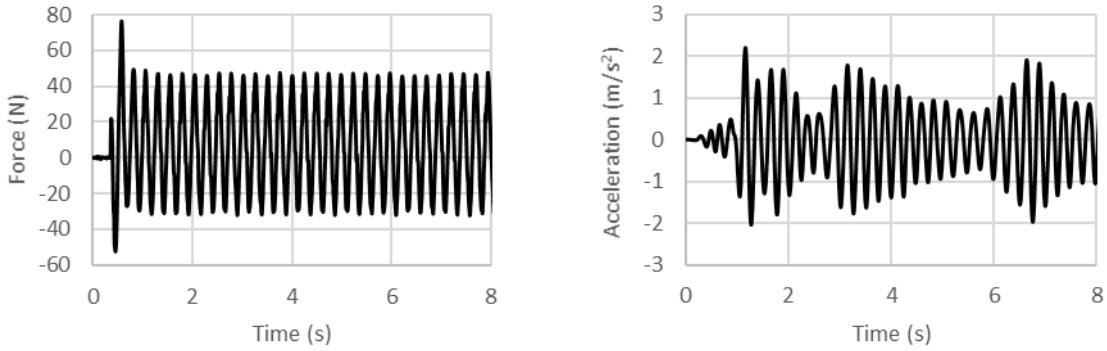

(a) *(b)*

Figure 2.17: Experimental (a) force and (b) acceleration histories at 4 Hz under displacement control.

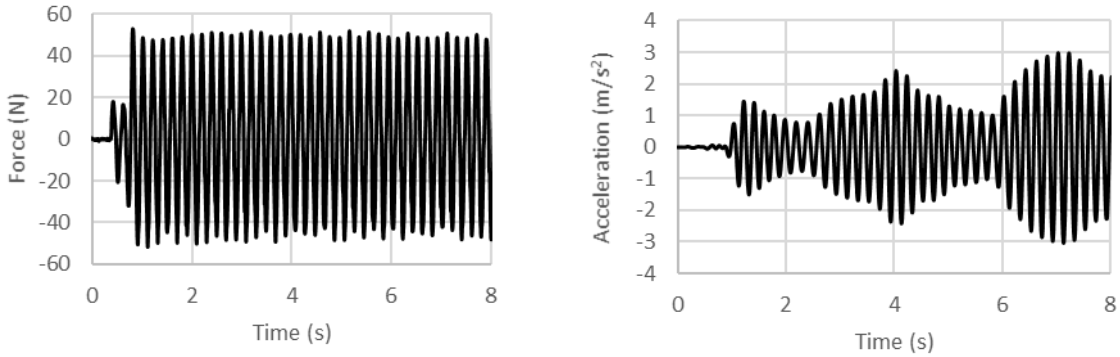

(a) *(b)*

Figure 2.18: Experimental (a) force and (b) acceleration histories at 5 Hz under displacement control.

For each frequency of excitation, three different trials were performed. The overall percentage error for the measured specific inertance between the trials was under 12%. Due to the presence of a pre-load in the load cell even at zero displacement condition an offset exists between the positive and the negative peaks in the load history. For the calculation of specific inertance the average of the peaks in the load history is used. The specific inertance versus the excitation frequency for the DCSE case are summarized in the Figure 2.19. For each frequency the data points represent the average value of the specific inertance with the error bars indicating the maximum and minimum values from the three trials. The measure specific inertance follows an exponential

trend with the excitation frequency. The fit for the specific inertance for the DCSE case is given by:

$$\left(\frac{J}{M_{st}}\right)_{DSCE} = 212.3\, e^{-0.53f} \tag{2.17}$$

Where f is the frequency of excitation. In the low frequency regime accelerations would be small and the displacement would be large hence due to the movement of the rack inertance can be realized, but in the high frequency regime due to high accelerations, displacements tend to diminish and there would be no visible movement in the rack to realize inertance, hence specific inertance tending to zero at higher frequencies is explainable. In the low frequency limit when the curve is extrapolated the fit yields a limiting value of 212.3 for the quasi-static case, which is much higher than the predicted theoretical value which is 90. It is explainable because experimental fit includes all the structural effects which include friction and misalignment, which gives an exaggerated value for the specific inertance in the low-frequency regime.

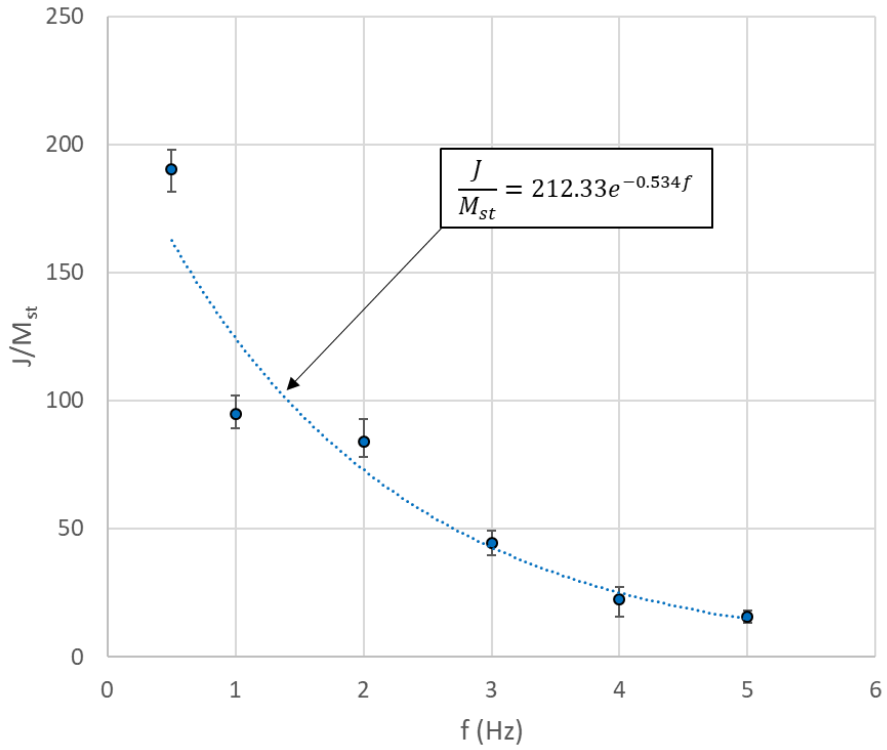

Figure 2.19: Variation of J/M_{st} with excitation frequency from displacement controlled tests.

The trend line proves an overall estimate of the specific inertance behavior with the excitation frequency, deviations such as for the 1 Hz case could be attributed to the internal dynamics arising from the assemblage of the components.

2.6.2 Acceleration Controlled Sinusoidal Excitations

In this section, the inerter is tested at acceleration controlled sinusoidal excitations at different frequencies under 5 Hz. Load and acceleration histories for frequencies 3 Hz, 4 Hz and 5 Hz are shown in the Figures 2.13 - 2.18. In all the cases the load and acceleration histories are time synchronous, and the history for the first 8 s from start-up is shown. The accelerations shown in the following figures deviates from the inputted 3.5 m/s^2, because the shaker operates without a feedback control. For each frequency, the post start-up transient data is used to extract the average peak load and average peak acceleration in order to compute the specific inertance, J/M_{st} as per Equation 2.16.

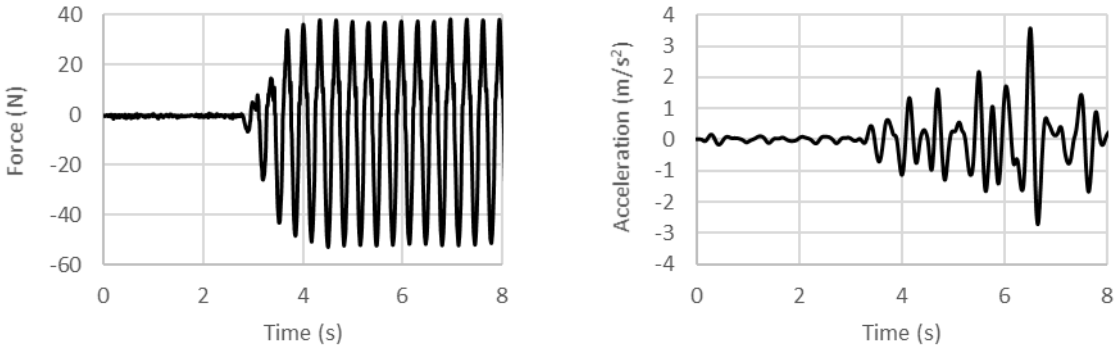

(a) *(b)*

Figure 2.20: Experimental (a) force and (b) acceleration histories at 3 Hz under acceleration control.

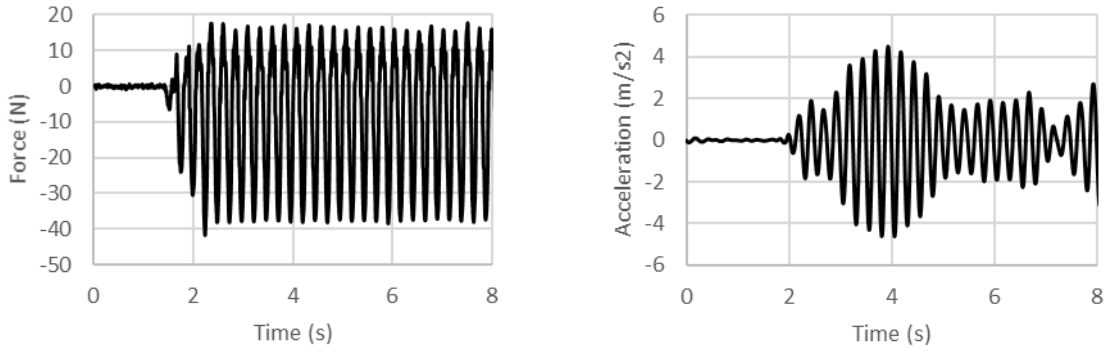

(a) *(b)*

Figure 2.21: Experimental (a) force and (b) acceleration histories at 4 Hz under acceleration control.

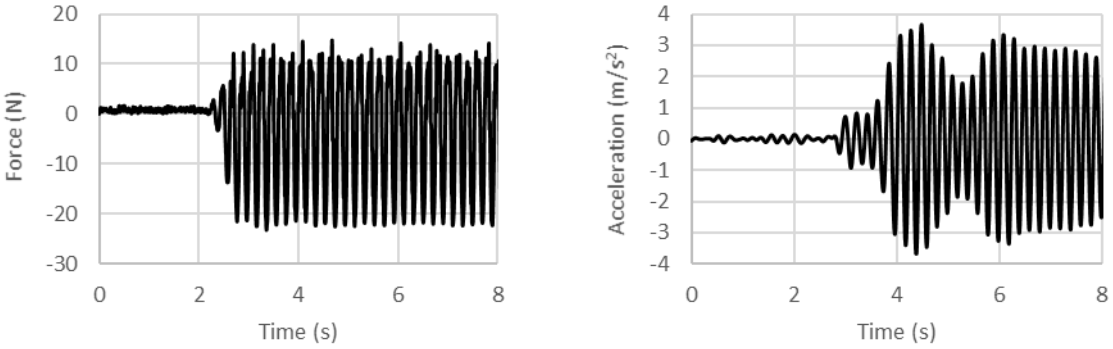

(a) *(b)*

Figure 2.22: Experimental (a) force and (b) acceleration histories at 5 Hz under acceleration control.

Figure 2.23 summarizes the specific inertance versus the excitation frequency for the ACSE case. It follows a negative exponential trend with the excitation frequency which is governed by the following equation:

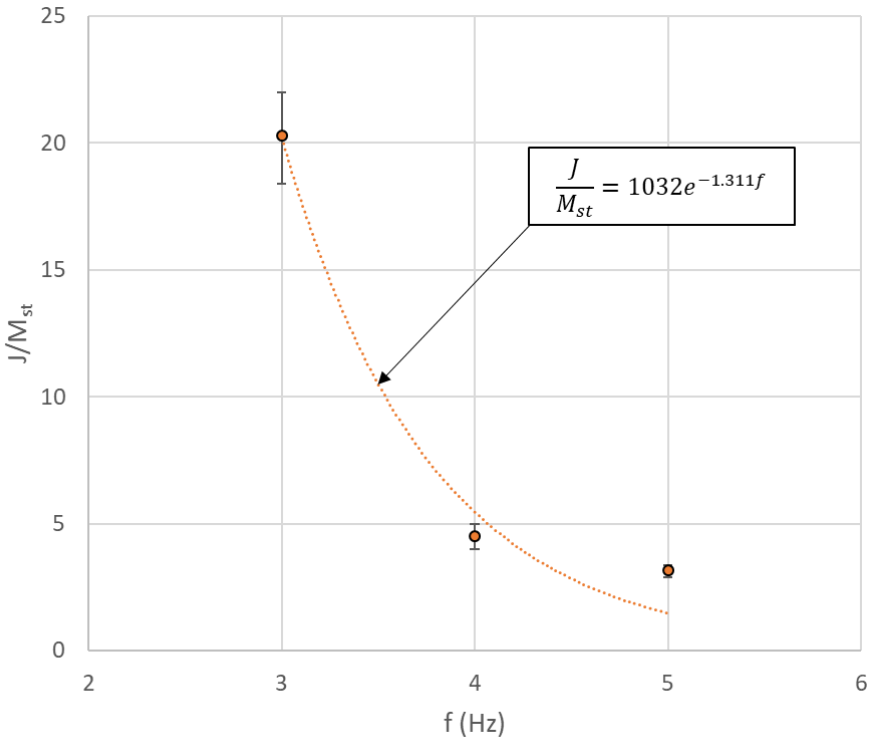

Figure 2.23: Variation of J/M_{st} with excitation frequency from acceleration controlled tests.

$$\left(\frac{J}{M_{st}}\right)_{ASCE} = 1032\, e^{-1.31f} \tag{2.18}$$

Figure 2.23 shows the variation of experimental inertance to static mass (J/M_{st}) of the inerter with frequency, it has both experimental data and the curve fitted with that data. The orange points are the average values of the specific inertance at the corresponding frequency with error bars showing the minimum and maximum values. The orange dotted line is the trend line which follows the negative exponential trend as given by Equation 2.18. Similar to the ACSE case in the high frequency regime the curve decays to zero due to high accelerations and low displacements of the rack, where in the low frequency regime when the curve is extrapolated, which is the quasi-static case it has a very high specific inertance of 1032, which is definitely high compared to the theoretical and the DCSE case. This is because ACSE and DCSE have different exciting conditions

and the displacement of the rack in DCSE is quiet less when compared to the displacements in ACSE (2-3 mm) and the system operates in a different regime as far as the mechanisms for internal resistance are concerned.

Therefore, including the effects of internal stiffness and internal damping of the test article in the theoretical model is expected to improve the predictions.

2.6.3 Estimation of Internal Stiffness and Damping

The fabricated test article is expected to have internal stiffness and damping and has a significant effect on the performance of the test article. Therefore, a lumped element model is considered for the estimation of the internal stiffness and damping.

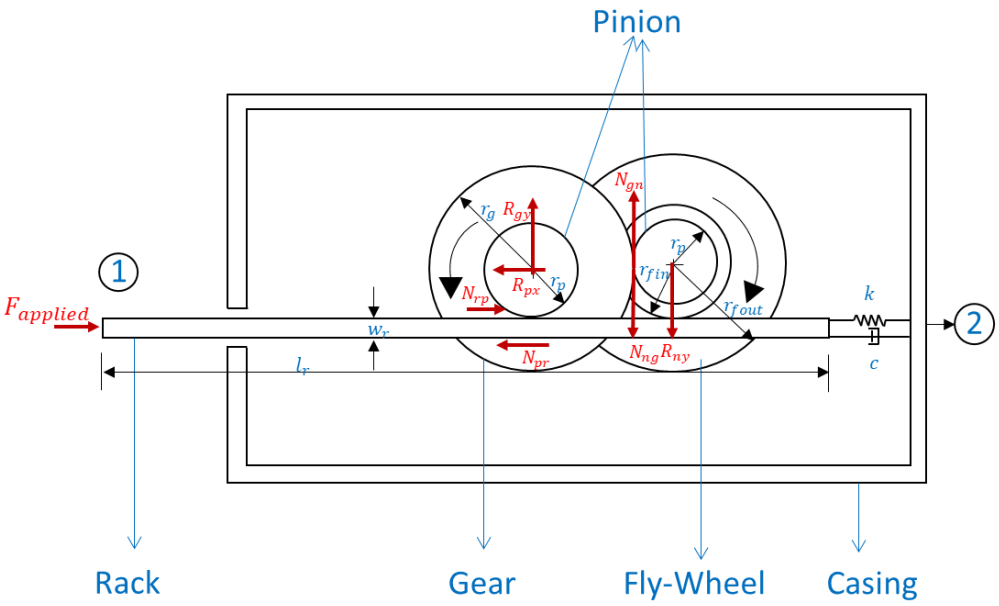

Figure 2.24: Line diagram of rack-and-pinion inerter with lumped elements representing the internal stiffness and damping

A spring and damper are connected in parallel with the rack as shown in the Figure 2.24, these act as the internal stiffness and damping of the test article. A phase matching procedure was employed to estimate the parameters.

Using the same procedure for the original rack-and-pinion inerter model, the equation of motion for this model can be derived as:

$$F_{applied} = \left[\frac{\left(\frac{m_n r_n^2}{2} + m_f k^2\right) r_g^2}{r_p^2 r_n^2} + \frac{\left(m_p r_p^2 + m_g r_g^2\right)}{2 r_p^2} + m_r\right] \ddot{u_r} + c\dot{u_r} + k u_r \tag{2.19}$$

Where u_r, $\dot{u_r}$ and $\ddot{u_r}$ are the displacement, velocity, and acceleration of the rack, respectively. Since a harmonic forcing, $F_{applied} = F_0 sin(\omega t)$ is assumed, the displacement response of the rack can be expressed as:

$$u_r = U_r sin(\omega t + \phi) \tag{2.20}$$

Where U_r is the displacement amplitude of the rack, and ϕ is the phase angle of the rack's displacement response relative to the applied harmonic force. Substituting the harmonic input and the response into Equation 2.19 one can directly obtain:

$$F_0 \sin(\omega t) = J(-\omega^2 U_r) \sin(\omega t + \phi) + c(\omega U_r) \cos(\omega t + \phi) + k U_r sin(\omega t + \phi) \tag{2.21}$$

Simplifying and comparing the coefficients of $\sin(\omega t)$ and $\cos(\omega t)$, the following two equations can be extracted.

$$F_0 + (J\omega^2 U_r - k U_r) \cos(\phi) + c U_r \omega \sin(\phi) = 0 \tag{2.22}$$

$$(k U_r - J\omega^2 U_r) \sin(\phi) + c U_r \omega \cos(\phi) = 0 \tag{2.23}$$

Using Equations 2.22 and 2.23, one can solve for the internal stiffness, k, and the internal damping coefficient, c, in terms of the phase angle, ϕ, and the inertance, J, to obtain:

$$k = \frac{F_0}{U_r} \cos(\phi) + J\omega^2 \tag{2.24}$$

$$c = \frac{-F_0}{U_r \omega} \sin(\phi) \tag{2.25}$$

In Equations 2.24 and 2.25, F_0, J, U_r, ω, and ϕ are experimental input or measured parameters. The phase angle is obtained from an averaging procedure based on the time synchronous load and acceleration histories recorded from experiments. The time lag is calculated

at multiple points and the corresponding phase angle for the respective frequencies are interpolated to obtain the evenly spaced phase angle data. Then the phase angle data is used to calculate the maximum, minimum and average phase angle. This method is repeated for all the frequencies to obtain the phase information. Then these experimentally determined phase values are substituted in order to obtain the internal stiffness and damping at all the frequencies for DCSE and ACSE cases. Then a plot is made between the frequency of excitation and the internal stiffness and parameters which is shown in the Figure 2.25. For each data point the maximum, minimum and average values are plotted using the corresponding phase values at that frequency. It is noted that the stiffness depends on the inertance, J in addition to phase angle,ϕ and displacement,U_r but the damping coefficient does not. This additional dependence on a derived experimental parameter results in higher magnitudes for the error in the estimates for internal stiffness. The values for the ACSE are comparatively smaller than those for DCSE, but they are comparable. In the DCSE case, the excitation displacements are relatively higher when compared to that of DCSE, which indicates the rate-dependence of the internal stiffness mechanism. Further, for the DCSE case, both stiffness and damping values are observed to tend towards a limiting value with an increase in the frequency of excitation. This behavior could be correlated with a transition in the rate-dependence of the internal stiffness mechanism when the frequency of excitation increases.

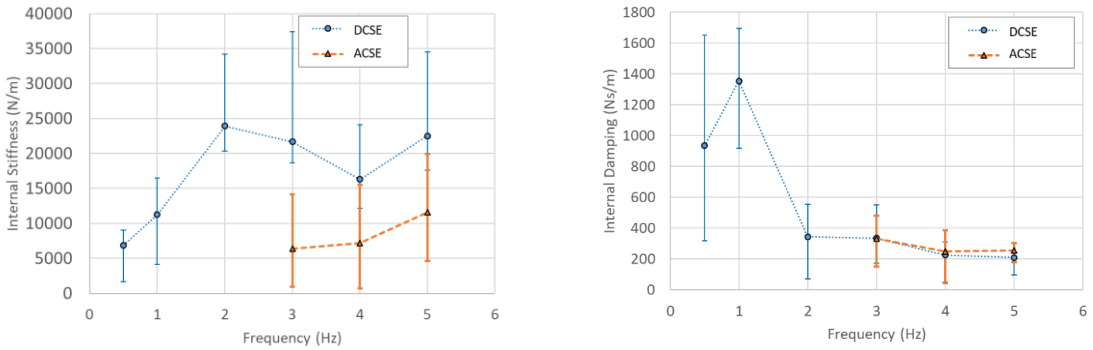

Figure 2.25: Estimated internal (a) stiffness and (b) damping versus excitation frequency.

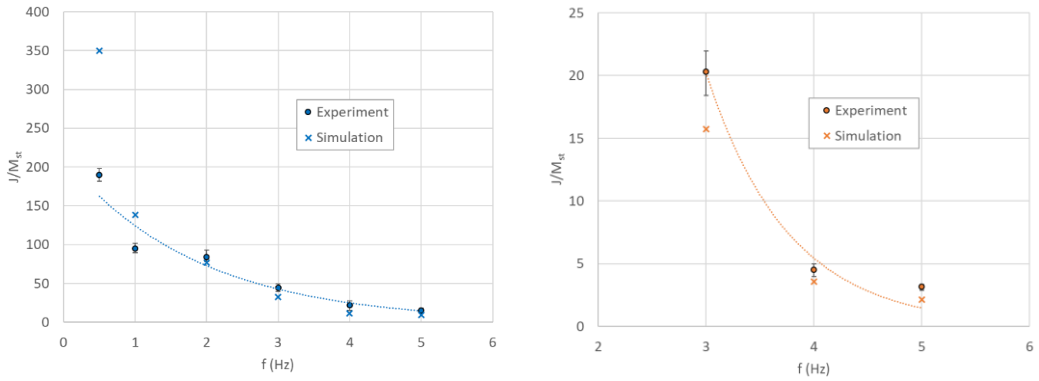

(a) *(b)*

Figure 2.26: Comparison of experimental and simulated specific inertance for (a) Displacement-Controlled Sinusoidal Excitation (DCSE) and (b) Acceleration-Controlled Sinusoidal Excitation (ACSE).

To examine the specific inertance predicted by the theoretical model based on phase estimation a discrete element model was setup using ABAQUS finite element software. The average internal stiffness and damping values are used in the model which are extracted by phase matching procedure. The two cases DCSE and ACSE are simulated using this model. In DCSE a prescribed harmonic excitation displacement boundary condition was inputted and similarly acceleration for ACSE case. Figure 2.26 is the comparison of experimental specific inertance and simulated specific inertance as predicted by the model. The simulated specific inertance is found to have very close agreement with experiments in the high frequency regime, this is due to the high scattering of the phase values in the low frequency regime. But the phase matching procedures provides a simple process to estimate the theoretical model to include the internal structural effects present in the fabricated prototypes, which would have a significant influence on the inertant performance.

The extraction of phase angle using the time synchronous load and acceleration histories reveals some interesting trends that indicated the test article nonlinear response under low-rate excitations. Using the experimentally determined phase angle data, the phase histories are used to

observe the spectrum for all the frequencies of excitation. The phase spectral data is presented in the Figures 2.27 and 2.28. Due to the test articles nonlinear response, the phase difference between the load and acceleration varies with time, even after the post-transient state seems to have been achieved. But the phase spectra shows the existence of ultra-low frequency components (< 1 Hz), do in general dominate excitation frequencies indicating the contributions from meandering effects within the structural assembly. The phase variation is also affected by the excitation frequency for DCSE case, in which the displacement amplitudes are significantly higher that the ACSE case. For this case a visible peak is observed in the frequency spectrum corresponding to the excitation frequency, indicating its direct contribution to the phase with time. In the ACSE case in which the displacements are relatively smaller, in the influence of the excitation frequency on the spectrum is not seen.

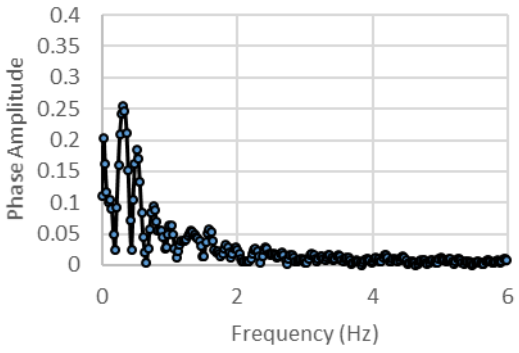

(a)

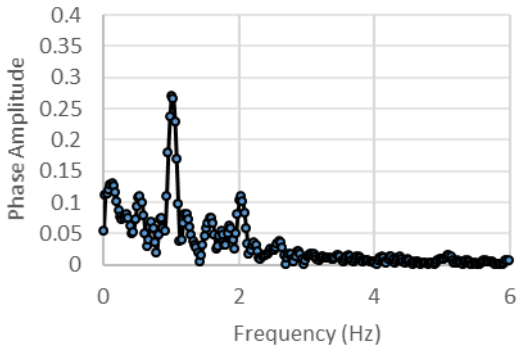

(b)

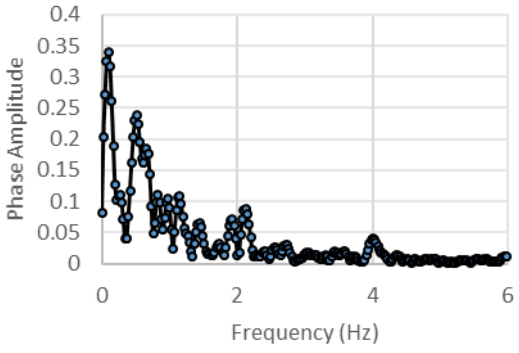

(c)

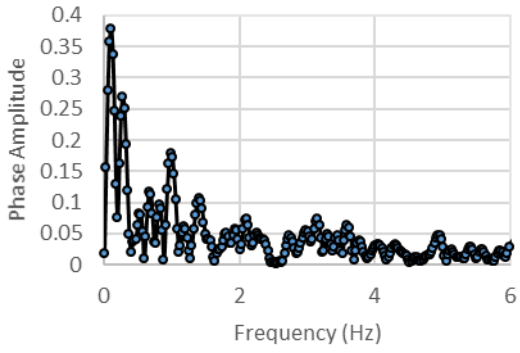

(d)

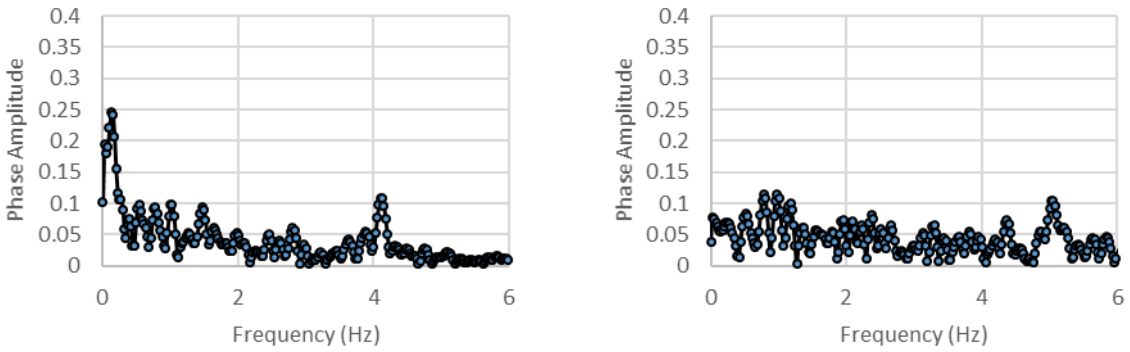

(e) (f)

Figure 2.27: Phase angle spectra for (a) 0.5 Hz, (b) 1 Hz, (c) 2 Hz, (d) 3 Hz, (e) 4 Hz, and (f) 5 Hz for displacement control

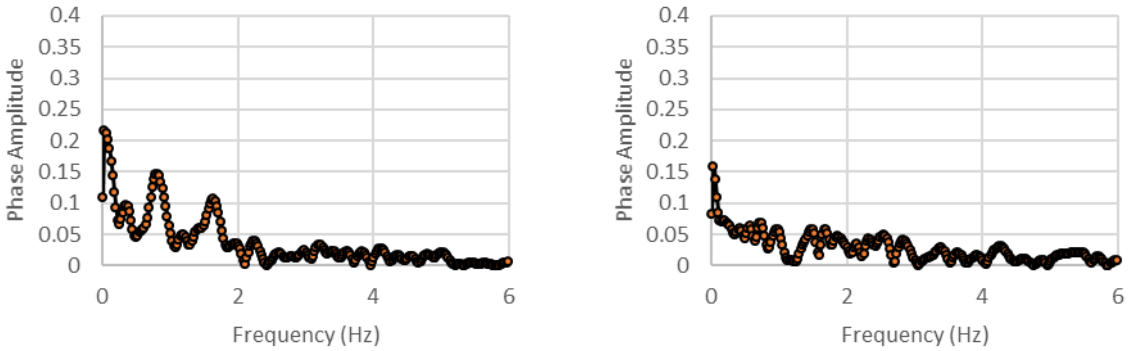

(a) (b)

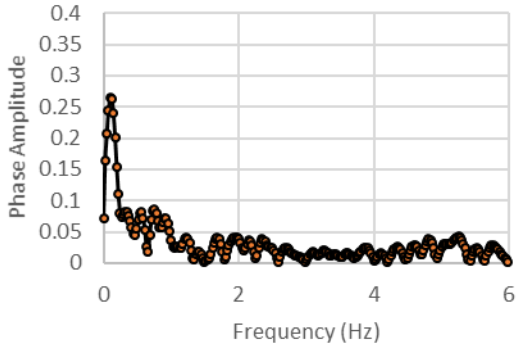

(c)

Figure 2.28: Phase angle spectra for (a) 3 Hz, (b) 4 Hz, and (c) 5 Hz for acceleration control

2.7 Summary

The main aim of this section is to study about inertance and its rate dependency. The objective was achieved by designing a rack-and-pinion inerter and deriving its force equation. A simple 2D line diagram of rack-and-pinion inerter was considered and equations of motion of all components of the inerter were derived, based on the equations of motion the final equation of motion of the inerter is derived. Parametric curves were drawn before manufacturing the test article so as to achieve the required specific inertance of the structural scale model. Based on the parametric curves and the available commercial off the components and with the help of some 3D printed structures rack-and-pinion inerter was manufactured. To study the rate dependence an experiment setup was built. The specific inertance 'J/M_{st}' followed a negative exponential trend with the rate of excitation in both the test cases. This indicates that the structural scale inerter is meant only to be used at low frequency excitations. The exaggerated specific inertance in the experiments is high compared to the theoretical predicted value, to explain this a lumped element model was considered to estimate the internal stiffness and damping of the system using a phase matching procedure. Next, a discrete element model was setup in ABAQUS to model the theoretical inerter and the experimentally estimated internal stiffness and damping were also included. The model predicts very close values of the specific inertance in the high frequency regime due to less error compared to the low-frequency regime. To investigate a potential kinematically simpler structure which can have inerter like behavior and can be used at high frequencies is investigated in the succeeding section.

CHAPTER III

CHARACTERIZATION OF INERTANCE IN A KINEMATICALLY SIMPLER STRUCTURE

3.1 Introduction & Motivation

The experimental study carried out in the previous chapter deals with a structural scale implementation of the inerter tested at low frequencies and it is observed that at high frequencies the inertance to static mass ratio J/M_{st} decays to zero exponentially as there will be no appreciable movement in the rack to result in dynamic mass amplification effect at high frequencies as displacements are quite small. This indicates that the inerter is restricted to low frequencies at the structural scale unless extreme gearing ratios are employed. Moreover the rotary components necessary to realize mechanical manifestation of the inerter are not easily amenable to miniaturization which is desirable for MEMS applications. For microscale applications it is therefore desirable to have kinematically simpler structures that could potentially deliver an inertant response. This chapter deals with the investigation of a potential kinematically simpler structure for inerter that is based on a modification of the von Mises truss.

Now a question arises, about what type of model or structure is to be used exact this kinematic simplification so that the inerter can be used in high frequency applications. At microscale for instance, manufacturing of the rack-and-pinion inerter or the ball-screw inerter is very difficult and involves high manufacturing cost. Even if an inerter is manufactured it could be very difficult to ensure consistency due to the complicated structure.

Hence an inerter like structure that is kinematically simpler is desirable for such applications, so that it can be used in miniature scale and in high frequency applications.

For the potential kinematically simpler structure a modified form of the von Mises truss is considered as basis for the new design. The von Mises truss is a bi-stable truss than exhibits snap-through behavior. A bi-stable truss is the one which has two stable positions and it can snap through from one stable position to another after reaching a threshold point where the truss elements will encourage buckling.

It has two stiffness regimes one where force is directly proportional to the displacement and another which is the negative stiffness region, where even though less force or no force is applied more displacement is caused, it is a region where force and displacement are in opposite direction. In other words the system can be self-driven due to internal forces in this regime. When the truss is acted upon by a force till a certain point the truss moves in proportion with respect to the force, but after the threshold point the truss elements cannot take the compression and undergoes buckling rapidly during which it snaps through to its second stable position with some transience.

Using this snap through effect a novel truss first of its kind is designed which has an additional arm and mass. This arm swings about the pinned position, hence this arm is termed as swing arm and the mass attached to it is termed as the swing arm mass (SAM). The inertance effect in the rack-and-pinion inerter is due to the gearing ratio, flywheel mass and radius of gyration of the flywheel. This swing arm length (SAL) will act as the radius of gyration of the flywheel and the mass attached to the swing arm will act as the mass of the flywheel. So when the structure undergoes snap-through motion, the swing arm is thrown away to another position and might capture a part of the flywheel movement, hence this snapping effect and the SAM throw away might contribute to the dynamic mass amplification.

The structure is simple in construction and easy to manufacture in miniature and micro scale as well, hence this model can be extended to investigate its application in MEMS (Micro

Electro Mechanical Systems) domain. The current study focusses on miniature scale model only, hence this serves as a basis to investigate further in the field of MEMS in the future.

3.2 Analytical Model

A von Mises truss which is a bi-stable truss is considered as the basis for the design as shown in the Figure 3.1, it has a vertex mass with two truss elements, it is connected to the ground with the help of a linear viscous damper, which has a roller support in the horizontal direction. This structure exhibits two types of stiffness regimes while moving to its second stable position.

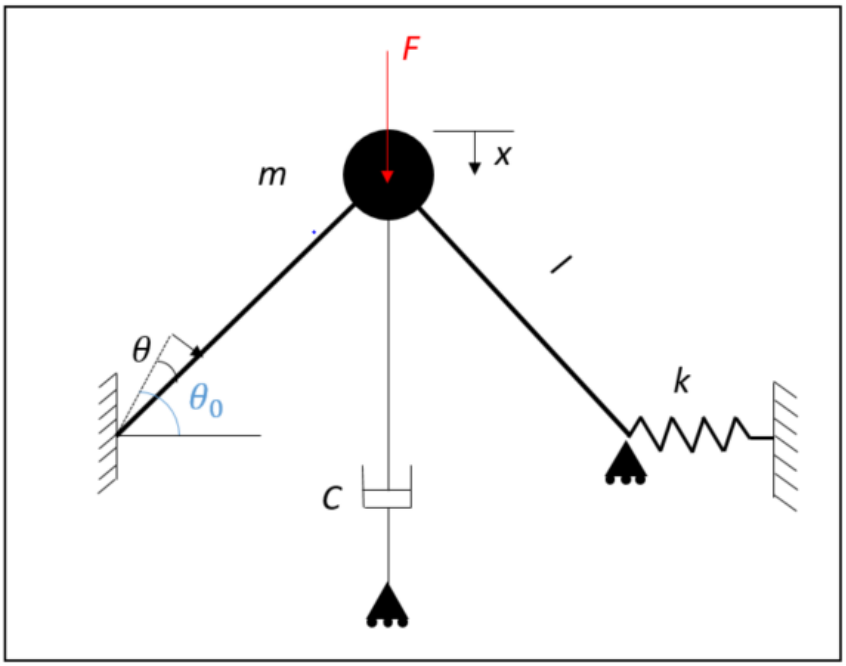

Figure 3.1: von Mises truss [43]

As shown in the Figure 3.1, region 'A' is the positive stiffness region where the stress is directly proportional to strain. Region 'B' is the negative stiffness or zero stiffness region where the structure just snaps through to another stable position with some transience.

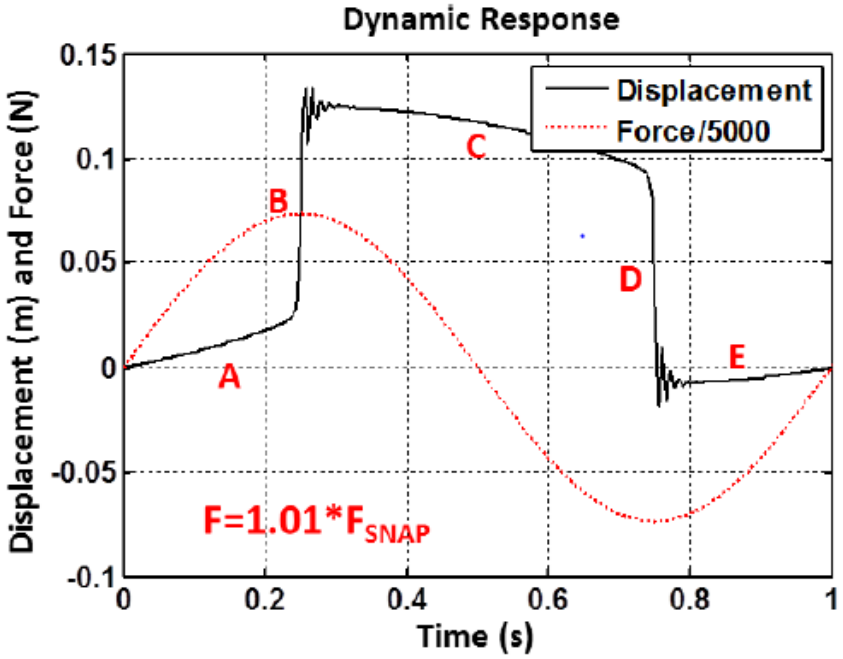

Figure 3.2: Dynamic response of a von Mises truss [43]

Lumped mass model is considered for the analytical model as shown in the Figure 3.2, which has two masses, three truss elements, two springs and a damper in the vertical direction. It is evident that the vertex mass can move only in the vertical direction, and the SAM moves in a circular motion about the SAL radius. The two ends of the bi-stable arch have pinned ends as bi-stable arch with pinned ends has more bi-stable characteristic as discussed in [43]. A vertical force 'F' is applied on the vertex mass, it is connected to the ground with a linear viscous damper with a fixed boundary condition.

Figure 3.3, is a von Mises truss with additional arm and mass. The links are pin-jointed truss elements and are assumed to be rigid. The links are assumed to be massless and the entire mass is lumped into two concentrated masses which are the tip mass and the SAM. The tip mass is forced to move in the vertical direction only as the two ends of the pinned joints are fixed. The two pinned ends of the structure and the dashpot's fixed end combined could act as the second end of the inerter, which is the fixed end. The vertex of the truss is connected to the ground by a linear

viscous damper. The initial angle made by the truss elements is denoted by θ_0, positive counterclockwise and at any time the angle made with the initial position is θ positive clockwise.

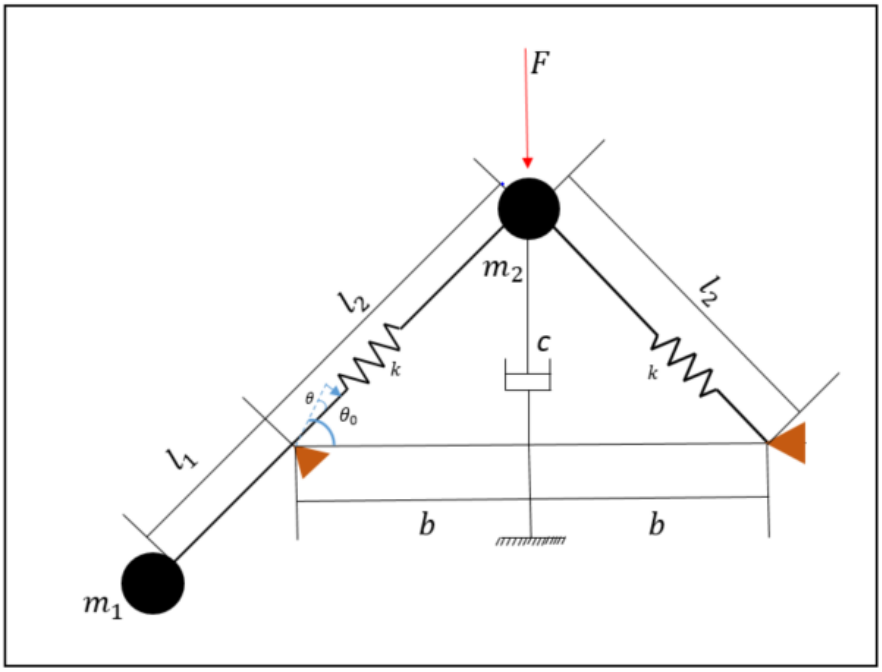

Figure 3.3: Analytical model of the potential kinematically simpler structure

To study the dynamics of this system it is important to know the equation of motion of the system, which defines the position of second mass m_1 and m_2 at any time. The nonlinear equation of motion is derived by using the Lagrange's method based on Hamilton's principle. In this method first the kinetic (T) and elastic potential (V) energies of the system are derived and the Lagrangian (L) is defined as follows.

$$L = T - V \tag{3.1}$$

The Euler-Lagrange equation is defined as

$$\frac{\partial}{\partial t}\left(\frac{\partial L}{\partial \dot{q}}\right) - \frac{\partial L}{\partial q} = Q \tag{3.2}$$

The kinetic energy of the system stems from the two masses, one at the vertex and another which is the swing arm mass.

$$T = \frac{1}{2} m_1 l_1^2 \dot{\theta}^2 + \frac{1}{2} m_2 b^2 \, sec(\theta_0 - \theta)^4 \, \dot{\theta}^2 \tag{3.3}$$

The potential energy of the system due to the deflection of the two springs.

$$2 * \frac{1}{2} k(\delta x)^2 \tag{3.4}$$

Deflection of the spring is given by the equation

$$\delta x = b\left(\frac{1}{cos(\theta_{01})} - \frac{1}{cos(\theta_{01} - \theta_1)}\right) \tag{3.5}$$

Hence potential energy contributed by the two springs is

$$kb^2\left(\frac{1}{cos(\theta_{01})} - \frac{1}{cos(\theta_{01} - \theta_1)}\right)^2 \tag{3.6}$$

The potential energy of the system due to the damper is

$$-\int cv^2 dt \; or - \int cv \, dy \tag{3.7}$$

The total potential energy of the system is as follows

$$V = kb^2\left(\frac{1}{cos(\theta_{01})} - \frac{1}{cos(\theta_{01} - \theta_1)}\right)^2 + -\int cv^2 dt \; or - \int cv \, dy \tag{3.8}$$

The velocity can be written as

$$v = b \, sec(\theta_0 - \theta)^2 \dot{\theta} \; or \; dy = b \, sec(\theta_0 - \theta)^2 \, d\theta \tag{3.9}$$

Now, substituting the Equations 3.3 and 3.8 into the Equation 3.1 we have the Lagrangian, *L* as follows

$$L = \frac{1}{2} m_1 l_1^2 \dot{\theta}^2 + \frac{1}{2} m_2 b^2 \, sec(\theta_0 - \theta)^4 \, \dot{\theta}^2 - kb^2(sec(\theta_0) - sec(\theta_0 - \theta))^2 + [\int cv^2 dt \; or \int cv \, dy \,] \tag{3.10}$$

Now, substituting Equation 3.10 into Equation 3.2 and simplifying we finally end up with

$$\ddot{\theta}[m_1 l_1^2 + m_2 b^2\, sec(\theta_0 - \theta)^4] - \dot{\theta}^2[2m_2 b^2 sin(\theta_0 - \theta)\, sec(\theta_0 - \theta)^5] + 2kb^2\, sin(\theta_0 - \theta)\, sec(\theta_0 - \theta)^2\, [sec(\theta_0) - sec(\theta_0 - \theta)] + cb^2\, sec(\theta_0 - \theta)^4\, \dot{\theta} = Fb\, sec(\theta_0 - \theta)^2 \tag{3.11}$$

Equation 3.11 is the equation of motion of the potential kinematically simpler structure, it is a nonlinear ordinary differential equation in θ of second order.

3.3 Numerical Parametric Study

The parametric dependencies for the specific inertance of the potential kinematically simpler structure are explored using the simulations by numerically integrating the ODE (3.11) in MATLAB R2016b using ode45 based on an explicit Runge-Kutta formula. For all the dynamic solutions the system was initially at rest in the non-deformed configuration.

$$\theta\,(t = 0) = 0$$
$$\dot{\theta}\,(t = 0) = 0 \tag{3.12}$$

Table 3.1: Base parametric setting of the potential kinematically simpler structure

Parameter	Value
Tip mass (m_1)	0.001 kg
Swing arm mass (m_2)	0.001 kg
Link length (l_1)	0.005 m
Swing arm length (l_2)	0.005 m
Spring stiffness (k)	600 N/m
Damping Constant (c)	0.1 Ns/m

The base parameters used for the simulation are shown in the table 3.1, which are based on the aim that the model is small enough such that it can be simulated at high frequencies.

The generation of the variation of the specific inertance with the key parameter establishes a feasible design space and aids the parameter selection so as to optimize the specific inertance of the system. In the potential kinematically simpler structure the key parameters which could cause the dynamic mass amplification affect are carefully identified and a simulation matrix is developed as shown in the Table 3.2.

Two cases are studied here (i) Harmonic Displacement Input (HDI) and (ii) Harmonic Force Input (HFI) on the tip or the vertex mass m_1. In the HDI case the displacement of the tip mass is controlled and the amplitude is given such that the tip mass moves to the second stable position. In the HFI case the tip mass is given a harmonic force which causes the tip to snap-through to second stable position, the force which causes the snap through is called as snap through force and is calculated from the hysteresis loop of the HDI case.

3.4 Harmonic Displacement Input

In this case the tip mass displacement is controlled and it is excited with a sinusoidal displacement input. For the tip mass to travel to the second stable position the amplitude is set to the full stroke $Amp = 2l_2\sin(\theta_0)$ that is the amount of displacement necessary to let the tip mass travel from the initial stable position to the second stable position. As the displacement of the tip mass is controlled the force-displacement curves don't have the snap through effect.

The displacement input equation which satisfies the initial conditions, given by Equation 3.12 is as follows

$$y = btan(\theta_0) - btan(\theta_0)cos(\omega t) \qquad (3.13)$$

Where θ_0 is the initial angle made by link l_2 with horizontal, ω is the frequency of excitation. Based on the equation of motion given by the Equation 3.11 and the sinusoidal displacement input given by Equation 3.13, is solved in MATLAB.

The key parameters identified from the analytical model are the SAM (m_1), SAL (l_1), damping constant (C) and excitation frequency (f). The key parameters are varied keeping the other parameters constant to study the effect on the specific inertance.

3.4.1 Swing Arm Mass Variation

In this section the variation of SAM is studied under HDI. It is expected to act as the mass of the inerter's flywheel, it is varied from a very less value to a high value when compared to the base value, to study its dependence on the specific inertance of the structure.

Table 3.2: Swing arm mass variation cases

Dimensionless Parameter	$m_1 =$ $0.0001\ kg$	$m_1 =$ $0.001\ kg$	$m_1 =$ $0.002\ kg$	$m_1 =$ $0.01\ kg$	$m_1 =$ $0.02\ kg$
$\mu = m_1/m_2$	0.1	1	2	10	20

The simulation matrix is shown in the Table 3.2, the SAM is varied from 0.0001 kg to 0.02 kg. The base parameters used for this set of simulations are $l_1 = 0.005\ m, m_2 = 0.001\ kg,\ l_2 = 0.005\ m,\ f = 1\ Hz, C = 0.1\ Ns/m,\ k = 600\ \frac{N}{m}\ and\ \omega^*(\sqrt{\frac{k}{m_2}}) = 775\ rad/s.$

As shown in the Figure 3.4 the structure has a hysteresis loop with some energy loss due to the presence of a damper which dissipates energy over the cycle. The force and displacement are directly proportional till about 1.3 mm of displacement and the structure has positive stiffness, then the tip mass experiences a peak force which is the snap through force and then it exhibits negative/zero stiffness up to 3.8 mm and followed by a positive stiffness region.

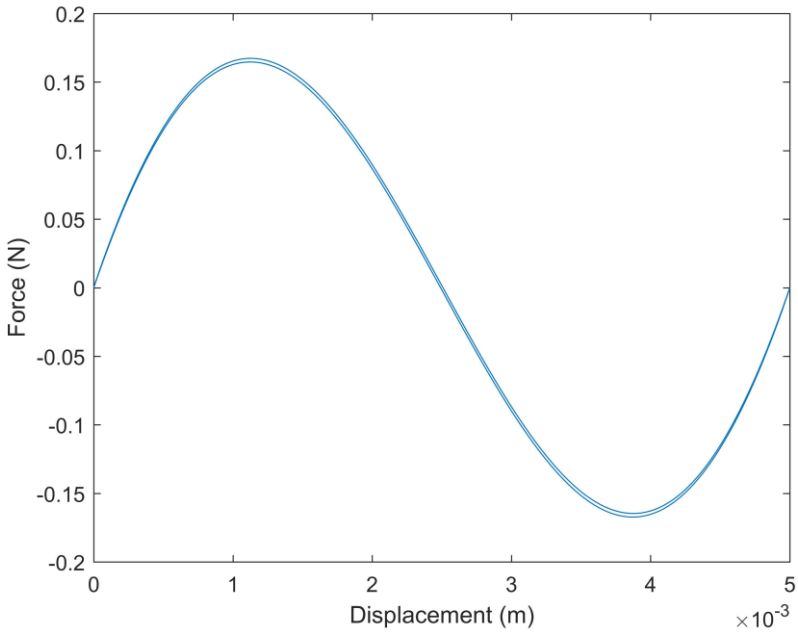

Figure 3.4: Hysteresis loop for $m_1 = 0.0001\ kg$

The remaining cases of the SAM variation show a similar hysteresis loop with increasing peak force and energy loss due to the increase in the SAM.

3.4.2 Swing Arm Length Variation

The SAL which could act as the radius of the inerter and its variation might have considerable effect on the specific inertance. In this section the effect of varying the SAL is studied under HDI. It is varied from a small value to a high value as given by the Table 3.3 to study its effect on the specific inertance.

Table 3.3: Swing arm length variation cases

Dimensionless Parameter	$l_1 =$ $0.0005\ m$	$l_1 =$ $0.001\ m$	$l_1 =$ $0.005\ m$	$l_1 =$ $0.01\ m$	$l_1 =$ $0.02\ m$
$\lambda = l_1/l_2$	0.1	0.2	1	2	4

The base parameters used for this set of simulations are $m_1 = 0.001\ kg, m_2 = 0.001\ kg,\ l_2 = 0.005\ m,\ f = 1\ Hz, C = 0.1 Ns/m,\ k = 600\ \frac{N}{m}\ and\ \omega^*(\sqrt{\frac{k}{m_2}}) = 775\ rad/s$.

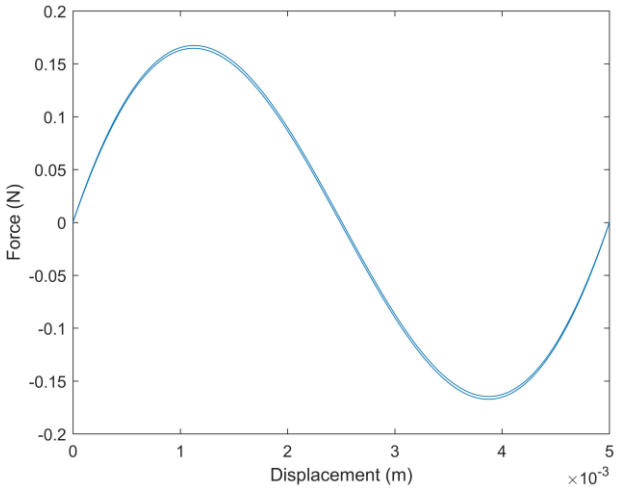

Figure 3.5: Hysteresis loop for $l_1 = 0.0005\ m$

Figure 3.5 is the hysteresis loop for $l_1 = 0.0005\ m$, it shows a similar behavior as of the SAM variation case but with very small change in the snap through force and the energy dissipation. Increasing the SAL shows an increase in the snap through force and energy loss.

3.4.3 Damping Constant Variation

This section deals with the variation of damping constant of the structure under HDI. Damping is inherent in any kind of structure and its effect on the specific inertance is necessary. The damping is varied from 0.001 Ns/m to 10 Ns/m as given by the Table 3.4

Table 3.4: Damping constant variation cases

Dimensionless Parameter	$c = 0.001$ Nsm^{-1}	$c = 0.01$ Nsm^{-1}	$c = 0.1$ Nsm^{-1}	$c = 1$ Nsm^{-1}	$c = 10$ Nsm^{-1}
$\gamma = \frac{c^2}{km_2}$	0.00000167	0.000167	0.0167	1.67	166.67

The base parameters used for this set of simulations are $m_1 = 0.001\,kg,\ l_1 = 0.005\,m, m_2 = 0.001\,kg,\ l_2 = 0.005\,m,\ f = 1\,Hz,\ k = 600\,\frac{N}{m}\ and\ \omega^*(\sqrt{\frac{k}{m_2}}) = 775\,rad/s.$

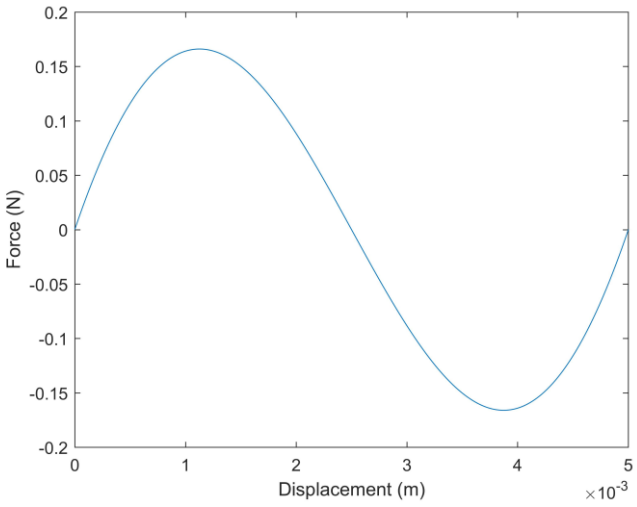

(a)

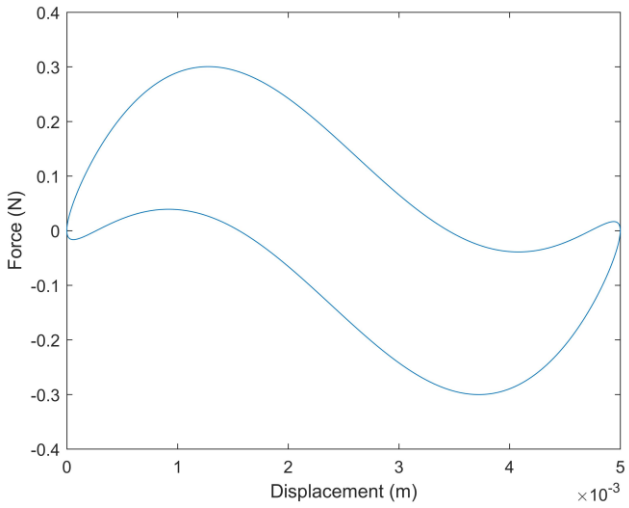

(b)

Figure 3.6: Hysteresis loop for (a) $c = 0.001\ Ns/m$ (b) $c = 10\ Ns/m$

From Figures 3.6 (a) and (b) it can be inferred that increasing the damping constant increases the energy loss of the system and it will have a considerable effect on the performance of the structure.

3.4.4 Excitation Frequency Variation

To study the rate dependent behavior of the potential kinematically simpler structure, the excitation frequency is varied as given in the Table 3.5. The frequency is varied from $0.628\ rads^{-1}$ $(0.1\ Hz)$ which is close to the quasi-static case and to $62.8\ rads^{-1}$ $(10\ Hz)$.

Table 3.5: Excitation frequency variation cases

Dimensionless Parameter	$\omega = 0.628\ rads^{-1}$	$\omega = 3.14\ rads^{-1}$	$\omega = 6.28\ rads^{-1}$	$\omega = 31.4\ rads^{-1}$	$\omega = 62.8\ rads^{-1}$
$\Omega = \omega\ /\omega^*$	0.00081	0.004	0.0081	0.04	0.081

The base parameters used for this set of simulations are $m_1 = 0.001\ kg,\ l_1 = 0.005\ m, m_2 = 0.001\ kg,\ l_2 = 0.005\ m, C = 0.1\frac{Ns}{m}$, $k = 600\ \frac{N}{m}$ $and\ \omega^*(\sqrt{\frac{k}{m_2}}) = 775\ rad/s.$

From Figures 3.7 (a) and (b) as the excitation frequency varies the energy loss increases which is due to high accelerations achieved in the structure due to increase in the cycles per second and more energy loss.

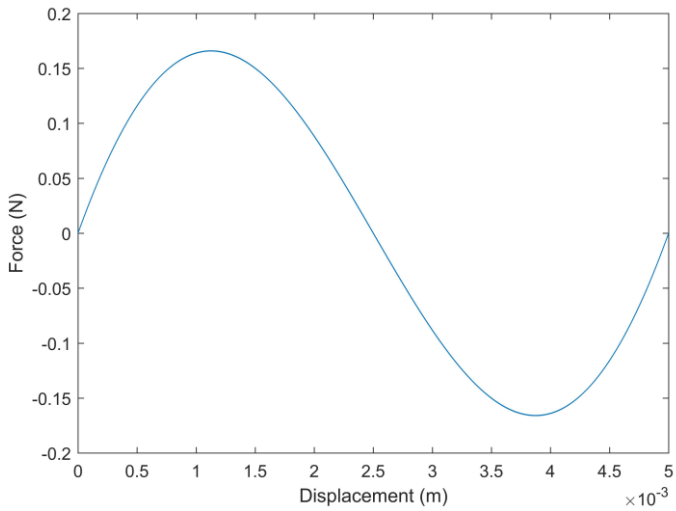

(a)

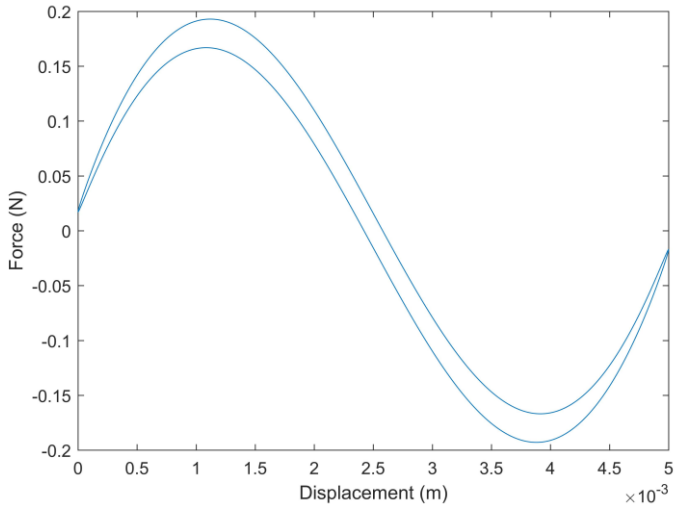

(b)

Figure 3.7: Hysteresis loop for (a) $\omega = 0.628\, rads^{-1}$*(b)* $\omega = 62.8\, rads^{-1}$

3.5 Harmonic Force Input

In this section the variations discussed in the previous sections are studied under HFI (harmonic force input), in which a harmonic force is applied at the tip mass. The equation of motion given by the Equation 3.11 is solved in MATLAB using ODE45. In this case the harmonic force is chosen based on the HDI simulations in which the peak force experienced by the tip mass is the snap through force and any force above the snap through force causes the snap through effect.

3.5.1 Swing Arm Mass Variation

As discussed in the previous section the same set of simulations are carried out for the HFI case as well, where the input force is the peak force experienced by the tip mass under HDI. As given by the Table 3.2 the SAM is varied from 0.0001 kg to 0.02 kg to study its effect on the specific inertance and the snap through effect.

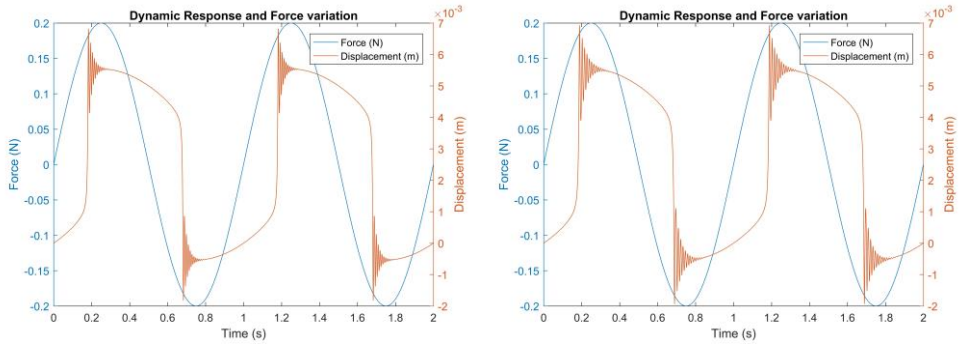

(a) *(b)*

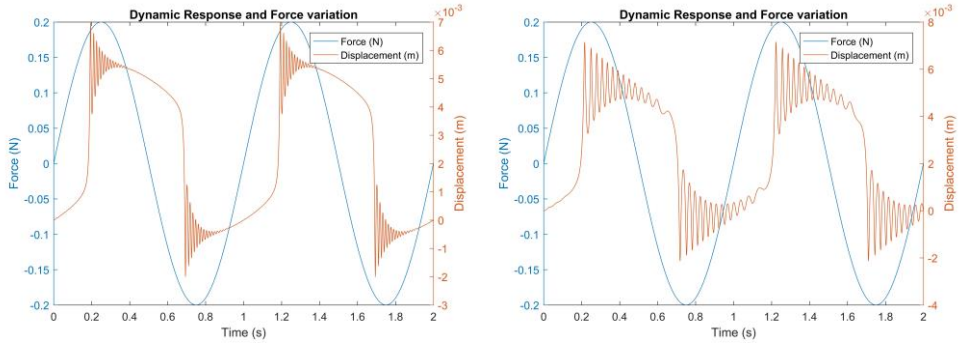

(c) *(d)*

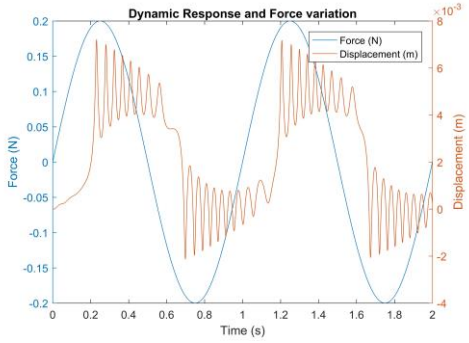

(e)

Figure 3.8: Dynamic response and force variation for (a) $m_1 = 0.0001\ kg$ *(b)* $m_1 = 0.001\ kg$ *(c)* $m_1 = 0.002\ kg$ *(d)* $m_1 = 0.01\ kg$ *(e)* $m_1 = 0.02\ kg$

Figure 3.8 (a) to (e) are the dynamic response and force variation on the tip mass with varying SAM. The positive stiffness region is seen up to 0.22 s where the force and displacement

are proportional and after that the structure exhibits zero stiffness region where even with less force more displacement is caused and the snap through effect is seen and the tip mass snaps from its first stable position to another stable position with some transience.

It is clearly evident that as the SAM increases the transience frequency of the tip mass is changing, this is explainable because when the mass increases it takes more time to stabilize due to more inertia and the frequency decreases.

3.5.2 Swing Arm length Variation

The SAL which is supposed to act as the radius of the inerter in the potential kinematically simpler structure, as given by the Table 3.3 the SAL is varied from 0.0005 m to 0.02 m under HFI to study the influence of it on the specific inertance of the structure.

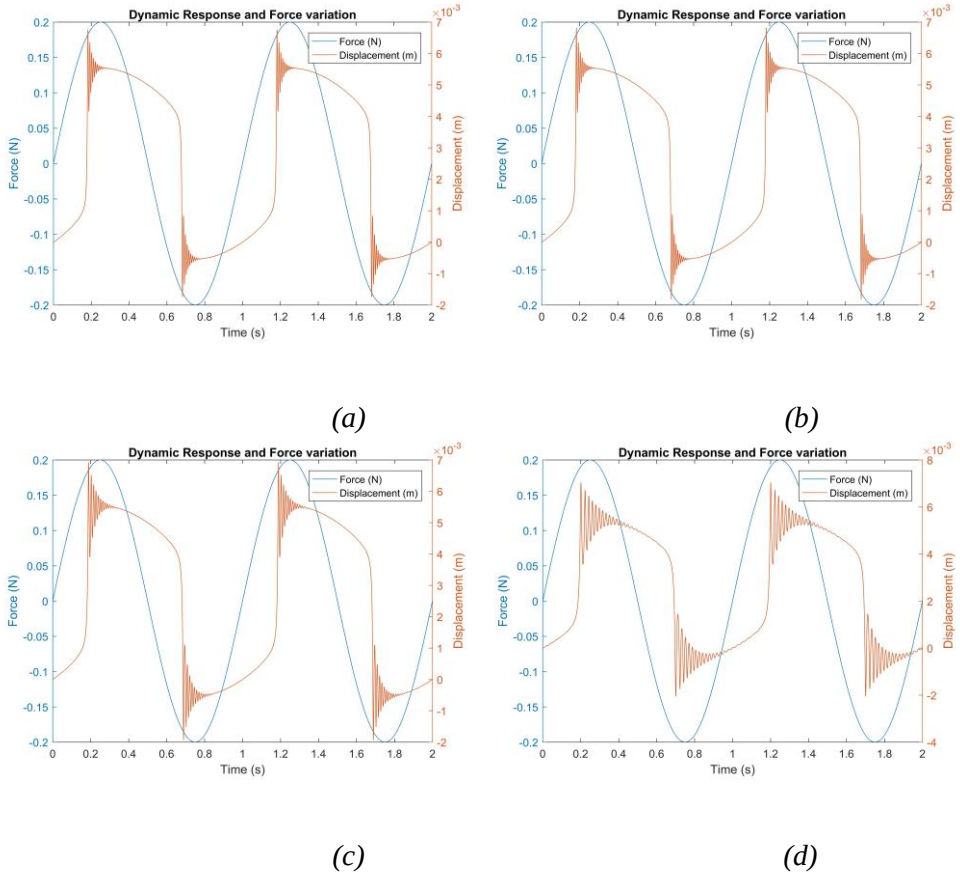

(a) *(b)*

(c) *(d)*

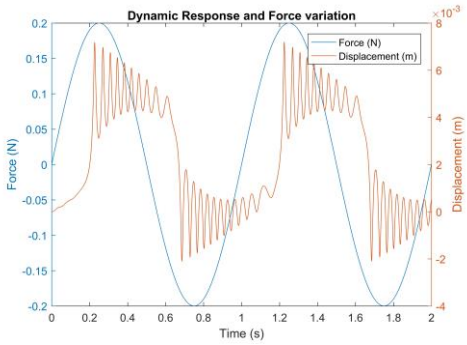

(e)

Figure 3.9: Dynamic response and force variation for (a) $l_1 = 0.0005\ m$ *(b)* $l_1 = 0.001\ m$ *(c)* $l_1 = 0.005\ m$ *(d)* $l_1 = 0.01\ m$ *(e)* $l_1 = 0.02\ m$

The snap through force is calculated using the same procedure that is employed for SAM variation. As seen in the SAM variation, similar snap through effect can be seen in the swing arm length variation as well. Increasing the SAL decreases the frequency of the transient response which is explainable due to decrease in the stiffness of the structure due to increase in the length.

3.5.3 Damping Constant Variation

Damping is inherent in any structure it may be due to material, friction or the structure. It has a significant effect on the performance of the structure under cyclic loading due to continuous loss of energy. As given by the Table 3.4 the similar set of simulations are carried for the HFI case with varying damping constant.

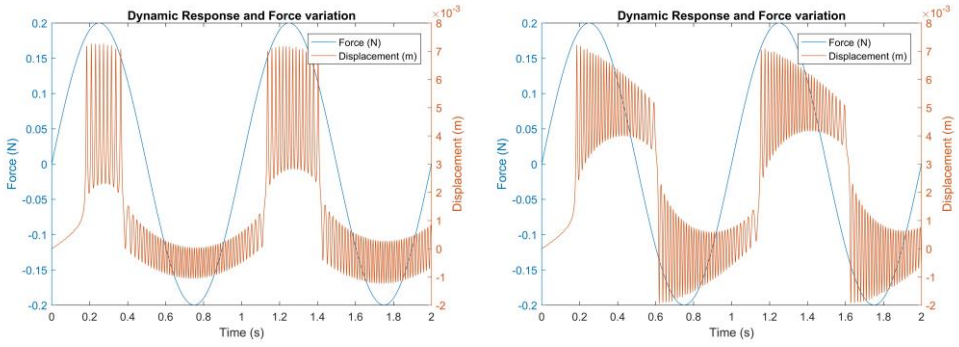

(a) *(b)*

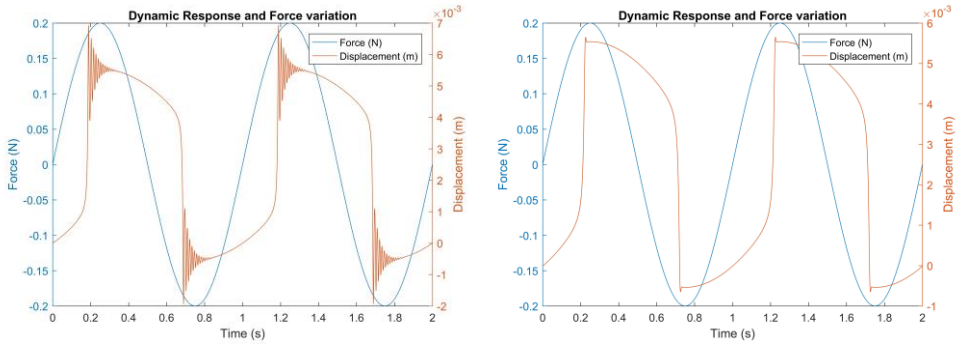

(c) *(d)*

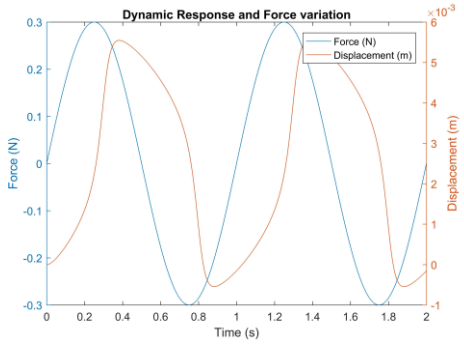

(e)

Figure 3.10: Dynamic response and force variation for (a) $C = 0.001\ Ns/m$ *(b)* $C = 0.01\ Ns/m$ *(c)* $C = 0.1\ Ns/m$ *(d)* $C = 1\ Ns/m$ *(e)* $C = 10\ Ns/m$

From Figure 3.10 (a) to (e) it can be inferred that initial transience are high for the case with less damping and gradually the transience disappear due to high damping constant, this is explainable due to high energy loss and the high resistance offered by the damper the transience vibrations are reduced drastically.

3.5.4 Excitation Frequency Variation

As given by the Table 3.5 similar set of simulations are carried out for the excitation frequency variation under HFI. The dynamic response and the force variation are given in the Figures 3.10 (a) to (e).

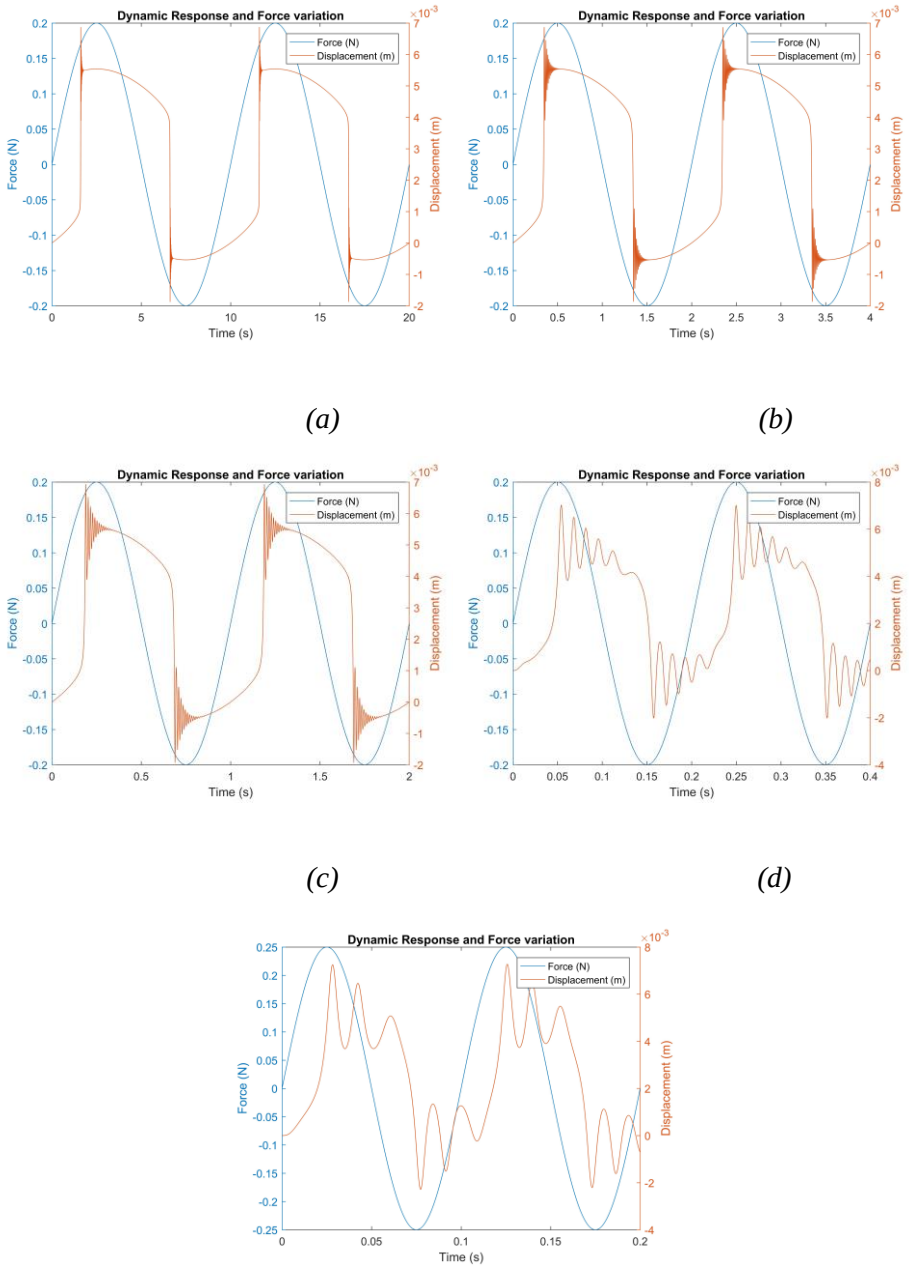

Figure 3.11: Dynamic response and force variation for (a) $\omega = 0.628\, rads^{-1}$ *(b)* $\omega = 3.14\, rads^{-1}$ *(c)* $\omega = 6.28\, rads^{-1}$ *(d)* $\omega = 31.4\, rads^{-1}$ *(e)* $\omega = 62.8\, rads^{-1}$

From Figures 3.11 (a) to (e) the gradual decrease in the transient response is observed this is because the increase in number of cycles per second decreases the time for the tip mass to stabilize and by the time it stabilizes it moves to another stable position.

3.6 Results and Discussions

The results from two test cases – Harmonic Displacement Input (HDI) and Harmonic Force Input (HFI) are presented and discussed for the key parameter variation. For each case the force and acceleration history are saved and the specific inertance is calculated using the following expression

$$\frac{J}{M_{st}} = \frac{F_{rms}}{a_{rms}\, M_{st}} \tag{3.14}$$

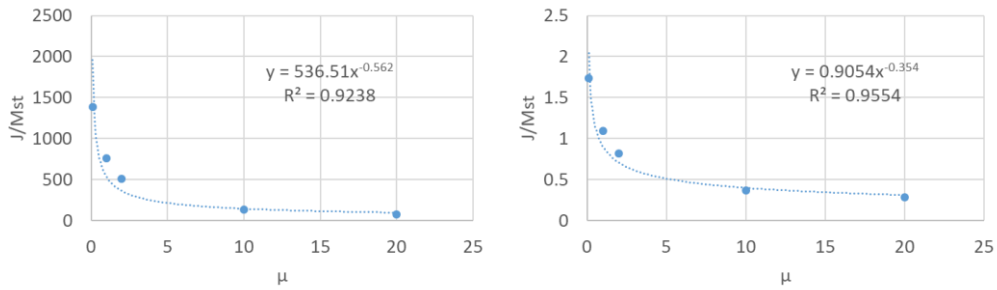

(a) *(b)*

Figure 3.12: Specific inertance variation for SAM variation under (a) harmonic displacement input (b) harmonic force input

The SAM and SAL which are expected to act as the mass and radius of the flywheel have a direct dependence on the specific inertance as explained in the Chapter I, but from the Figure 3.12 and Figure 3.13 it is observed that specific inertance of the structure decreases with increase in the SAM and SAL, this might be because in the rack-and-pinion inerter the rack (first terminal) and the flywheel move in the same sense but in the potential kinematically simpler structure the tip mass (first terminal) and the SAM move in the opposite sense, due to the cancellation effect in the structure we see a decreasing trend in the specific inertance as observed from the simulations.

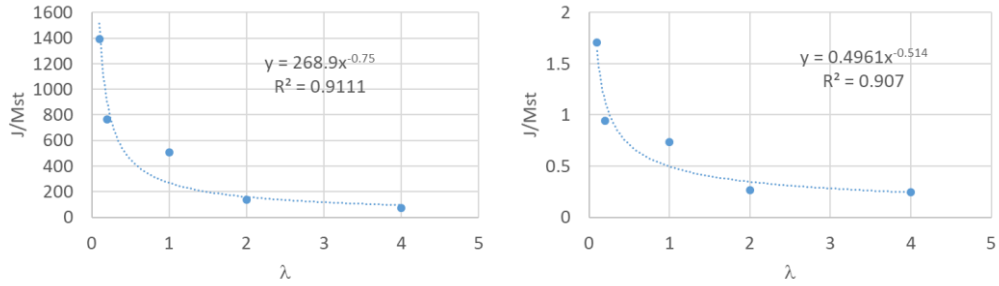

(a) *(b)*

Figure 3.13: Specific inertance variation for SAL variation under (a) harmonic displacement input (b) harmonic force input

The cause for the high specific inertance values for the HFI case is explainable, the snap through motion is captured only in the HFI case, when the tip mass snaps to the stable position very high accelerations are achieved due to the sudden movement, due to high accelerations the denominator value in the Equation 3.14 increases and very less specific inertance values are observed when compared to the HDI case.

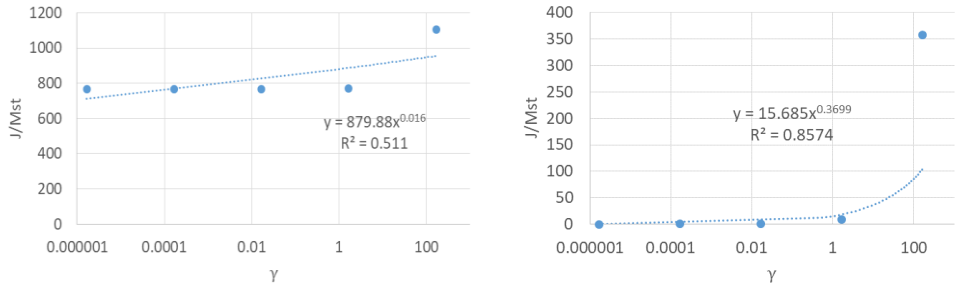

(a) *(b)*

Figure 3.14: Specific inertance variation for damping constant variation under (a) harmonic displacement input (b) harmonic force input

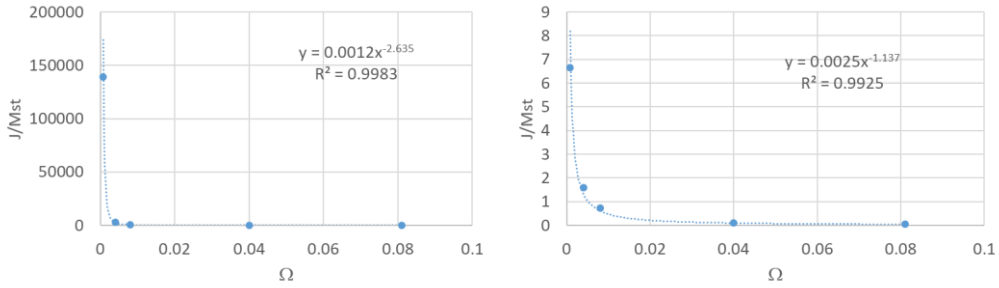

(a) *(b)*

Figure 3.15: Specific inertance variation for excitation frequency variation under (a) harmonic displacement input (b) harmonic force input

When the damping in the system increase more energy is dissipated due to very high resistance offered it, in the HDI case very high forces are observed because as the displacement is controlled no matter what the damping is the displacement is confined and the acceleration is the same hence we can observe a increasing trend in the specific inertance as reported in the Figure 3.14 (a). In the HFI case due to very less damping initial transience is high and gradually reduce to almost no transience due to that an increasing trend is observed in Figure 3.14 (b).

The frequency of excitation also has an effect on the specific inertance, at low frequencies very high specific inertance is observed as shown in the Figure 3.15 (a), due to very less acceleration and at high frequencies very high acceleration is achieved. Similar trend can be observed in the HFI case shown in the Figure 3.15 (b)

3.7 Summary

The structural inerter which was characterized in the first section is restricted to low frequencies and it is observed that as the frequency increases specific inertance decays to zero in a negative exponential trend. A potential kinematically simpler structure which may have an inerter like behavior and can be used in miniature scale was modeled in this section. The EOM was derived using the Hamilton's principle based on Lagrange's method and the structure was studied under two cases harmonic displacement input (HFI) and harmonic force input. The key parameters were

identified and they were varied to study the effect of them on the specific inertance of the structure. Then using the force and acceleration histories specific inertance was calculated and some interesting trends in the specific inertance with the key parameters were observed. It was inferred that the decreasing trend in the specific inertance with SAM and SAL variation was due to the opposite movement of the first terminal (tip mass m_1) and the SAM m_2 where as in the structural inerter the first terminal (rack) and the flywheel move in the same sense. Chapter I dealt with the inherent nonlinearity in the structural inerter, in the next chapter the wave dispersion characteristics of acoustic metamaterials having intentional nonlinear inerters in the local attachments is discussed.

CHAPTER IV

NONLINEAR INERTANT ACOUSTIC METAMATERIALS

4.1 Introduction & Motivation

Acoustic metamaterials are a class of metamaterials which derive their unique dynamic properties from the locally engineered structures. Previously many studies typically used local linear or nonlinear spring to study the wave propagation characteristics [63]. Recent discovered element which completes the force-current analogy is the inerter, which has the dynamic mass amplification affect and it is mostly used in vibration suppression or isolation purposes. Kulkarni and Manimala [65] recently have explored the effect of adding a linear inerter in the local attachments and in the lattice to study the longitudinal wave propagation characteristics. As Section I deals with the inherent nonlinearity that is present in the structural inerter, this section explores the effect of adding nonlinear inerters to the acoustic metamaterials in the local attachments of the discrete element lattice is investigated and different nonlinearities are explored in the subsequent sections.

The effective mass model for the lumped parameter model with local nonlinear inerters is discussed first. Two cases of nonlinear inerters in local attachment are studied which are frequency dependent and acceleration dependent. The effect of nonlinearities on the bandgap properties, degree of attenuation and passive wave filtering are studied. The results are obtained in the form of dispersion relation, are used to study different properties of the wave propagation in 1D lattice

4.2 Analytical Model

An infinite one dimensional discrete mass-spring system is considered as shown in the Figure 4.1 with local linear spring and nonlinear inerter. A unit cell is arbitrarily chosen along the infinite 1D system and assumed to be the j^{th} cell. The model illustrated in the Figure 4.1 (a) is analyzed using the effective mass approach [59] in which the host mass and the local linear spring and nonlinear inerter are subsumed into one single mass which is the effective mass as shown in the Figure 4.1 (b).

The host structure is discretized into mass-spring lattice of lattice length L, each unit cell has a lattice/host mass m_1, lattice/host spring stiffness k_1. The local resonator attachment has a local mass m_2, spring of stiffness k_2 with nonlinear inertance $J(\bar{\omega}, \ddot{u})$.

The dispersion characteristics of the nonlinear inertant acoustic metamaterials (NLIAM) is analyzed in two different categories which are the frequency dependent and acceleration dependent models. The following nonlinearities in the inerter are considered

(i) Frequency-dependent inertance

(a) Inverse square law inertance

(b) Power law inertance

(ii) Acceleration-dependent inertance

(a) Duffing-type inertance

Local inertant acoustic metamaterial (LIAM) is the limiting case for all the models mentioned above.

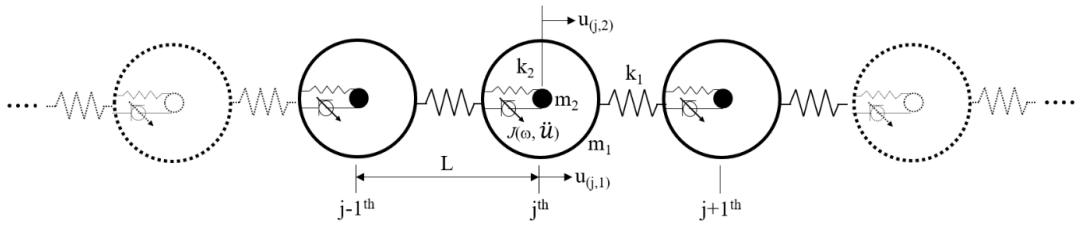

(a)

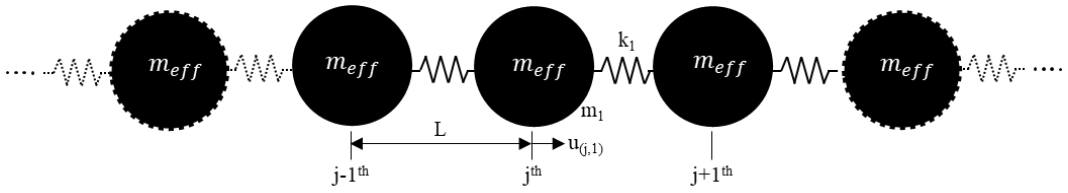

(b)

Figure 4.1: (a) Discrete element lattice representation of a one-dimensional nonlinear inertant acoustic metamaterial (NLIAM) and (b) its effective model.

4.2.1 NLIAM with Frequency-Dependent Inertance

The wave propagation characteristics or the dispersion characteristics of a 1D locally resonant acoustic metamaterials (LRAM), which have local linear resonator within a host structure or material are often analyzed using their representative discrete element lattice [59]. In this 1D infinite mass-spring system is represented as a monoatomic chain with each mass designated by an effective mass. The effective mass approach [59] is necessary to study the effect of both degrees of freedom. Due to the presence of a local linear resonator there exists a tunable bandgap between acoustic and optical modes where the lower bound of the bandgap corresponds to the local resonance frequency, whereas the upper bound is a function of ratio of attachment mass to host mass.

The waves within the bandgap cannot propagate through the system because the total energy is absorbed by the local resonator. The attenuation of the wave also depends on the

attenuation factor (β) which is the imaginary part of the wavenumber which is theoretically unbounded at the lower bound of the bandgap. Therefore attenuation of the waves is higher only near the lower bound of the bandgap which is a smaller frequency range. From the effective mass approach the dispersion relation for the LRAM represented by its discrete element lattice model is expressed as

$$\mu = qL = \cos^{-1}\left[1\frac{m_{eff}\bar{\omega}^2\omega_n^2}{2k_1}\right] \tag{4.1}$$

Where $\mu = qL = \alpha + i\beta$ is the complex wavenumber, $\omega_n = \sqrt{k_2/m_2}$ is the local resonance frequency, and $\bar{\omega} = \omega/\omega_n$ is the nondimensional excitation frequency. The frequency-dependent effective mass for the LRAM is given by

$$m_{eff}^{LRAM} = \left[(m_1 + m_2) - \frac{m_2}{1 - \frac{1}{\bar{\omega}^2}}\right] \tag{4.2}$$

At $\bar{\omega} = 1$ it can be observed that the effective mass becomes unbounded and thereafter remains negative up to $\bar{\omega} = \sqrt{1 + m_2/m_1}$. This frequency range of effective mass negativity corresponds to the band gap. Further, the nondimensional complex wavenumber can be written as $qL = \alpha + i\beta$, where α the real part is the phase constant that establishes the propagation modes and β the imaginary part is termed as the attenuation factor, which indicates the existence of band gaps and gives a measure of the degree of attenuation with the band gaps. Now, if a linear inerter (J_0) is attached in parallel to the resonator's spring (k_2) then the LRAM is converted to locally inertant acoustic metamaterial (LIAM) for which the effective mass expression is given as follows

$$m_{eff}^{LIAM} = \left[(m_1 + m_2) - \frac{m_2\bar{\omega}^2}{\bar{\omega}^2(1 + \gamma_0) - 1}\right] \tag{4.3}$$

Where $\gamma_0 = J_0/m_2$ is the ratio of the static inertance to the attachment mass. Due to the inerters participation in the local attachment lowers the local resonance frequency as it acts as additional mass and hence the lower bound of the band gap. But the advantage of adding an inerter

instead of a mass is the inerter provides a high dynamic mass compared to the static mass of the device. Now if the denominator of the second term on the right-hand side (RHS) in Equation 4.3 tends to a very small positive value, the effective mass has a very large negative value which results in a high attenuation factor (β). Therefore, a frequency-dependent nonlinear inertance could conceivably provide a means to ensure that degree of attenuation is retained at an appreciably high value for an extended frequency range, especially below the LRAM's band gap. This condition can be enforced as

$$\bar{\omega}^2(1+\gamma) - 1 = \epsilon \tag{4.4}$$

Where ϵ is an arbitrarily small positive value that ensures the desired degree of attenuation and $\gamma(\bar{\omega}) = J(\bar{\omega})/m_2$, which is the required nonlinear inertance and is easily obtained as

$$\gamma(\bar{\omega}) = \frac{1+\epsilon}{\bar{\omega}^2} - 1 \equiv \frac{\gamma_n}{\bar{\omega}^2} + \gamma_\infty \tag{4.5}$$

From Equation 4.5 it can be inferred that an inverse square relationship between γ and $\bar{\omega}$ is required to ensure high attenuation across all frequencies. Also, it can be observed that when $\bar{\omega} \rightarrow 0$, the nonlinear inertance, γ becomes unbounded and $\bar{\omega} > \sqrt{1+\epsilon}$, γ becomes negative both of which are not realistic. Therefore, realizing the requisite inverse square frequency-dependence for inertance that ensures high attenuation across the entire frequency bandwidth is not practical. This indeed becomes necessary to explore other types of nonlinear inertance models which are practically achievable while being a reasonably close approximation to the required inverse square law relation for as wide as a bandwidth possible, especially for frequencies below the LIAM's bandgap.

A ball-screw inerter [4, 6] is considered as the basis and some notional concepts for the variable inertance are postulated which display frequency-dependent changes in their inertance. Three concepts are postulated – (i) sleeve-type, (ii) radial buckling-type and (iii) clutch-type are shown in Figure 4.2. Basically, the aim of introducing frequency-dependent inertance is achieved

by varying the mass participation in flywheel in its rotary motion which is caused by the reciprocation of the screw. In the clutch-type could provide an inerter which displays an increase in inertance with increase in the frequency of excitation. As the frequency of excitation is increased more number of plates of the flywheel rotate together increasing the mass participation due to higher centrifugal force, which increase the thickness of the flywheel but the radius of gyration doesn't change. Where as in the radial-buckling and the sleeve type concepts decrease in inertance with increase in frequency of excitation can be achieved. In the radial-buckling type concept envisions the use of a radially-graded structural material for the flywheel to provide a similar variation in the inertance. This flywheel could conceivably be fabricated similar to mechanical metamaterials using hybrid techniques consisting of an additively manufactured flexible host structure having concentric shear-induced buckling bands along with machined metallic inclusions or inserts to provide the radial gradation in mass. Such a concept would enable full mass participation of the radially-graded flywheel at low excitation frequencies with incremental reduction in mass participation with increase in excitation frequency due to sequential buckling of the radially-graded bands. In the sleeve-type concept utilizes a flywheel which has several concentric sleeves held in contact with each other with friction. At low frequencies due to low velocities all of the sleeves participate in the flywheel rotary motion increasing its mass as well as the radius of gyration which increase the inertance. But at higher frequencies due to high velocities the sleeves slip on the surface reducing the number of active sleeves and reduces the mass and radius of gyration which reduces the inertance. The detailed design or analysis of these concepts are reserved for future studies but they serve as a basis to model the nonlinear inerters in structural and even in miniature scale which can be used in metamaterials with advanced wave manipulation capabilities.

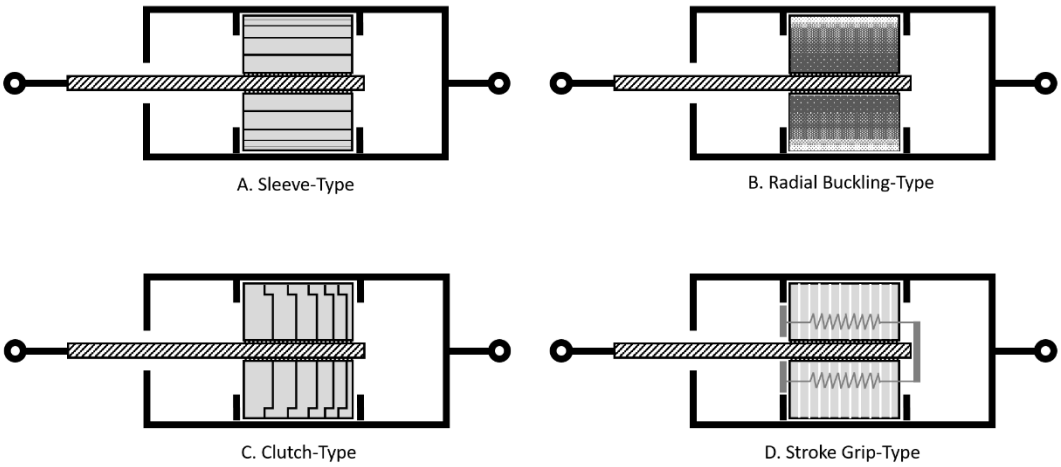

Figure 4.2: Conceptual schematics for potential frequency-dependent – (a) Sleeve-Type, (b) Radial Buckling-Type, (c) Clutch-Type, and acceleration-dependent – (d) Stroke Grip-Type nonlinear inerters.

In contrast to the desired inverse-square relationship for the inertance in order to ensure a wide bandwidth of appreciable attenuation especially for the low frequency regime below the LIAM's band gap, the potential concepts that could be explored to realize nonlinear inertance in practice would have bounded and positive inertance throughout the bandwidth. The concepts discussed above have a piecewise constant frequency-dependent inertance but eventually continuously variable ones could be potentially developed. One way to theoretically approximate the inverse square law inertance is by using a power law model which is of the form as follows

$$\gamma(\bar{\omega}) = \gamma_\infty + (\gamma_0 - \gamma_\infty) r^{-\bar{\omega}} \tag{4.6}$$

Where $\gamma_\infty = J_\infty / m_2$ the nondimensionalized high frequency limiting value for the inertance is, $\gamma_0 = J_0 / m_2$ is the nondimensionalized low frequency limiting value for the inertance, and r is a rate factor that controls the nonlinearity. A rate factor which doesn't vary with the frequency that represents the best nonlinear variation of the inertance for the physically realizable device as well as one that closely approximates the desired inverse square law relationship in the

low-frequency ($\bar{\omega} < 1$) regime needs to be selected. As discussed in the literature [2] the highest possible inertance to static mass ratio is 300 and it is chosen as the low-frequency limiting value of $\gamma_0 = J_0/m_2 = 300$. At high frequency the inertance can be expected to tend to the static mass of the device which is subsumed into the attachment mass. Hence, this limit is set to $\gamma_\infty = J_\infty/m_2 = 1$. The inertance in the power law tends to a finite low-frequency limit of 300, for certain bandwidth in the extremely low-frequency regime it becomes smaller than the desired inertance as per the inverse square law. But for the rest of the frequency above the bandwidth, the inverse square law model remains well below the power law model. In order to enforce that the power law remains close to the inverse square law model the rate factor is chosen such that they both touch one more time after the initial crossover point. For this condition to satisfy the rate factor can be numerically obtained as $r = 18395$.

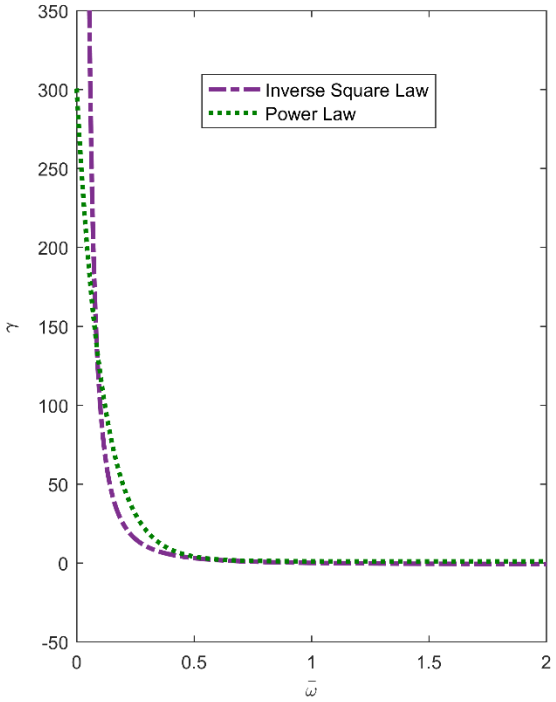

Figure 4.3: Comparison of inverse square law inertance and its approximation using the power law.

Figure 4.3 is the comparison of the inverse square law and the power law inertance models. The parameters used for the inverse square law are $ISL: [\gamma_n, \gamma_\infty] = [1.01, -1]$ and the parameters

used for the power law model are PL: $[\gamma_0, \gamma_\infty, r] = [300,1,18395]$. Both the curves first cross each other at $\bar{\omega} = 0.0856$ and the next cross over point is in the vicinity of $\bar{\omega} = 0.57$.

4.2.2 NLIAM with Acceleration-Dependent Inertance

The acceleration-dependent nonlinear inertance is inspired from the Duffing-type oscillator which exhibits amplitude-dependent cubically nonlinear stiffness, a similar type for Duffing-type inertance is postulated. The Duffing-type nonlinear inertance in this case is a function of the relative acceleration across the two terminals of the inerter and is defined by the relationship as follows

$$J(\ddot{u}) = J_0 \pm J_n \ddot{u}^2 \tag{4.7}$$

Where, J_0 is the linear inertance, J_n is the parameter that controls the nonlinearity, and $\ddot{u}$ is the relative acceleration across the two terminals of the inerter. The force response of this nonlinear inerter would be as follows

$$F = J\ddot{u} = J_0\ddot{u} \pm J_n\ddot{u}^3 \tag{4.8}$$

The above mentioned Duffing-type inertance can be realized by a variation of the clutch-type concept that may be termed as the stoke-grip-type as shown in the Figure 4.2 which has an active amplitude-activated mechanism to vary the mass of the flywheel. The 1D infinite discrete lattice model of the NLIAM is shown in the Figure 4.1 that incorporates weekly nonlinear Duffing-type inerter in parallel with the linear spring of each attachment mass. A perturbation approach based on the method of multiple scales [66] is used to obtain the first order correction to the linear dispersion relation for this NLIAM due to the presence of Duffing-type inerter in the microstructure. A j^{th} unit cell is arbitrarily chosen in the infinite discrete lattice model, the equations of motion of the unit cell are

$$m_1\ddot{u}_{j,1} + k_1(2u_{j,1} - u_{j+1,1} - u_{j-1,1}) + k_2(u_{j,1} - u_{j,2}) + J_0(\ddot{u}_{j,1} - \ddot{u}_{j,2}) + \varepsilon J_n(\ddot{u}_{j,1} - \ddot{u}_{j,2})^3 = 0 \quad (4.9)$$

$$m_2\ddot{u}_{j,2} + k_2(u_{j,2} - u_{j,1}) + J_0(\ddot{u}_{j,2} - \ddot{u}_{j,1}) + \varepsilon J_n(\ddot{u}_{j,2} - \ddot{u}_{j,1})^3 = 0 \quad (4.10)$$

Where ε is an arbitrarily small perturbation parameter used to enforce weak nonlinearity. For the purposes of the ensuing analysis, the following composite and non-dimensional parameters are defined.

$$\omega_n = \sqrt{k_2/m_2} \quad (4.11a),\ \bar{\omega} = \omega/\omega_n \quad (4.11b),\quad \tau = \omega t \quad (4.11c),$$

$$\theta_{12} = m_1/m_2 \quad (4.11d),\ \delta_{12} = k_1/k_2 \ (4.11e)$$

$$\gamma = J_0/m_2 \quad (4.12a),\ \Gamma = J_n L^2 \omega_n^4/m_2 \quad (4.12b),\ \bar{\Gamma} = \Gamma/L^2 \ (4.12c)$$

Where ω_n is the local resonance frequency of the spring, ω is the frequency of excitation, $\bar{\omega}$ is the nondimensionalized frequency of excitation, τ is the nondimensionalized time, θ_{12} is the mass ratio, δ_{12} is the stiffness ratio, γ is the linear inertance ratio, Γ is the nondimensionalized nonlinear inertance ratio, and $\bar{\Gamma}$ is its modified dimensional form used for convenience. Reconfiguring the equations of motion given by Equation 4.9 and Equation 4.10 above in terms of these parametric definitions the following equations are obtained

$$\theta_{12}\,\bar{\omega}^2\frac{d^2u_{j,1}}{d\tau^2} + \delta_{12}(2u_{j,1} - u_{j+1,1} - u_{j-1,1}) + (u_{j,1} - u_{j,2}) + \gamma\bar{\omega}^2\left(\frac{d^2u_{j,1}}{d\tau^2} - \frac{d^2u_{j,2}}{d\tau^2}\right) + \varepsilon\bar{\Gamma}\bar{\omega}^6\left(\frac{d^2u_{j,1}}{d\tau^2} - \frac{d^2u_{j,2}}{d\tau^2}\right)^3 = 0 \quad (4.13)$$

$$\bar{\omega}^2\frac{d^2u_{j,2}}{d\tau^2} + (u_{j,2} - u_{j,1}) + \gamma\bar{\omega}^2\left(\frac{d^2u_{j,2}}{d\tau^2} - \frac{d^2u_{j,1}}{d\tau^2}\right) + \varepsilon\bar{\Gamma}\bar{\omega}^6\left(\frac{d^2u_{j,2}}{d\tau^2} - \frac{d^2u_{j,1}}{d\tau^2}\right)^3 = 0 \quad (4.14)$$

Now introducing the first order corrections to the displacement and frequency which are defined as

$$u = u^{(0)} + \varepsilon u^{(1)} + O(\varepsilon^2) \tag{4.15}$$

$$\omega = \omega_0 + \varepsilon\omega_1 + O(\varepsilon^2) \tag{4.16}$$

For easy understanding of the equations, superscripted order numbers placed in parenthesis are used for the displacement correction whereas the subscripted order numbers are used for the frequency correction terms. Substituting the corrections which are Equations 4.15 and 4.16 into the equation of motion for the lattice mass (m_1) which is given by the Equation 4.13, we have the following equation

$$\theta_{12}\,(\bar{\omega}_0 + \varepsilon\bar{\omega}_1)^2\,\frac{d^2}{d\tau^2}(u_{j,1}^{(0)} + \varepsilon u_{j,1}^{(1)}) + \delta_{12}\big(2(u_{j,1}^{(0)} + \varepsilon u_{j,1}^{(1)}) -$$

$$(u_{j+1,1}^{(0)} + \varepsilon u_{j+1,1}^{(1)}) - (u_{j-1,1}^{(0)} + \varepsilon u_{j-1,1}^{(1)})\big) + \big((u_{j,1}^{(0)} + \varepsilon u_{j,1}^{(1)}) -$$

$$(u_{j,2}^{(0)} + \varepsilon u_{j,2}^{(1)})\big) + \gamma(\bar{\omega}_0 + \varepsilon\bar{\omega}_1)^2\left(\frac{d^2(u_{j,1}^{(0)} + \varepsilon u_{j,1}^{(1)})}{d\tau^2} - \frac{d^2(u_{j,2}^{(0)} + \varepsilon u_{j,2}^{(1)})}{d\tau^2}\right) +$$

$$\varepsilon\bar{\Gamma}(\bar{\omega}_0 + \varepsilon\bar{\omega}_1)^6\left(\frac{d^2(u_{j,1}^{(0)} + \varepsilon u_{j,1}^{(1)})}{d\tau^2} - \frac{d^2(u_{j,2}^{(0)} + \varepsilon u_{j,2}^{(1)})}{d\tau^2}\right)^3 = 0 \tag{4.17}$$

In the above equation the zeroth and first order terms of the perturbation parameter ε are separated to yield the following equations

$$\varepsilon^0\colon\quad \theta_{12}\bar{\omega}_0^2\,\frac{d^2u_{j,1}^{(0)}}{d\tau^2} + \delta_{12}\left(2u_{j,1}^{(0)} - u_{j-1,1}^{(0)} - u_{j+1,1}^{(0)}\right) + \left(u_{j,1}^{(0)} - u_{j,2}^{(0)}\right) +$$

$$\gamma\bar{\omega}_0{}^2\left(\frac{d^2u_{j,1}^{(0)}}{d\tau^2} - \frac{d^2u_{j,2}^{(0)}}{d\tau^2}\right) = 0 \tag{4.18}$$

$$\varepsilon^1\colon\quad \theta_{12}\left(\bar{\omega}_0^2\,\frac{d^2u_{j,1}^{(1)}}{d\tau^2} + 2\bar{\omega}_0\bar{\omega}_1\,\frac{d^2u_{j,1}^{(0)}}{d\tau^2}\right) + \delta_{12}\big(2u_{j,1}^{(1)} -$$

$$u_{j-1,1}^{(1)} - u_{j+1,1}^{(1)}\big) + \big(u_{j,1}^{(1)} - u_{j,2}^{(1)}\big) + \gamma\bar{\omega}_0{}^2\left(\frac{d^2u_{j,1}^{(1)}}{d\tau^2} - \frac{d^2u_{j,2}^{(1)}}{d\tau^2}\right) + 2\gamma\bar{\omega}_0\bar{\omega}_1\left(\frac{d^2u_{j,1}^{(0)}}{d\tau^2} - \right. \tag{4.19}$$

$$\left.\frac{d^2u_{j,2}^{(0)}}{d\tau^2}\right) + \bar{\Gamma}\bar{\omega}_0^6\left(\frac{d^2u_{j,1}^{(0)}}{d\tau^2} - \frac{d^2u_{j,2}^{(0)}}{d\tau^2}\right)^3 = 0$$

To obtain propagating wave solutions, a harmonic displacement excitation boundary condition is applied to the first lattice mass and a harmonic wave solution is assumed for the ε^0 order equation. The zeroth order displacement solution for the first lattice mass (m_1) in the j^{th} unit can be represented as

$$u_{j,1}^{(0)} = \frac{A_1^{(0)}}{2} e^{i(qjL)} e^{i\tau} + \frac{\bar{A}_1^{(0)}}{2} e^{-i(qjL)} e^{-i\tau} \tag{4.20}$$

Where q the wave is number and L is the lattice length.

Similarly the zeroth order displacement solutions for the lattice masses $j-1^{th}$ and $j+1^{th}$ units can be expressed as follows

$$u_{j+1,1}^{(0)} = \frac{A_1^{(0)}}{2} e^{i(qjL)} e^{i\tau} e^{i(qL)} + \frac{\bar{A}_1^{(0)}}{2} e^{-i(qjL)} e^{-i\tau} e^{-i(qL)} \tag{4.21}$$

$$u_{j-1,1}^{(0)} = \frac{A_1^{(0)}}{2} e^{i(qjL)} e^{i\tau} e^{-i(qL)} + \frac{\bar{A}_1^{(0)}}{2} e^{-i(qjL)} e^{-i\tau} e^{i(qL)} \tag{4.22}$$

The sum of the Equations 4.21 and 4.22 can be simplified as

$$u_{j+1,1}^{(0)} + u_{j-1,1}^{(0)} = 2\cos(qL)\left[\frac{A_1^{(0)}}{2} e^{i(qjL)} e^{i\tau} + \frac{\bar{A}_1^{(0)}}{2} e^{-i(qjL)} e^{-i\tau}\right] = 2u_{j,1}^{(0)} \cos(qL) \tag{4.23}$$

The lattice mass zeroth order equation given by Equation 4.18 can be simplified as

$$\varepsilon^0: \quad -\theta_{12}\bar{\omega}_0^2 u_{j,1}^{(0)} + \delta_{12}\left(2u_{j,1}^{(0)} - 2u_{j,1}^{(0)}\cos(qL)\right) + \left(u_{j,1}^{(0)} - u_{j,2}^{(0)}\right) + \gamma\bar{\omega}_0^2\left(-u_{j,1}^{(0)} + u_{j,2}^{(0)}\right) = 0 \tag{4.24}$$

(4.25)

$$\varepsilon^0: \quad u_{j,1}^{(0)}[-\theta_{12}\bar{\omega}_0^2 + 2\delta_{12}(1-\cos(qL)) + 1 - \gamma\bar{\omega}_0^2] = u_{j,2}^{(0)}[1 - \gamma\bar{\omega}_0^2]$$

Similarly, substituting the first order corrections given by Equations 4.15 and 4.16 into the equation of motion of the attachment mass m_2 obtained in Equation 4.14, the zeroth order equation for the attachment mass is as follows

$$\varepsilon^0: \quad \bar{\omega}_0^2 \frac{d^2u_{j,2}^{(0)}}{d\tau^2} + \left(u_{j,2}^{(0)} - u_{j,1}^{(0)}\right) + \gamma\bar{\omega}_0{}^2\left(\frac{d^2u_{j,2}^{(1)}}{d\tau^2} - \frac{d^2u_{j,1}^{(1)}}{d\tau^2}\right) =$$

$$\bar{\omega}_0^2\left(-u_{j,2}^{(0)}\right) + \left(u_{j,2}^{(0)} - u_{j,1}^{(0)}\right) + \gamma\bar{\omega}_0^2\left(-u_{j,2}^{(0)} + u_{j,1}^{(0)}\right) = 0 \tag{4.26}$$

$$\varepsilon^0: \quad u_{j,2}^{(0)}(1 - \bar{\omega}_0^2 - \gamma\bar{\omega}_0^2) = u_{j,1}^{(0)}(1 - \gamma\bar{\omega}_0^2) \tag{4.27}$$

The linear dispersion relation is recovered by eliminating $u_{j,2}^{(0)}$ from the zeroth order equations of motion given by Equations 4.25 and 4.27

$$\varepsilon^0: \quad (1 - (1+\gamma)\bar{\omega}_0^2)[1 - (\theta_{12} + \gamma)\bar{\omega}_0^2 + 2\delta_{12}(1 - \cos(qL))] = (1 - \gamma\bar{\omega}_0^2)^2 \tag{4.28}$$

Now introducing $\mu = qL$ which is the nondimensional wavenumber, the linear dispersion relations becomes

$$\bar{\omega}_0^4[\theta_{12} + \gamma + \theta_{12}\gamma] - \bar{\omega}_0^2[1 + \theta_{12} + 2\delta_{12}(1+\gamma)(1-\cos(\mu))] + 2\delta_{12}(1-\cos(\mu)) = 0 \tag{4.29}$$

Equation 4.29 is solved to obtain the solutions that give positive values for the frequency, resulting in the well-known explicit form for the linear dispersion relation.

$$\bar{\omega}_0 = \sqrt{\frac{\{1+\theta_{12}+2\delta_{12}(1+\gamma)(1-\cos(\mu))\} \pm \sqrt{\{1+\theta_{12}+2\delta_{12}(1+\gamma)(1-\cos(\mu))\}^2 - 8\delta_{12}(\theta_{12}+\gamma+\theta_{12}\gamma)(1-\cos(\mu))}}{2(\theta_{12}+\gamma+\theta_{12}\gamma)}} \tag{4.30}$$

Further, the first order equation of motion for the lattice mass m_1 given by the Equation 4.19 is rewritten in the form

$$\theta_{12}\bar{\omega}_0^2\frac{d^2u_{j,1}^{(1)}}{d\tau^2}+\delta_{12}\left(2u_{j,1}^{(1)}-u_{j-1,1}^{(1)}-u_{j+1,1}^{(1)}\right)+\left(u_{j,1}^{(1)}-u_{j,2}^{(1)}\right)+\gamma\bar{\omega}_0{}^2\left(\frac{d^2u_{j,1}^{(1)}}{d\tau^2}-\frac{d^2u_{j,2}^{(1)}}{d\tau^2}\right)=-2\theta_{12}\bar{\omega}_0\bar{\omega}_1\frac{d^2u_{j,1}^{(0)}}{d\tau^2}-2\gamma\bar{\omega}_0\bar{\omega}_1\left(\frac{d^2u_{j,1}^{(0)}}{d\tau^2}-\frac{d^2u_{j,2}^{(0)}}{d\tau^2}\right)-\bar{\Gamma}\bar{\omega}_0^6\left(\frac{d^2u_{j,1}^{(0)}}{d\tau^2}-\frac{d^2u_{j,2}^{(0)}}{d\tau^2}\right)^3 \quad (4.31)$$

From Equations 4.18 and 4.31 it can be observed that the Equation 4.31 resembles the zeroth order case as given by Equation 4.18 but with a forcing function on the right-hand-side. Substituting the expressions for the lattice mass displacements from Equations 4.20 and 4.23, eliminating the attachment mass displacement by using the Equation 4.27 and expanding the forcing function on the right-hand-side and grouping on $e^{i(qjL+\tau)}$ and $e^{3i(qjL+\tau)}$. The Equation 4.31 can be expressed as

$$2\theta_{12}\bar{\omega}_0\bar{\omega}_1u_{j,1}^{(0)}+2\gamma\bar{\omega}_0\bar{\omega}_1\left(u_{j,1}^{(0)}-u_{j,2}^{(0)}\right)+\bar{\Gamma}\bar{\omega}_0^6\left(u_{j,1}^{(0)}-u_{j,2}^{(0)}\right)^3=2\bar{\omega}_0\bar{\omega}_1\left(\theta_{12}-\frac{\gamma\bar{\omega}_0{}^2}{1-(1+\gamma)\bar{\omega}_0{}^2}\right)\left[\frac{A_1^{(0)}}{2}e^{i(qjL)}e^{i\tau}+\frac{\bar{A}_1^{(0)}}{2}e^{-i(qjL)}e^{-i\tau}\right]-\bar{\Gamma}\bar{\omega}_0{}^6\left(\frac{\bar{\omega}_0{}^2}{1-(1+\gamma)\bar{\omega}_0{}^2}\right)^3\left[\left\{\frac{A_1^{(0)3}}{8}e^{3i(qjL)}e^{3i\tau}+\frac{\bar{A}_1^{(0)3}}{8}e^{-3i(qjL)}e^{-3i\tau}\right\}+\frac{3}{4}A_1^{(0)}\bar{A}_1^{(0)}\left\{\frac{A_1^{(0)}}{2}e^{i(qjL)}e^{i\tau}+\frac{\bar{A}_1^{(0)}}{2}e^{-i(qjL)}e^{-i\tau}\right\}\right]\equiv c_1e^{i(qjL+\tau)}+c_3e^{3i(qjL+\tau)}+c.c. \quad (4.32)$$

Where $c.c.$ denotes complex conjugate terms. Noting that in Equation 4.32 all the terms in the expansion of the forcing function on the right-hand-side that occur with the term $e^{i(qjL+\tau)}$ behave to force the first order equation of motion at resonance which leads to unbounded solutions. Hence, these terms are grouped as secular terms and must be equated to zero to result in bounded solutions. Hence the coefficient, c_1 in Equation 4.32 must be set to zero which results in the following condition

$$c_1\equiv\bar{\omega}_0\bar{\omega}_1\left(\theta_{12}-\frac{\gamma\bar{\omega}_0{}^2}{1-(1+\gamma)\bar{\omega}_0{}^2}\right)A_1^{(0)}-\bar{\Gamma}\bar{\omega}_0{}^6\left(\frac{\bar{\omega}_0{}^2}{1-(1+\gamma)\bar{\omega}_0{}^2}\right)^3\frac{3}{8}A_1^{(0)2}\bar{A}_1^{(0)}=0 \quad (4.33)$$

The above condition directly provides the first order correction as

$$\bar{\omega}_1 = \frac{3}{8}|A_1|^2 \bar{\Gamma} {\bar{\omega}_0}^5 \left(\frac{{\bar{\omega}_0}^2}{1-(1+\gamma){\bar{\omega}_0}^2}\right)^3 \left(\frac{1-(1+\gamma){\bar{\omega}_0}^2}{\theta_{12}-(\theta_{12}+\gamma+\theta_{12}\gamma){\bar{\omega}_0}^2}\right) \quad (4.34)$$

Now, using the above equation and substituting in the frequency correction defined in the Equation 4.16, the first order correction for the dispersion relationship is as follows

$$\bar{\omega} = \bar{\omega}_0 + \varepsilon \frac{3}{8}|A_1|^2 \bar{\Gamma} {\bar{\omega}_0}^5 \left(\frac{{\bar{\omega}_0}^2}{1-(1+\gamma){\bar{\omega}_0}^2}\right)^3 \left(\frac{1-(1+\gamma){\bar{\omega}_0}^2}{\theta_{12}-(\theta_{12}+\gamma+\theta_{12}\gamma){\bar{\omega}_0}^2}\right) \quad (4.35)$$

It is noted that $\bar{\omega}_0$ in the above expression is obtained from the linear dispersion relation given by the Equation 4.30. All the parameters in the Equation 4.35 are dimensionless except $|A_1|$ and $\bar{\Gamma}$. The amplitude of excitation has the dimension of length and the nonlinearity parameter has inverse square length dimension. These are nondimensionalized as $A^* = |A_1|/L$ and $\Gamma = \bar{\Gamma}L^2$ which are the nondimensional parameters corresponding to excitation amplitude and nonlinearity parameter. Now the Equation 4.35 can be rewritten as follows

$$\bar{\omega} = \bar{\omega}_0 + \varepsilon \frac{3}{8}{A^*}^2 \Gamma {\bar{\omega}_0}^5 \left(\frac{{\bar{\omega}_0}^2}{1-(1+\gamma){\bar{\omega}_0}^2}\right)^3 \left(\frac{1-(1+\gamma){\bar{\omega}_0}^2}{\theta_{12}-(\theta_{12}+\gamma+\theta_{12}\gamma){\bar{\omega}_0}^2}\right) \quad (4.36)$$

The above equation gives the shifts of the dispersion curve for the harmonic wave propagation through the NLIAM which is induced by the inclusion of the Duffing-type inertance in the local attachments.

It is also interesting to explore the first order correction of the local resonator mass m_2 using the same approach. The first order equation of motion for the attachment mass can be obtained from the Equation 4.14 as

$$\varepsilon^1: \quad \bar{\omega}_0^2 \frac{d^2 u_{j,2}^{(1)}}{d\tau^2} + \left(u_{j,2}^{(1)} - u_{j,1}^{(1)}\right) + \gamma {\bar{\omega}_0}^2 \left(\frac{d^2 u_{j,2}^{(1)}}{d\tau^2} - \frac{d^2 u_{j,1}^{(1)}}{d\tau^2}\right) =$$

$$-2\bar{\omega}_0\bar{\omega}_1 \frac{d^2 u_{j,2}^{(0)}}{d\tau^2} - 2\gamma\bar{\omega}_0\bar{\omega}_1 \left(\frac{d^2 u_{j,2}^{(0)}}{d\tau^2} - \frac{d^2 u_{j,1}^{(0)}}{d\tau^2}\right) - \bar{\Gamma}\bar{\omega}_0^6 \left(\frac{d^2 u_{j,2}^{(0)}}{d\tau^2} - \frac{d^2 u_{j,1}^{(0)}}{d\tau^2}\right)^3 \quad (4.37)$$

Similarly, expanding the forcing terms on the right-hand-side and grouping on $e^{i(qjL+\tau)}$ and $e^{3i(qjL+\tau)}$, Equation 4.37 can be expressed as follows

$$\begin{gathered}2\bar{\omega}_0\bar{\omega}_1 u_{j,2}^{(0)} + 2\gamma\bar{\omega}_0\bar{\omega}_1\left(u_{j,2}^{(0)} - u_{j,1}^{(0)}\right) + \bar{\Gamma}\bar{\omega}_0^6\left(u_{j,2}^{(0)} - u_{j,1}^{(0)}\right)^3 = \\ 2\bar{\omega}_0\bar{\omega}_1\left(\frac{1}{1-(1+\gamma)\bar{\omega}_0{}^2}\right)\left[\frac{A_1^{(0)}}{2}e^{i(qjL)}e^{i\tau} + \frac{\bar{A}_1^{(0)}}{2}e^{-i(qjL)}e^{-i\tau}\right] \\ +\bar{\Gamma}\bar{\omega}_0{}^6\left(\frac{\bar{\omega}_0{}^2}{1-(1+\gamma)\bar{\omega}_0{}^2}\right)^3\left[\left\{\frac{A_1^{(0)3}}{8}e^{3i(qjL)}e^{3i\tau} + \frac{\bar{A}_1^{(0)3}}{8}e^{-3i(qjL)}e^{-3i\tau}\right\} + \right. \\ \left.\frac{3}{4}A_1^{(0)}\bar{A}_1^{(0)}\left\{\frac{A_1^{(0)}}{2}e^{i(qjL)}e^{i\tau} + \frac{\bar{A}_1^{(0)}}{2}e^{-i(qjL)}e^{-i\tau}\right\}\right] \equiv c_1 e^{i(qjL+\tau)} + c_3 e^{3i(qjL+\tau)} + c.c.\end{gathered} \tag{4.38}$$

Enforcing the secular condition to avoid unbounded solutions as before yields

$$c_1 = 2\bar{\omega}_0\bar{\omega}_1\left(\frac{1}{1-(1+\gamma)\bar{\omega}_0{}^2}\right)\frac{A_1^{(0)}}{2} + \bar{\Gamma}\bar{\omega}_0{}^6\left(\frac{\bar{\omega}_0{}^2}{1-(1+\gamma)\bar{\omega}_0{}^2}\right)^3\frac{3}{4}A_1^{(0)}\bar{A}_1^{(0)}\frac{A_1^{(0)}}{2} = 0 \tag{4.39}$$

From Equation 4.39 the first order correction to the resonator mass response yields as

$$\bar{\omega}_1 = -\frac{3}{8}\bar{\Gamma}|A_1|^2\frac{\bar{\omega}_0{}^{11}}{\left(1-(1+\gamma)\bar{\omega}_0{}^2\right)^2} \tag{4.40}$$

Now, substituting this correction into the frequency equation given by Equation 4.16 gives the first order corrected frequency relation for the attachment mass as

$$\bar{\omega} = \bar{\omega}_0 - \varepsilon\frac{3}{8}\bar{\Gamma}|A_1|^2\frac{\bar{\omega}_0{}^{11}}{\left(1-(1+\gamma)\bar{\omega}_0{}^2\right)^2} \tag{4.41}$$

From Eq. 27, the zeroth order frequency-amplitude relationship for the resonator mass can be expressed as

$$u^* = \frac{u_{j,2}^{(0)}}{u_{j,1}^{(0)}} = \frac{1-\gamma\bar{\omega}_0^2}{1-\bar{\omega}_0^2-\gamma\bar{\omega}_0^2} \tag{4.42}$$

Where u^* is the ratio of the displacement of the resonator mass to that of the lattice mass which is a measure of the frequency response of the resonator mass and can be termed the

displacement transmissibility. This relationship can be inverted to obtain the zeroth order frequency in terms of the displacement transmissibility.

$$\bar{\omega}_0 = \sqrt{\frac{1-u^*}{\gamma - u^* - \gamma u^*}} \tag{4.43}$$

Substituting Equation 4.43 into Equation 4.41, the first order corrected frequency relationship for the resonator mass can be expressed in terms of the displacement transmissibility as

$$\bar{\omega} = \sqrt{\frac{1-u^*}{\gamma - u^* - \gamma u^*}} - \varepsilon \frac{3}{8} \bar{\Gamma} |A_1|^2 \frac{\left(\sqrt{\frac{1-u^*}{\gamma - u^* - \gamma u^*}}\right)^{11}}{\left[1 - (1+\gamma)\frac{1-u^*}{\gamma - u^* - \gamma u^*}\right]^2} \tag{4.44}$$

The dynamic characteristics of the NLIAM having acceleration-dependent inerters in the local attachment are discussed in the ensuing section.

4.3 Dispersion Characteristics

Based on the discrete element lattice representation the theoretical dispersion relations for NLIAM are investigated using numerical studies. The parameters are chosen such that the bandgap includes low frequencies (< 5 Hz) as structural inerters can be used at those frequencies. The base parametric setting used for all simulations is $[m_1, m_2, k_1, k_2, L] = [1,10,1000,100,1]$ with the values assumed to be in compatible units. All the parametric curves generated for each case are nondimensionalized.

4.3.1 NLIAM with Frequency-Dependent Inertance

In this section frequency-dependent NLIAM cases are studied. As the inertance doesn't depend on the excitation acceleration, effective mass model as shown in Equation 4.3 is used to plot the dispersion curves. Firstly, NLIAM with inverse square (ISL) is studied. The case specific base parameters for ISL are inverse square law (ISL) inertance (Eq. 5) is examined. The case specific

base parameters for ISL are $[\gamma_n, \gamma_\infty] = [1.01, -1]$ which ensure that the bandgap exists over almost entire frequency range of interest. Figure 4.4 shows the effect of varying the high frequency limit of the inertance $\gamma_\infty = J_\infty/m_2$ on the real part, α and imaginary part, β of the nondimensional wavenumber qL. In can be inferred that bandgap region where the imaginary part β is nonzero shifts towards higher frequencies as γ_∞ increases.

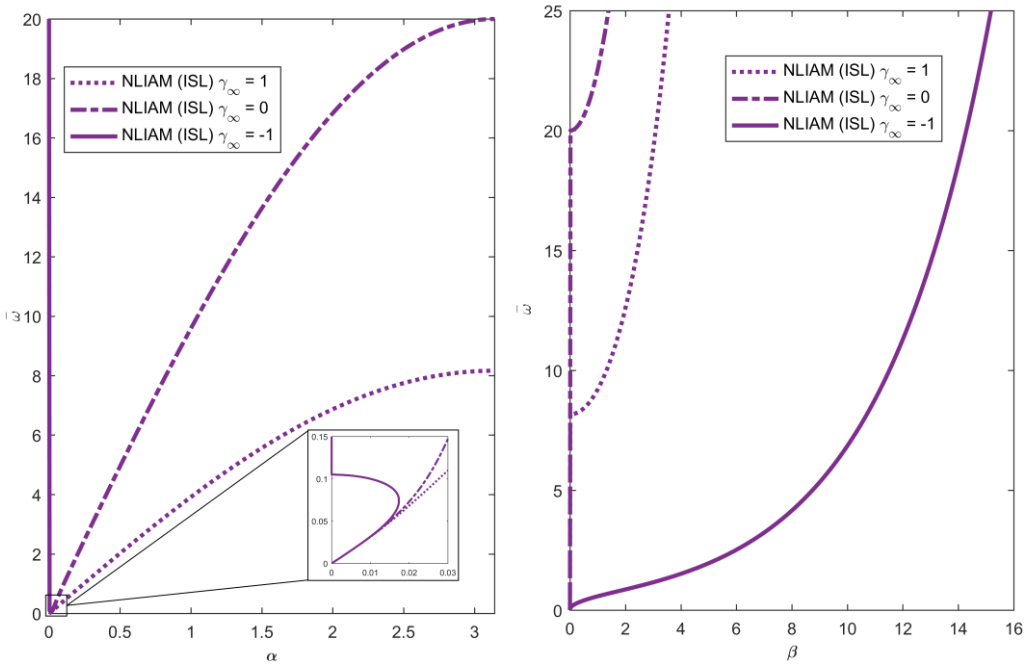

(a) *(b)*

Figure 4.4: Influence of the high frequency limit of the inertance, $\gamma_\infty = J_\infty/m_2$ on the (a) real and (b) imaginary parts of the wavenumber for NLIAM with inverse square law (ISL) inertance.

The band gap encompasses nearly the entire frequency range of interest as predicted when $\gamma_\infty = -1$. The effect of varying the nonlinear parameter which is $\gamma_n = J_n/m_2$ on the real part, α and imaginary part, β of the nondimensional wavenumber qL is shown in the Figure 4.5, clearly showing the significance of retaining this parameter as close to and above the LRAM's local resonance frequency ($\bar{\omega} = 1$) in order to maximize the bandgap which corresponds to the frequency range with nonzero β. In both parametric variations for ISL, it is interesting to note that the propagation mode denoted by the real part of the wavenumber, α can evince regions where the

slope is negative indicating negative group velocity can be achieved for the extremely low frequency range. This phenomenon is seen for the power law (PL) cases too.

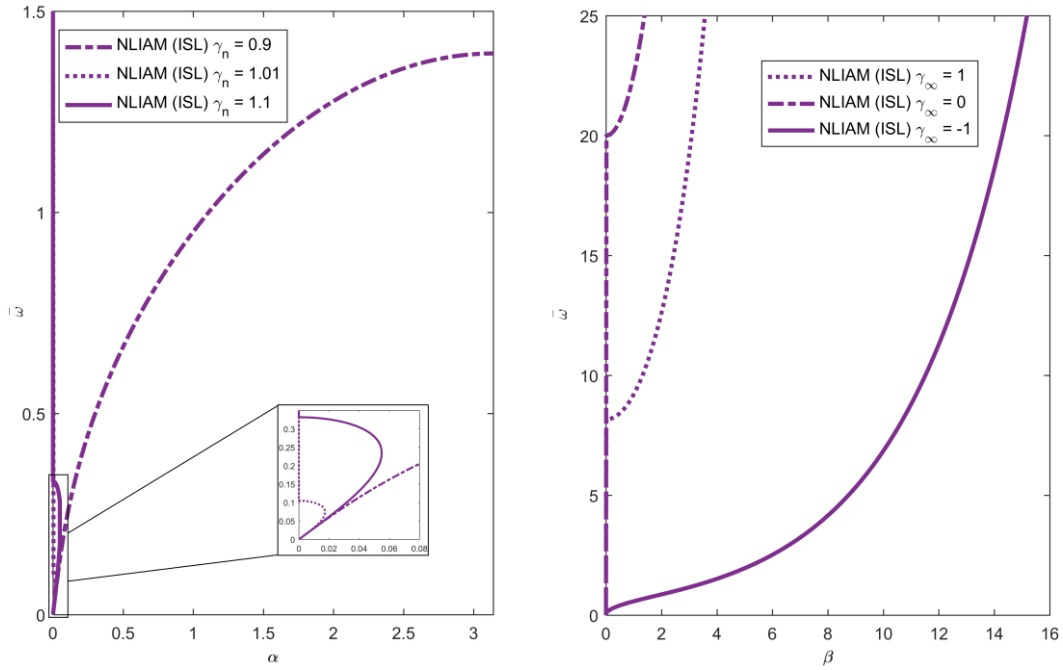

(a) *(b)*

Figure 4.5: Influence of the nonlinear inertance parameter, $\gamma_n = J_n/m_2$ on the (a) real and (b) imaginary parts of the wavenumber for NLIAM with inverse square law (ISL) inertance.

Similarly for the NLIAM with power law (PL) inertance which is described using the Equation 4.6, the dispersion behavior is obtained using the effective mass model given by the Equation 4.3. The base parameters used for this case are fixed and are $[\gamma_0, \gamma_\infty] = [300,1]$. The parameters are chosen based on the inertance values which are physically realizable as provided in the literature [2]. Figure 4.3 shows the best approximate to ISL using the PL where r is a tunable parameter is. The effect of varying the rate factor on the dispersion behavior of the NLIAM with PL inertance is shown in the Figure 4.6. When the rate factor $r = 10000$, is less than the optimal value ($r = 18395$), the attenuation factor β as well as the extent of bandgap both are diminished. When the rate factor $r = 25000$, is greater than the optimal value, a high degree of attenuation is obtained, but the bandgap becomes discontinuous due to the appearance of an additional

propagation mode in between the two discontinuous portions of the bandgap. Hence in order to maximize the attenuation in the low frequency regime for NLIAM with PL, an optimal choice of the rate factor is essential.

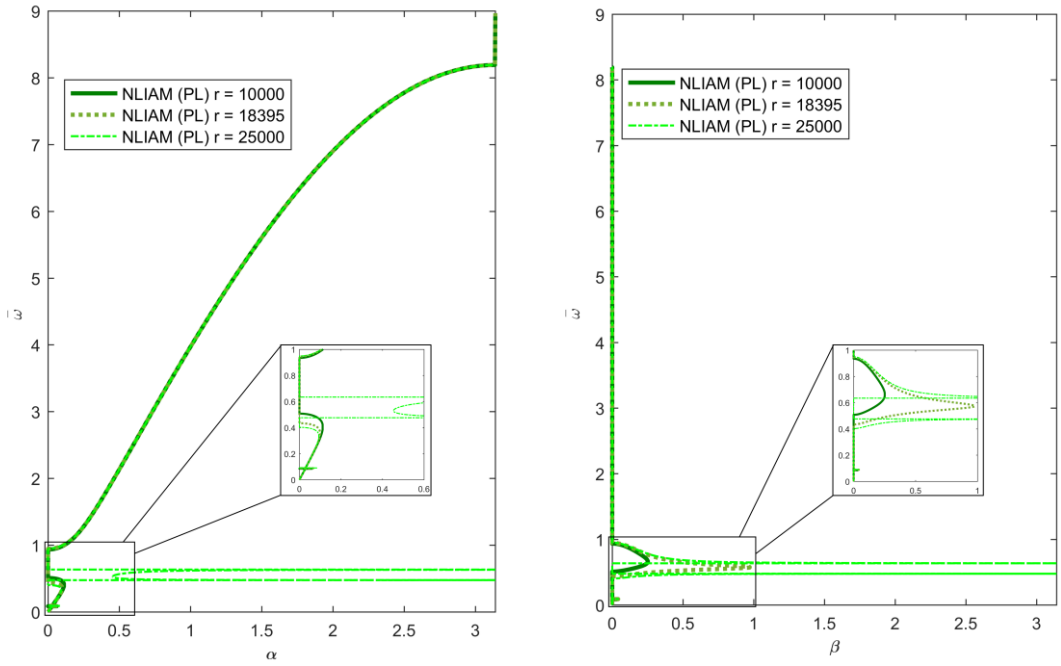

(a) *(b)*

Figure 4.6: Influence of the rate factor, r on the (a) real and (b) imaginary parts of the wavenumber for NLIAM with power law (PL) inertance.

Figure 4.7 is the comparison of the dispersion behavior for the LIAM (having static inertance $\gamma_0 = 1$), NLIAM with ISL inertance (having $[\gamma_n, \gamma_\infty] = [1.01, -1]$) and NLIAM with PL inertance (having $[\gamma_0, \gamma_\infty, r] = [300,1,18395]$). The LIAM's bandgap is shifted below the LRAM's local resonance frequency ($\bar{\omega} = 1$) due to the inclusion of the static inertance (set at $\gamma_0 = J_0/m_2 = 1$).This is because the static inerter increases the dynamic mass in the local attachments across entire bandwidth which lowers the resonant frequency of the local attachment. For the ISL inertance case it displays a nonzero β over the entire frequency range even in the extremely low frequency range. Increase in frequency increases the attenuation factor β which indicates high efficiency in attenuating high frequency waves.

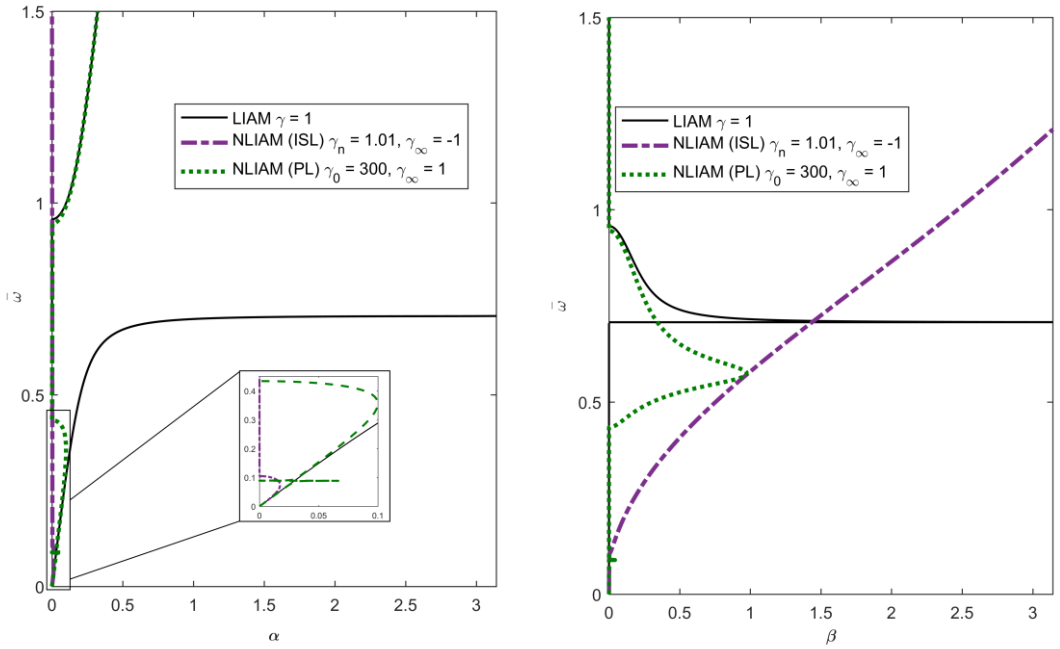

Figure 4.7: Comparison of (a) the real and (b) imaginary parts of the wavenumber for the locally inertant acoustic metamaterial (LIAM) and the nonlinear inertant acoustic metamaterial (NLIAM) with inverse square law and power law inertance.

From the Figure 4.7 it can be inferred that the power law (PL) inertance serves as a potentially physically realizable approximation to the ISL which delivers a widening of bandgap towards low frequencies. Substituting the power law (PL) inertance as given by Equation 4.6 in the dispersion relation from the effective mass model one can ascertain that the value of the cosine function exceeds 1 above $\bar{\omega} = 0.434$ resulting in the wave number becoming completely imaginary. The upper limit of the bandgap of LIAM case and PL case remain nearly unchanged at $\bar{\omega} = 0.957$ and $\bar{\omega} = 0.945$ respectively. But when comparing the lower limit of the bandgap nearly more than a 100% increase is obtained in the NLAIM with PL inertance. The attenuation factor in the NLIAM with PL inertance is relatively low compared to the LIAM, but the extent of the bandgap is high in the former covering the low frequency range. With only a small increase in the

static mass the gain the low frequency attenuation bandwidth could be realized as the nonlinear inerter displays a large frequency-dependent dynamic mass presence.

4.3.2 NLIAM with Acceleration-Dependent Inertance

In this section dispersion characteristics of the NLIAM with acceleration-dependent (AD) case are discussed, the base parameters used for this study are $[\gamma, \Gamma, A^*, \varepsilon] = [1,10,0.1,0.001]$. Firstly, due to the presence of the acceleration-dependent local attachments the shifts in the dispersion curves are examined by plotting the first order corrected dispersion given by the Equation 4.36. The variation of the excitation amplitude as well as the nonlinear parameter are considered as shown in the Figure 4.8. The shifts indicate higher influence in the low wavelength regime as compared to the lower shifts and influence in the high wavelength limit. This is experienced by the acoustical mode which is the low frequency mode below the bandgap as well as the optical mode which is the high frequency mode above the bandgap.

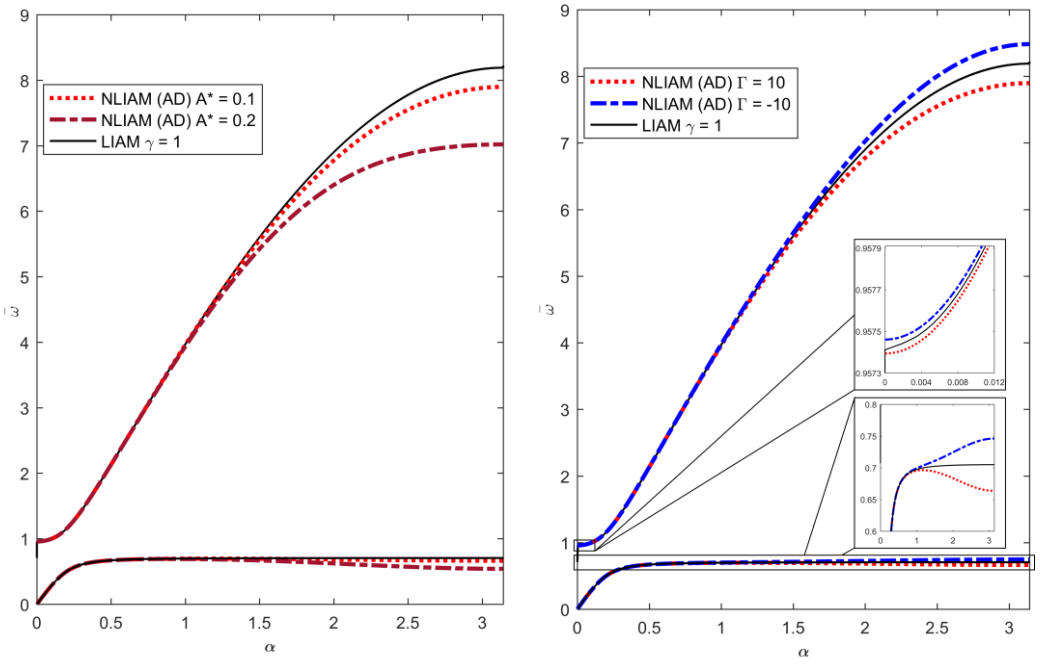

(a) *(b)*

Figure 4.8: Dispersion curve shifts for the NLIAM with acceleration-dependent inertance for (a) variation of excitation amplitude, A^* and (b) variation of the nonlinear parameter, Γ.

As shown in the Figure 4.8 the shifts are more in the amplitude variation case compared to the nonlinear parameter variation case, this is due to the square dependence of the excitation amplitude in the correction. The Duffing-type inertance as inspired from the Duffing-type stiffness, when compared to it, a positive value for the nonlinearity (Γ)results in a softening behavior where as a negative value for Γ results in a hardening behavior. This is explainable as the inerter enters the attachment as a mass parameter, which is in the denominator. The bandgap widens for a positive Γ shifting the acoustic mode to lower frequencies. Figure 4.8 (a) which is the excitation amplitude variation, the lower bound of the bandgap shifts to $\bar{\omega} = 0.696$ for A^*=0.1 and to $\bar{\omega} = 0.690$ for A^*=0.2 from the LIAM's lower bound which is at $\bar{\omega} = 0.707$ for all excitation amplitudes. Hence physically realizing a Duffing-type inertance in the acoustic-metamaterials could be utilized as a passive adaptive means to filter out mechanical waves in the frequency range just below the LIAM's bandgap based only on their amplitude.

Figure 4.9 shows the effect of the excitation amplitude, A^* and the nonlinearity parameter, Γ on the displacement transmissibility for the resonator mass. The first order frequency correction has a negative sign as given by Equation 4.40 for the displacement transmissibility u^*, unlike the correction for the dispersion relation given by Equation 4.34. Hence, a positive value of the nonlinearity parameter results in a hardening response for the transmissibility similar to the Duffing-type oscillator, but its dependence on the frequency is of a much higher order. The presence of the acceleration-dependent inertance in the local attachment couples its influence between the resonator and the lattice chain. The correction for the dispersion curves is seen to be of a larger magnitude than the correction for the resonator's response. Therefore, although the resonator displays a hardening response with increase in excitation amplitude for a positive value of Γ as predicted by the corrections, the lattice chain displays a more massive response, with the result that the band gap widens below the corrected local resonance frequency for the NLIAM with AD inertance.

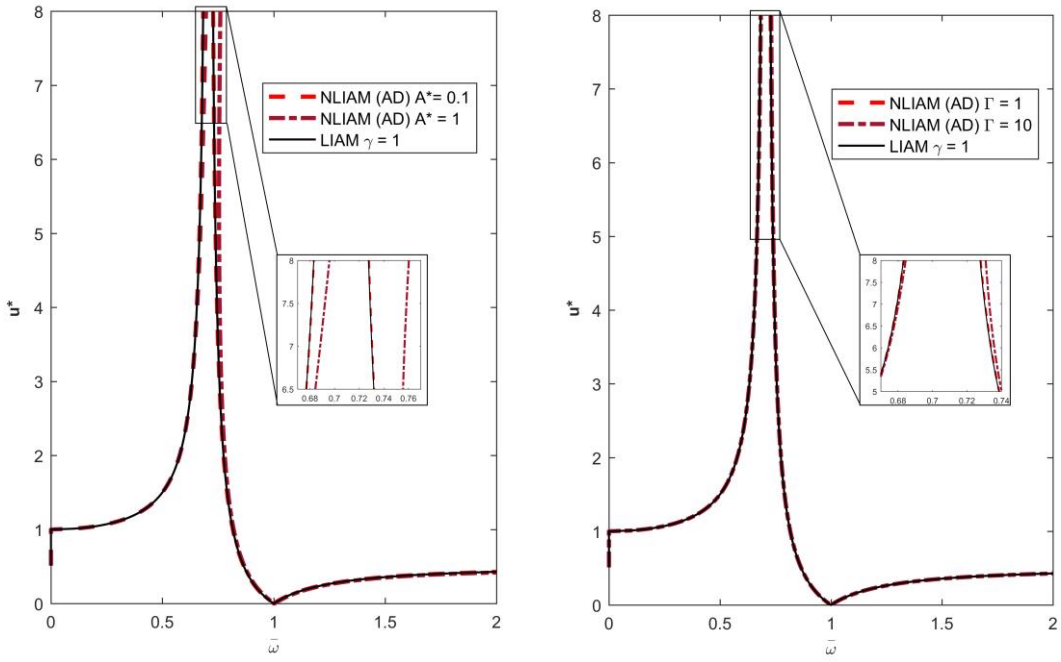

(a) *(b)*

Figure 4.9: Influence of excitation amplitude, A^* and nonlinearity, Γ on the displacement transmissibility of the resonator (attachment) mass.

4.4 Summary

The wave propagation characteristics of nonlinear inertant acoustic metamaterials having nonlinear inerter in the local attachments were investigated using the effective mass model for their discrete element lattice representation. The notional concepts for frequency-dependent and acceleration-dependent nonlinear inertant devices are postulated using the ball-screw inerter as the basis. Using the effective mass approach the dispersion characteristics of NLIAM with frequency-dependent inertance were studied. The inverse square law model can ensure a bandgap over the entire frequency range, but the limiting values of inertance was not physically realizable. Hence a more practical power law inertance is approximated with the inverse square law. Next, the dispersion characteristics of NLIAM with acceleration-dependent inertance were studied using a perturbation approach. The first order corrections to frequency and displacement were derived for an NLAIM with cubic acceleration-dependent nonlinear inertance. Further, the transmissibility for the resonator is studied the first order corrections were derived using the same approach.

CHAPTER V

CONCLUSIONS AND RECOMMENDATIONS

5.1 Conclusions

The world around us is rapidly evolving due to engineering progress and humans continue to innovate with new structures and materials to maximize performance and improve his comfort. Among the many recent mechanical innovations that have come forth, the invention of a new mechanical element known as the inerter has provided several exciting opportunities to enhance the dynamical performance of mechanical systems. Inerter is a two terminal mechanical element which gives a force response proportional to the relative acceleration across two ends. The proportionality constant is termed as its inertance which has the dimension of mass. The prominent mechanical realizations of the inerter are the ball-screw and rack-and-pinion inerters. It displays a relatively high dynamic mass under dynamic loading although its static device mass can be quite small.

In this study, inspired by acoustic metamaterials, the dynamic characteristics of 'meta-structures' that employ inerters are explored. Firstly, improved analytical models and parametric design studies for two prominent embodiments of the inerter viz. the rack-and-pinion and the ball-screw inerter are considered. Analytical models incorporating component inertias and sizing were developed for both versions. The dependence of specific inertance, which is the ratio of inertance to static mass, on key parameters are brought out through simulations. A prototype rack-and-pinion inerter with a specific inertance of 90 was designed, fabricated and tested under low-rate displacement and acceleration-controlled excitations.

Both displacement as well as acceleration controlled excitation cases at low frequencies (< 5 Hz) were considered during testing of the structural-scale inerter. The experimentally determined specific inertance displays a negative exponential trend with the excitation frequency for both the cases. Deviations from predictions are attributable to the frequency dependence of internal stiffness and damping in the fabricated prototype. Based on these results, the inherent internal stiffness and damping in the prototype test article were estimated using a phase matching procedure using a representative lumped element model. The internal stiffness and damping show increasing and decreasing trends respectively with increase in the excitation frequency and are observed to asymptote to finite limits. A discrete element simulation model was setup in ABAQUS. Using the theoretical value of inertance and the average internal stiffness and damping as inputs, the inertance predicted from simulations is found to have good agreement with experiment although the magnitude of deviation is larger for the low frequency cases. Further, spectral examination of the experimental phase lag shows the presence of ultra-low frequency components (< 1 Hz) in addition to the excitation frequency indicating the possibility of meandering effects stemming from within the structural assembly. Based on the results of this parametric study, design perspectives have been advanced for such mechanical inerters, which are seeing increasing use in several low-frequency applications. It is envisioned that the phase matching-based approach can be utilized to subsume the specific nonlinear characteristics of individual inerters into a simple yet unsimplistic model that can be used to more efficiently and accurately predict the behavior of multi-element, inerter-based systems that employ them.

Due to the inability of a structural inerter to be responsive at high frequencies unless extreme gearing ratios are employed as well as the challenges involved in miniaturizing the rotary components for microscale applications, a potential kinematically simpler structure that can display inerter-like behavior is desirable. A candidate structure based on a modification of the von Mises truss is investigated to ascertain its inertant characteristics. The nonlinear equation of motion for this structure is derived using Hamilton's principle. Numerical simulations were carried out for the

lumped parameter model of the structure under harmonic displacement and force inputs. The parametric influences on specific inertance for this structure are established using these simulations. The decreasing trend in the specific inertance with increase in swing-arm mass and swing-arm length indicates the need for additional kinematic transformations in order to ensure that the sense of the rotational throw of the swing-arm mass is opposite to the direction of motion of the vertex mass in order to mirror the sense of the flywheel's rotation in the rack-and-pinion inerter.

The inherent nonlinearity present in structural inerters is inevitable due to design and fabrication aspects of the inerter. The nonlinearities present in the inerter can be used as a passive way to alter tuned mass participation. Studies on such inherent nonlinearities due to design or fabrication aspects for inerters are more widely available, while those concerning the use of intentionally nonlinear inerters to enrich the dynamics of systems that employ them are comparatively scarce. On the other hand, research on inertant acoustic metamaterials is still emerging. . In this context, the mechanical wave manipulation characteristics of Nonlinear Inertant Acoustic Metamaterial (NLIAM) configurations are studied using analysis and simulations for their one-dimensional discrete element lattice representations. Based on notional concepts for nonlinear inertant devices, potential frequency-dependent and acceleration-dependent nonlinear inertant models are advanced. Using an effective mass model for the NLIAM with frequency-dependent inertance in the local resonator attachment, the dispersion characteristics of inverse square law and power law inertance models are examined and contrasted with those for an acoustic metamaterial with frequency invariant inertance. While a tuned inverse square law inertance model ensures the existence of a band gap over almost the entire frequency bandwidth of interest even encompassing the extremely low frequency regime, the low and high frequency limits for this inertance law would be challenging to realize in practice. A potentially more practical power law approximation is proposed and shown to deliver a widening of the band gap by more than 100% towards frequencies below the lower bound of the band gap for the acoustic metamaterial with frequency invariant inertance. Further, drawing inspiration from the Duffing-type stiffness, an acceleration-dependent

cubically nonlinear inertance model is proposed. First order corrections to the dispersion characteristics are obtained for an NLIAM with acceleration-dependent inertance using a perturbation approach akin to the method of multiple scales. For weakly nonlinear cases, excitation amplitude-activated shifts in the dispersion curves are found to enable this NLIAM to act as a passive adaptive filter for mechanical waves based solely on their excitation amplitude. Practical manifestations of such NLIAM could therefore provide a means to realize extraordinary wave manipulation capabilities especially suitable for low frequency structural dynamic applications.

5.2 Recommendations

Ever since the inerter was first postulated and then realized in practice, it has seen increasing use in performance-oriented applications including vehicle suspension systems and as an enhancement to tuned mass damper systems. In general, there is much scope to explore the applications of inerter in several related areas where dynamic mass is desirable without significant increase in the static device mass. The following are some recommendations for future research based on the lessons learnt from this study:

1. Fabrication and testing procedures: The use of precision parts and high tolerances for fit between components is recommended to minimize inherent nonlinearities from fabrication and assembly considerations. The test article fabricated in this study could be improved by adopting transition or interference fit for attaching gears to shafts and shafts to bearings which could significantly reduce the play between them while testing. Custom fabricated components rather than modified COTS or 3D printed components are recommended where needed to facilitate operational efficiency. The use of active control during testing can also be implemented for the testing.

2. Kinematically simpler structures for inerters: While the lumped parameter analytical model for the kinematically simpler structure based on the von Mises truss gives an idealized representation, in practice the use of bistable arches involving deformation of continuous structures would be required to construct such structures. Moreover, the additional kinematic coupling

required to ensure that the sense of the swing-arm mass's throw is representative of the rotary motion of the flywheel requires further investigation. Also improved designs could be developed for the testing of such structures with mechanisms to vary the swing-arm mass and its location. With current additive and hybrid manufacturing processes attaining critical commercial maturity, it is an opportune time to explore new designs that can take advantage of this to develop inerters for microscale applications.

3. Nonlinear Inertant Acoustic Metamaterials: Transitioning the advantage of inertant acoustic metamaterials to real world applications would require lab-scale demonstrations for specific configurations to begin with. There is much to be gained by exploring the potential for such meta-structures deploying inerters to be used for seismic wave mitigation, as well as for lightweight and long-distant mechanical actuation such as in cable-harnessed or large collapsible structures. This study was limited to the one dimensional propagation case using lumped parameter models for just one local engineered configuration. Ample scope exists to elaborate upon the theoretical explorations for multidimensional propagation characteristics for diverse local configurations. This could pave the way for enriched dynamics in several structural dynamic applications.

REFERENCES

[1] F. A. Firestone, “A new analogy between mechanical and electrical systems”, Journal of the Acoustical Society of America, 4, 249–267, 1933.

[2] M. C. Smith, “Synthesis of mechanical networks: the inerter”, IEEE Transactions on Automatic Control, 47, 1648–1662, 2002.

[3] M. C. Smith and F. C. Wang, “Performance benefits in passive vehicle suspensions employing inerters”, Vehicle System Dynamics, 42, 235–257, 2004.

[4] F. C. Wang, C. H. Yu, M. L. Chang and M. Hsu. “The performance improvements of train suspension systems with inerters”, in Proceedings of the 45th IEEE Conference on Decision and Control, San Diego, USA, 13–15 December 2006, 1472–1477.

[5] S. S Evangelou, D. J. N. Limebeer, R. S. Sharp and M. C. Smith, “Steering compensation for high-performance motorcycles”, in Proceedings of the 43rd IEEE Conference on Decision and Control, Paradise Island, Bahamas, 14–17 December 2004, 749–754.

[6] C. Papageorgiou and M. C. Smith, “Laboratory experimental testing of inerters”, in Proceedings of the 44th IEEE Conference on Decision and Control, 2005 and 2005 European Control Conference, CDC-ECC ’05, 12–15 December 2005, 3351–3356.

[7] F. C Wang, M. F. Hong, and T. C. Lin, “Designing and testing a hydraulic inerter”.

[8] S. J. Swift, M. C. Smith, A. R. Glover, C. Papageorgiou, B. Gartner and N. E. Houghton, “Design and modelling of a fluid inerter”, International Journal of Control, 86, 2035-2051, 2013.

[9] Y. Liu, M. Z. Q. Chen and Y. Tian, “Nonlinearities in landing gear model incorporating inerter”, Proceeding of the 2015 IEEE International Conference on Information and Automation, Lijiang, China, August 2015.

[10] M. Z. Q. Chen, C. Papageorgiou, F. Scheibe, F. C. Wang and M. C. Smith, “The missing mechanical circuit element”, IEEE Transactions on Circuits and Systems, 9, 10–26, 2009.

[11] F. C. Wang and W. J. Su, “Impact of inerter nonlinearities on vehicle suspension control”, Vehicle System Dynamics, 46, 575–595, 2008.

[12] D. Xin, L. Yuance, M. Z. Q Chen, “Application of inerter to aircraft landing gear suspension”, Proceedings of the 34th Chinese Control Conference July 28-30, 2015, Hangzhou, China.

[13] Y. Shen, L. Chen, X. Yang, D. Shi and J. Yang, “Improved design of dynamic vibration absorber by using the inerter and its application in vehicle suspension”, Journal of Sound and Vibration, 361, 148–158, 2016.

[14] Y. Hu, C. Li and M. Z. Q. Chen, “Optimal control for semi-active suspension with inerter”, Proceedings of the 31st Chinese Control Conference July 25-27, 2012, Hefei, China.

[15] M. Z. Q. Chen, Y. Hu, C. Li and G. Chen, “Performance benefits of using inerter in semiactive suspensions”, IEEE Transactions on Control Systems Technology, 23, 2015.

[16] M. Z. Q. Chen, Y. Hu, C. Li and G. Chen, “Semi-active suspension with semi-active inerter and semi-active damper”, Proceedings of the 19th World Congress of The International Federation of Automatic Control Cape Town, South Africa. August 24-29, 2014.

[17] M. Z. Q. Chen, Y. Hu and B. Du, “Suspension performance with one damper and one inerter”, 24th Chinese Control and Decision Conference (CCDC), 2012.

[18] A. Kuznetsov, M. Mammadov, I. Sultan and E. Hajilarov, “Optimization of improved suspension system with inerter device of the quarter-car model in vibration analysis”, Archives of Applied Mechanics, 81, 1427–1437, 2011.

[19] T. T. Tran and H. Hasegawa, “Advanced passive suspension with inerter devices and optimization design for vehicle oscillation”, International Journal of Mechanical Engineering and Robotics Research, 4, 2015.

[20] Z. Zhang, M. Z. Q. Chen and L. Huang, “Frequency response of a suspension system with inerter and play”, The 21st International Congress on Sound and Vibration 13-17 July, 2014, Beijing/China.

[21] P. Li, J. Lam and K. C. Cheung, “Investigation on semi-active control of vehicle suspension using adaptive inerter”, The 21st International Congress on Sound and Vibration 13-17 July, 2014, Beijing/China.

[22] Y. Hu, K. Wang and M. Z. Q. Chen, “Performance optimization for passive suspensions with one damper one inerter and three springs”, Proceeding of the 2015 IEEE International Conference on Information and Automation Lijiang, China, August 2015.

[23] Y. Hu and M. Z. Q. Chen, “Performance evaluation for inerter-based dynamic vibration absorbers”, International Journal of Mechanical Sciences, 99, 297–307, 2015.

[24] I. F. Lazar, S. A. Neild and D. J. Wagg, “Using an inerter-based device for structural vibration suppression”, Earthquake Engineering and Structural Dynamics, 43, 1129–1147, 2014.

[25] P. Brzeski, E. Pavlovskaia, T. Kapitaniak and P. Perlikowski, “The application of inerter in tuned mass absorber”, International Journal of Non-Linear Mechanics, 70, 20–29, 2015.

[26] M. Z. Q. Chen, Y. Hu, L. Huang and G. Chen, “Influence of inerter on natural frequencies of vibration systems”, Journal of Sound and Vibration, 333, 1874–1887, 2014.

[27] F. C. Wang, C. W. Chen, M. K. Liao and M. F. Hong, “Performance analyses of building suspension control with inerters”, Proceedings of the 46th IEEE Conference on Decision and Control: New Orleans, LA, USA, 2007; 3786–3791.

[28] F. C. Wang, M. F. Hong and C.W. Chen, “Building suspensions with inerters”. Proceedings IMechE, Journal of Mechanical Engineering Science, 224, 1605–1616, 2009.

[29] P. Li, J. Lam, and K.C. Cheung, “Investigation on semi-active control of vehicle suspension using adaptive inerter”, The 21st International Congress on Sound and Vibration (ISCV 2014), Beijing, China, 13-17 July 2014. In Conference Proceedings, 2014, 4, 3367-3374.3.

[30] P. Li, J. Lam and K. C. Cheung, “Control of vehicle suspension using an adaptive inerter”, Journal of Automobile Engineering, 229, 1934–1943, 2015.

[31] P. Brzeski, T. Kapitaniak and P. Perlikowski, “Novel type of tuned mass damper with inerter which enables changes of inertance”, Journal of Sound and Vibration, 349, 56–66, 2015.

[32] P. Brzeski, M. Lazarek and P. Perlikowski, “Experimental study of the novel tuned mass damper with inerter which enables changes of inertance”, Journal of Sound Vibration, 404, 47-57, 2017.

[33] N. D. J Smith and D. J. Wagg “A fluid inerter with variable inertance properties”, In Proceedings of the 6th European Conference on Structural Control, Sheffield, England, 11–13 July 2016.

[34] P. Brzeski and P. Perlikowski, “Effects of play and inerter nonlinearities on the performance of tuned mass damper”, Nonlinear Dynamics, 88, 1027–1041, 2017.

[35] F. H. Moraes, M. Silveira and P. J. P. Gonçalves, “On the dynamics of a vibration isolator with geometrically nonlinear inerter”, Nonlinear Dynamics, 93, 1325–1340, 2018.

[36] Y. Shen, L. Chen, Y. Liu and X. Zhang, “Modeling and optimization of vehicle suspension employing a nonlinear fluid inerter”, Shock and Vibration, 2016, Article ID 2623017.

[37] X. Q. Sun, L. Chen, S. H. Wang, X. L. Zhang and X. F. Yang, “Performance investigation of vehicle suspension system with nonlinear ball-screw inerter”, International Journal of Automotive Technology, 17, 399−408, 2016.

[38] A. G. Buelga, I. F. Lazar, J. Z. Jiang, S. A. Neild and D. J. Inman, “Assessing the effect of nonlinearities on the performance of a tuned inerter damper”, Structural Control and Health Monitoring, 24, 2017.

[39] M. A. Savi, P. M. C. L. Pacheco and A. M. B. Braga, “Chaos in a shape memory two-bar truss”, International Journal of Non-linear Mechanics, 37, 1397-1395, 2002.

[40] B. A. Fulcher, D. W. Shahan, M. R. Haberman, C. C. Seepersad and P. S. Wilson, "Analytical and experimental investigation of buckled beams as negative stiffness elements for passive vibration and shock isolation systems", Journal of Vibration and Acoustics, 136, 2014.

[41] L. Kashdan, C. C. Seepersad, M. Haberman and P. S. Wilson, "Design, fabrication, and evaluation of negative stiffness elements using SLS", Rapid Prototyping Journal 18, 194-200, 2012.

[42] X. Liu, X. Huang and H. Hua, "On the characteristics of a quasi-zero stiffness isolator using Euler buckled beam as negative stiffness corrector", Journal of Sound and Vibration 332, 3359-3379, 2013.

[43] S. Barbarino , M. E. Pontecorvo and F. S. Gandhi, " Energy dissipation of a bi-stable von-Mises truss under harmonic excitation", 53rd AIAA/ASME/ASCE/AHS/ASC Structures, Structural Dynamics and Materials Conference 23 - 26 April 2012, Honolulu, Hawaii.

[44] S. Barbarino , M. E. Pontecorvo and F. S. Gandhi, " Energy dissipation of a bi-stable von-Mises truss under impulsive excitation", 54th AIAA/ASME/ASCE/AHS/ASC Structures, Structural Dynamics, and Materials Conference 8-11 April 2013, Boston, Massachusetts.

[45] M. E Pontecorvo, S. Barbarino, G. J Murray and F. S Gandhi, "Bistable arches for morphing applications", Journal of Intelligent Material Systems, 24, 274-286, 2012.

[46] S. Palathingal and G. K. Ananthasuresh, "Design of bistable arches by determining critical points in the force-displacement characteristic", Mechanism and Machine Theory 117, 175-188, 2017.

[47] V. M. Shalaev. "Optical negative-index metamaterials", Nature Photonics, 1, 41–48, 2007.

[48] E. Shamonina and L. Solymar. "Metamaterials: How the subject started. Metamaterials", Metamaterials, 1, 12–18, 2007.

[49] R. A. Shelby, D. R. Smith, and S. Schultz. "Experimental verification of a negative index of refraction", Science, 292, 77–79, 2001.

[50] G. V. Viktor, "The electrodynamics of substances with simultaneously negative values of ε and μ", Soviet Physics Uspekhi, 10, 509, 1968.

[51] J. B. Pendry, “Negative refraction makes a perfect lens”, Physical Review Letters, 85, 3966-3969, 2000.

[52] J. M. Manimala, H. H. Huang, C. T. Sun, R. Snyder and S. Bland, “Dynamic load mitigation using negative effective mass structures”, Engineering Structures, 80, 458, 2014.

[53] R. S. Lakes, T. Lee, A. Bersie and Y. C. Wang, “Extreme damping in composite materials with negative-stiffness inclusions”, Nature, 410, 565, 2001.

[54] A. N. Norris. “Acoustic cloaking theory”. Proceedings of the Royal Society A, 464, 2411–2434, 2008.

[55] S. A. Cummer and D. Schurig. “One path to acoustic cloaking”, New Journal of Physics, 9, 45, 2007.

[56] R. Martinez-Sala, J. Sancho, J. V. Sanchez, V. Gomez, J. Llinares and F. Meseguer, “Sound attenuation by sculpture”, Nature, 378, 241-241, 1995.

[57] J. H. Vincent, “LX. On the construction of a mechanical model to illustrate Helmholtz's theory of dispersion”, Philosophical Magazine, 46, 557-563, 1898.

[58] S. H. Lee, C. M. Park, Y. M. Seo, Z. G. Wang, and C. K. Kim, “Acoustic metamaterial with negative density”, Physics Letters A, 373, 4464–4469, 2009.

[59] H. H. Huang, C. T. Sun, and G. L. Huang. “On the negative effective mass density in acoustic metamaterials”, International Journal of Engineering Science, 47, 610–617, 2009.

[60] G. L. Huang and C. T. Sun. “Band gaps in a multiresonator acoustic metamaterial”, Journal of Vibration and Acoustics, 132, 031003, 2012.

[61] N. Fang, D. Xi, J. Xu, M. Ambati, W. Srituravanich, C. Sun and X. Zhang, “Ultrasonic metamaterials with negative modulus”, Nature Materials, 5, 452-456, 2006.

[62] Z. Liu, X. Zhang, Y. Mao, Y. Y. Zhu, Z. Yang, C. T. Chan and P. Sheng, “Locally resonant sonic materials”, Science, 289, 1734-1736, 2000.

[63] B. S. Lazarov and J. S. Jensen, “Low-frequency band gaps in chains with attached non-linear oscillators”, International Journal of Non-Linear Mechanics, 42, 1186-1193, 2007.

[64] P. P. Kulkarni and J. M. Manimala, “Nonlinear and inertant acoustic metamaterials and their device implications”, in proceedings of the SEM Annual Conference on Experimental Mechanics, Indiana, USA, 2018.

[65] P. P. Kulkarni and J. M. Manimala, “Longitudinal elastic wave propagation characteristics of inertant acoustic metamaterials”, Journal of Applied Physics, 119, 2016.

[66] R. K. Narisetti, M. J. Leamy, and M. Ruzzene, “A perturbation approach for predicting wave propagation in one-dimensional nonlinear periodic structures”, Journal of Vibration and Acoustics, 132, 031001, 2010.

VITA

Karthik Madhamshetty

Candidate for the Degree of

Master of Science

Thesis: DYNAMIC CHARACTERIZATION OF INERTANT META-STRUCTURES

Major Field: Mechanical and Aerospace Engineering

Biographical:

Education:

Completed the requirements for the Master of Science in Mechanical and Aerospace Engineering at Oklahoma State University, Stillwater, Oklahoma in December, 2018.

Completed the requirements for the Bachelor of Engineering in Mechanical Engineering at Osmania University, Hyderabad, India in 2015.

Experience:
Graduate Research Assistant — Oct 2016 - Present
Solid and Structural Dynamics Lab
School of Mechanical and Aerospace Engineering
Oklahoma State University, Stillwater, OK 74078

Journal Publications:

1. K. Madhamshetty and J. M. Manimala, "*Low-Rate Characterization of a Mechanical Inerter*," **Machines**, v6 (3), 32, 2018.
2. J. M. Manimala, P. P. Kulkarni and K. Madhamshetty, "*Amplitude-Activated Mechanical Wave Manipulation Devices Using Nonlinear Metamaterials*," **Advanced Composites and Hybrid Materials**, Springer Nature. (*accepted*)
3. K. Madhamshetty and J. M. Manimala, "*Extraordinary Wave Manipulation Characteristics of Nonlinear Inertant Acoustic Metamaterials*," invited submission to the **Journal of the Franklin Institute's** special issue on inerter-based systems. (*under review*)

Conference Presentations:

1. K. Madhamshetty and J. M. Manimala, "*Dynamic Characterization of Inertant and Quasi-Inertant Structures*", presented at the **38th AIAA/ ASME Oklahoma Symposium**, Oklahoma Christian University, Edmund, OK, April, 2018

Professional Memberships:
-American Society of Mechanical Engineers